Uncovering new thermal and mechanical behavior at the nanoscale using coherent extreme ultraviolet light

by

Kathleen Marie Hoogeboom-Pot

B.S., Calvin College, 2008

M.S., University of Colorado Boulder, 2012

A thesis submitted to the

Faculty of the Graduate School of the

University of Colorado in partial fulfillment

of the requirements for the degree of

Doctor of Philosophy

Department of Physics

2015

This thesis entitled:
Uncovering new thermal and mechanical behavior at the nanoscale using coherent extreme ultraviolet light
written by Kathleen Marie Hoogeboom-Pot
has been approved for the Department of Physics

Prof. Margaret M. Murnane

Prof. Henry C. Kapteyn

Date

The final copy of this thesis has been examined by the signatories, and we find that both the content and the form meet acceptable presentation standards of scholarly work in the above mentioned discipline.

Hoogeboom-Pot, Kathleen Marie (Ph.D., Physics)

Uncovering new thermal and mechanical behavior at the nanoscale using coherent extreme ultraviolet light

Thesis directed by Prof. Margaret M. Murnane and Prof. Henry C. Kapteyn

Tremendous recent progress in nanofabrication capabilities has made high-quality single-atomic layers and nanostructures with dimensions well below 50 nm commonplace, enabling unprecedented access to materials at the nanoscale. However, tools and techniques capable of characterizing the properties and function of nanosystems are still quite limited, leaving much of the fundamental physics that dominates material behavior in the deep nano-regime still unknown. Further understanding gained by studying nanoscale materials is critical both to fundamental science and to continued technological development. This thesis applies coherent extreme ultraviolet (EUV) light from tabletop high harmonic generation to study nanoscale systems on their intrinsic length and time scales (nanometers and femtoseconds, and above), specifically following thermal transport and acoustic dynamics. These studies have shown where and how nanostructured material properties can be quite different from their bulk counterparts. This has in turn allowed us to develop new theoretical descriptions to guide further work.

By observing heat dissipation from the smallest nanostructure heat sources measured to date (at 20 nm in lateral size), this work uncovers a previously unobserved and unpredicted nanoscale thermal transport regime where both size and spacing of heat sources play a role in determining the heat dissipation efficiency. Surprisingly, this shows that nanoscale heat sources can cool more quickly when spaced close together than when far apart. This discovery is significant to the engineering of thermal management in nanoscale systems and devices while also revealing new insight into the fundamental nature of thermal transport. Furthermore, we harness this new regime to demonstrate the first experimental measurement of the differential contributions of phonons with

different mean free paths to thermal conductivity, down to mean free paths as short as 14 nm for the first time.

The same technique is then applied to the study of acoustic waves in nanostructured materials, where they are used to characterize mechanical properties at the nanoscale. This thesis demonstrates the application of EUV nanometrology for the complete characterization of isotropic ultrathin films down to 50 nm in thickness across a broad range of stiffnesses. By simultaneously measuring both longitudinal and transverse waves, we are able to study trends in elastic properties that are normally assumed to be constant because it is difficult to measure them. This work also extends the technique to study anisotropic materials.

Finally, by observing the acoustic resonances of nanostructured ultrathin bilayers, this work is the first to apply EUV nanometrology to layers with sub-10nm thickness and to measure the mechanical properties of nanostructures down to single monolayer levels. Here it is shown that the density ratio of the ultrathin layers is not substantially altered from the bulk material counterpart, but the nanoscale elastic properties do deviate significantly and follow opposing trends for two different metallic materials.

Dedication

To Justin for constant love and friendship.

To my family for always encouraging deep curiosity about the world.

And to Him who is able to do immeasurably more than all we ask or imagine.

Acknowledgements

My time in grad school and in JILA has been a fantastic experience thanks in no small part to the many great people in the KM group that I've spent this time with and the great leadership, guidance and mentorship that Margaret and Henry provide. While I can't possibly extend thanks to all those who deserve it here, a few particular highlights must be mentioned. Through Margaret and Henry's excellent examples, I learned how important it is to develop the skill of good scientific story-telling — a lesson I will benefit from for the rest of my life. Special thanks to Tory and Craig who taught me that secret stashes of critical lab supplies must be maintained. Thanks to Dan Adams for sharing your truly impressive optics expertise and many excellent discussions which always furthered my understanding of the rigorous science behind my more intuitive ideas. Mark, your friendship and willingness to help us with experimental quirks and understanding more background have been wonderful. Most importantly, thanks to my Boulder family: Qing, you taught me everything I needed to be able to go on and delve deeply in these experiments, and you were a great friend in my first years of late nights in the lab. Travis, it has been a pleasure to watch you gaining the same kind of familiarity I learned from Qing, and you give me great confidence in turning over the ongoing experiments to you and Nico. Damiano and Nico, I think I've spent more of my life in Boulder with you than just about anyone else, and your research expertise and friendship made this all work so well. And those crazy nights when we finally felt like we were figuring it all out were unforgettable. Finally, thanks to Justin whose constant encouragement, support and sanity-keeping — and not a small number of late dinner deliveries in lab made all of this work possible.

Contents

Chapter

Tables

Table

Figures

Figure

Chapter 1

Introduction

The rapidly growing sector of Information and Communications Technologies now consumes up to $\approx 10\%$ of global electricity production, powering billions of personal computing devices, data centers and data transmission services around the world, some recent reports estimate [1, 2]. Moreover, the amount of Internet traffic occurring every hour will soon surpass the total from the year 2000 [2]. Much of this explosion in personal computing, connectivity, and data use and production has been driven by the rapid scaling of the transistors that comprise computer processors to very small size and data storage to very high density. This in turn has made incredible computing power very inexpensive and thus very accessible, such that the majority of people on earth carry billions of transistors in each pocket-sized device. More people today have mobile phones than have access to toilets or latrines [3], raising demand for high-volume production from semiconductor fabrication facilities that now output more transistors every year than the world's farmers grow grains of wheat or rice [4].

These rapid advances drove developments in nanofabrication capabilities such that nanoelectronic devices sold today are made with features smaller than 10 nm [5]. However, a host of new physical effects become significant for materials at such small size scales. Surfaces and interfaces take up an increasing proportion of the total number of atoms within a nanostructure volume. Continuum models for processes like heat transfer and material elasticity no longer apply as the dynamics of individual grains or the atomic lattices that comprise solid materials deviate from the macroscale approximations. Moreover, the capabilities for producing such small structures far

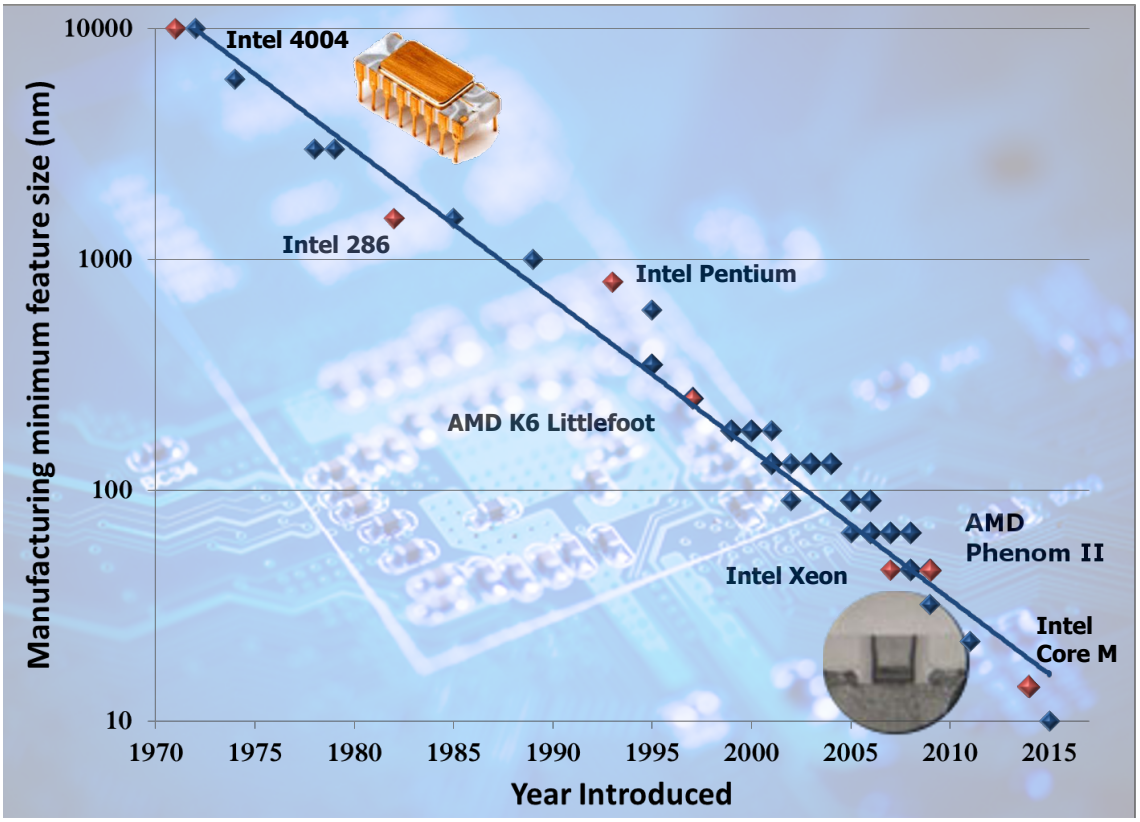

Figure 1.1: **Exponential scaling of transistor feature size** | Moore's Law began as an observation of the trend in the number of transistors comprising an integrated circuit, which have approximately doubled every two years since the 1960s. Now it is the driving guideline that sets the research and development goals of the modern semiconductor industry. To accommodate the growth in number, the minimum feature size within the transistors has seen extraordinary scaling as well. This is a large part of why the computers that used to require rooms full of equipment to do basic math can now easily fit into a pocket and give almost instantaneous access to information from around the world. A few specific CPU feature sizes are highlighted by the red points and labeled.

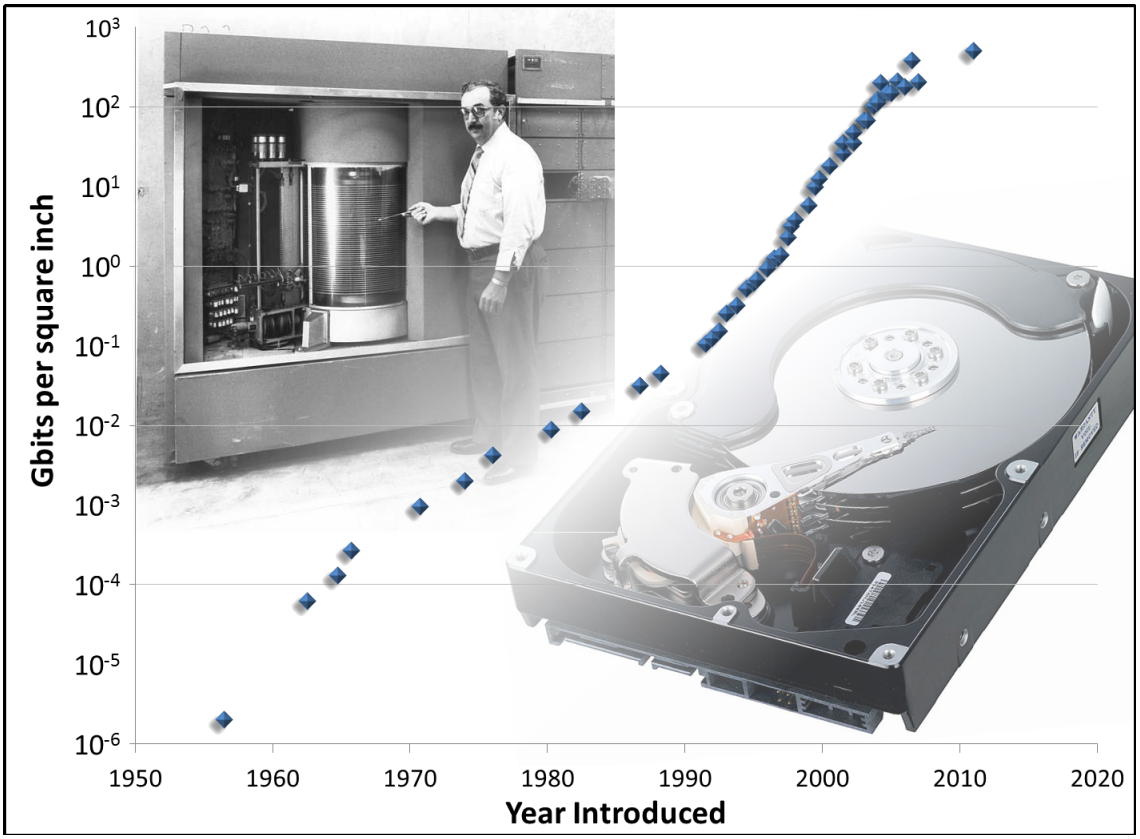

Figure 1.2: **Hard drive data storage density** | Exponential growth is also evident in data storage density. The first commercial hard drive, shown in the left inset image, was introduced in 1956 and stored 3.75 megabytes across its fifty 24-inch disks. Vast improvements in technology since then for both reading and writing data in smaller and more densely packed bits brought us to where we can now hold terabytes on a drive like that shown in the right inset, which can easily be held in one hand.

outstripped the development of tools and techniques that are able to characterize them, such that the nanoscale physics that comes to dominate these systems is still not well understood. This is one of the grand challenges standing in the way of further technological developments at this time. Sub-atomic precision is already needed but hard to obtain [6, 7], prompting the common refrain, "We can't fix what we can't measure." But with steadily rising electricity and energy costs of current technologies, there is much that needs to be fixed — both to improve efficiency within information and communications technologies and to apply them in ways that allow us to lower the other 90% of electricity consumption.

This creates a unique opportunity. Few-atom layers and sub-50nm structures can now be fabricated reliably, offering well-controlled systems for systematic study where we can uncover the fundamental processes that determine dynamics and material characteristics at the nanoscale. In turn, the deeper understanding we achieve will inform future technological developments, as well as provide further probes into the atomic and sub-atomic interactions that control material-level properties and dynamics.

While many types of dynamics demand more fundamental understanding in this nanoscale regime, my focus is on phonons — the collective motions of atomic lattices. These dynamics will fall into two main categories: thermal transport and acoustic wave propagation. Observing both of these in a single measurement with coherent extreme ultraviolet (EUV) light obtained from tabletop high harmonic generation offers the nanometric wavelength and femtosecond light pulses that yield the high spatial and temporal resolution necessary for measurement of nanoscale structures and their ultrafast dynamics.

Chapter 2 introduces the experimental techniques in more detail, discussing pump-probe spectroscopy in general before looking at how it is specifically applied in this thesis. In particular, some unique features of using periodic metallic nanostructures as both samples of study and transducers of dynamics that will illuminate other aspects of the whole material system are presented. Finally, it examines the unique advantages gained from probing nanoscale systems with EUV light and how high harmonic generation creates this coherent light source in a tabletop experiment.

The first application of these techniques is demonstrated in Chapter 3. It begins with an introduction into how and why nanoscale thermal transport is fundamentally different from macroscale transport, along with a summary of important previous experimental observations of this phenomenon. Then, by examining the heat dissipation from the smallest heat sources measured to date (at 20 nm in lateral size), we uncover a new thermal transport regime that dominates when both heat source size and spacing are small compared to the dominant mean free paths of heat-carrying phonons in the substrate material underneath the heat sources. Surprisingly, our new findings imply that nanoscale heat sources can, under defined circumstances, cool more quickly when spaced close together than when isolated, a prediction that we directly confirm with experimental observations of sub-50nm heat sources on a silicon substrate. This discovery has important design implications for many applications of nanoscale thermal engineering, and it yields an unpredicted and previously unobserved insight into nanoscale heat transfer dynamics.

The phonon-filtering nature of this new thermal transport regime is then applied in Chapter 4 to assess the spectrum of phonon contributions to thermal conductivity as a function of mean free path. This represents the first experimental measurement that can benchmark theoretical calculations of such spectra to mean free paths as small as 14 nm. It also offers the first direct experimental access to differential, rather than only integrated, phonon conductivity spectra. Since these spectra are essential to determining nanoscale thermal transport in a given material, this method will be important for future tests of theoretical predictions and to measure these spectra for more complex materials where calculations do not yet exist and may not be practical.

Chapter 5 shifts focus to the acoustic dynamics within nanostructured systems. First it introduces the physical meaning of elastic properties, and then demonstrates how an EUV nanometrology pump-probe technique can be applied to characterize the full elastic tensor of a wide range of soft and stiff isotropic ultrathin films ($\leq$ 100 nm in thickness). In particular, the very short acoustic wavelengths observable with EUV probes allow a wide range in measurement sensitivity to various layers, from characterization of a substrate to full confinement within a thin film to uniquely isolate its properties.

Chapter 6 extends EUV nanometrology to the mechanical properties of composite nanostructures for the first time. Here, surface acoustic waves launched below the nanostructures reveal that the mass density ratio between the nickel and tantalum in a sub-20nm bilayer structure is not significantly modified from its bulk counterpart. On the other hand, longitudinal acoustic resonances of the bilayers themselves show that the elastic properties of the two materials deviate significantly from bulk properties and with opposing trends. In particular, the tantalum layers are observed to stiffen significantly more than is typically observed for other ultrathin metallic layers.

This thesis concludes in Chapter 7 with a summary of the new findings presented and perspectives on a variety of future opportunities inspired by this work, spanning from local characterization based on dynamic coherent diffractive imaging, to new advanced developments in nanometrology using VUV or EUV transient grating technology. Beyond enabling continued development in nanoelectronics, clean energy and new medical therapies, the deeper understanding gained of nanoscale thermal transport and nanoscale elastic properties builds a strong foundation for further exploration of the fundamental material processes at work in nanostructured systems.

Chapter 2

Experimental background

While at first thought the studies of nanoscale heat dissipation and of the elastic properties of nanoscale materials may seem to have little in common, the methods used to observe the dynamics that reveal both sets of properties are very similar. Both can be related to physical deformations of solid materials: the flow of heat through a system will cause thermal expansion and relaxation; elastic properties determine the propagation of acoustic waves, which cause regular expansion and contraction of lattices as they pass. Thus, in order to study the elastic and thermal transport properties unique to nanostructured systems, we use a pump-probe technique to directly observe the systems' dynamic surface deformation. This yields a signal that can be parsed to characterize both sets of nanoscale properties with one efficient measurement.

In this chapter I will introduce the general concepts of pump-probe spectroscopy and its specific application in our experiments, including the use of periodic nanostructures and short-wavelength extreme ultraviolet (EUV) probes to gain strong sensitivity to materials at the nanoscale.

2.1 Pump-probe spectroscopy

Dynamic observations have a few fundamental requirements: some aspect of the system in question must be evolving; those changes must be detectable by some probe of the system; and different times within this evolution must be isolated from one another by a limited observation window and labeled relative to some well-defined time-zero. To rule out statistical anomalies, one

would ideally observe the same evolving process many times, requiring that the dynamics progress repeatably.

Because the understanding of dynamic processes and the ability to predict how they unfold is vital to many aspects of life, civilization and progress, humans have been refining the techniques for making such observations for thousands of years. One of the earliest recorded examples comes from the Ivory Tablet inscribed during the First Dynasty of United Egypt under Menes, ca. 3100 B.C. The Tablet speaks of "Sothis Bringer of the Year and of the Inundation", referring to the beginning of their astronomical calendar and the subsequent flooding of the Nile [8]. By observing the regular progression of the river's dynamics between the heliacal rising (when in the year a star first becomes visible above the eastern horizon for a brief moment just before sunrise [9]) of Sothis (also known as Sirius) and the annual floods, they learned to predict the precise timing of the floods and to arrange their agricultural cycles around them. After that, it was 'just' a matter of refining time resolution to gain understanding about progressively faster processes (see Fig. 2.1).

Two aspects of time resolution required improvement. First, the resolution of time-keeping was improved to make ever more precise measurement of the passage of time. Starting around 1500 B.C., sundials and water clocks broke days into hours and minutes [11]. The introduction of mechanical clocks in Europe around 1300 A.D. made the passage of seconds more visible [15]. Precision was further improved through the use of pendula (first implemented by Christiaan Huygens in 1656), then wheels and springs, before quartz crystal oscillations obviated the need for complicated interactions between mechanical parts in the 1920s [16]. Time-keeping precision took another leap forward with the advent of the cesium atomic clock, first demonstrated at the National Physical Laboratory in England in 1955. The most precise atomic clocks today use the interaction between laser light and atoms to keep track of the passage of time while losing less than a tenth of a second over the age of the universe [17]. However, resolution in the precise timing of the start of observations is not the only necessary parameter to improve.

The second time resolution improvement needed was the duration of an observation, which must be limited so as not to integrate over the dynamics of interest. But until the 1800s the

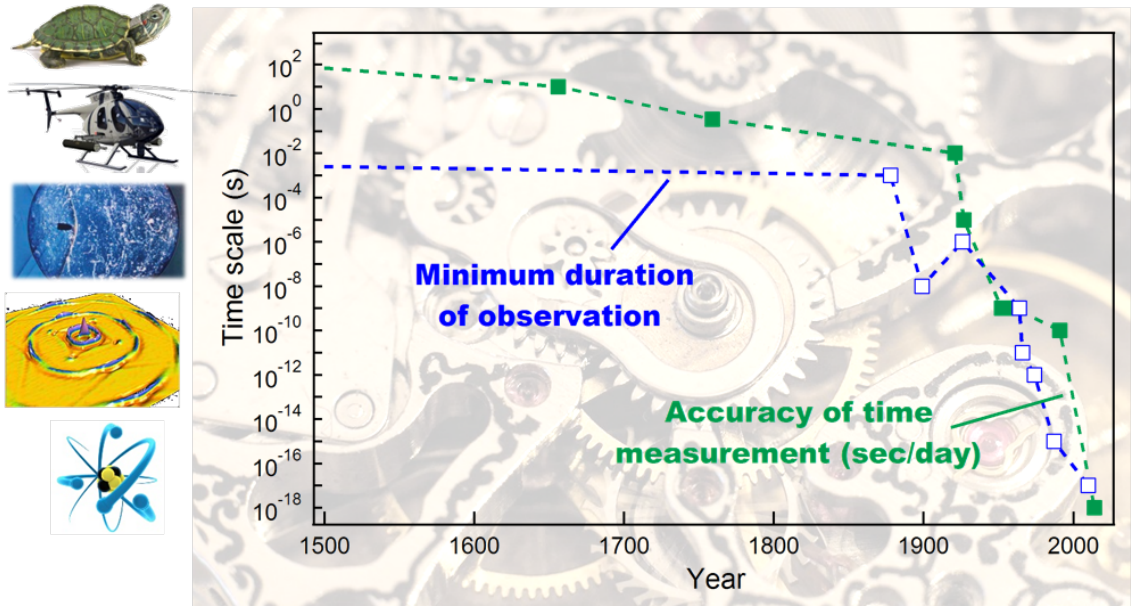

Figure 2.1: **Highlights in the history of time resolution** | Time-resolved observation of dynamics require both accurate time-keeping and short observation durations to freeze the system in different stages of its evolution. Dynamic speeds extend over many orders of magnitude depending on the object of observation; some examples are shown along the left: the slow movements of a turtle, the spinning of helicopter blades, the motion of a bullet through a bubble, the oscillation of nanoscale acoustic waves and the motions of atoms and the electrons within them. The filled green squares plotted follow the development of accuracy in clocks (measured by how many seconds they lose or gain per day), from mechanical gears and springs to atomic clocks. The open blue squares track the shortest time windows available for limiting observation duration. Notably both curves see a steep drop when scientists began to use light for both of these tasks (exploiting atomic resonances for clocks and flashing samples with light to limit an observation window), particularly following the invention of the laser in 1960. [10, 11, 12, 13, 14]

fastest 'detectors' were the human eye (response time around 0.1 s) and ear (0.1 ms) [11]. Then the mechanical-shutter snapshots by photographer Eadweard Muybridge captured images of the sub-second regime with his famous galloping horse in 1878 [18], and physiologist Etienne-Jules Marey led the way in developing these techniques for quantitative measurement [19] (see Fig. 2.2). Harold Edgerton introduced stroboscopic images in the 1920s, freezing the motion of bullets, bubbles, birds and more by limiting observation duration with a microsecond flash of light [14]. Thus measurements could be isolated to the duration of the shortest light flashes that could be generated. Thanks to the invention of the laser in 1960 [20] and fast subsequent developments in pulsed-laser techniques from Q-switching (nanosecond pulses), to active modelocking ($<$ 1 picosecond), to passive modelocking (femtosecond), these incredibly short flashes of light improved minimum observation durations by nine orders of magnitude [12].

It is also the extraordinary coherence and monochromiticity of laser light that enables the stability and sensitivity required for the accurate time-keeping of atomic clocks. Moreover, lasers allowed the precise measurement of time (and frequency) that spurred the redefinition of length, explicitly defining the meter in relation to the speed of light [22]. This highlights an equivalence between precise time-keeping and distance measurement. Thus, we have the tools for isolating femtosecond moments within dynamic processes using the flashes of ultrashort laser pulses and for ordering those moments along a precisely labeled timeline by tracking the distance light travels.

Using changes in light-travel distance to set differences in time was an important aspect of the first investigation that could be recognized as a modern pump-probe experiment. Abraham and Lemoine used an electrical pulse to simultaneously launch a spark and trigger a Kerr-cell shutter [11]. The Kerr cell placed between crossed polarizers will rotate the polarization of incident light enough to allow light through the second polarizer when the cell is activated by an electric field. By varying the distance the light from the spark needed to travel before reaching the Kerr cell and observing the light that traversed the Kerr-cell shutter, they determined how long after activation by the electrical pulse the shutter would remain 'open'. Here we see the well-defined time-zero attained by launching dynamics with a purposeful pump (electrical pulse) to the system,

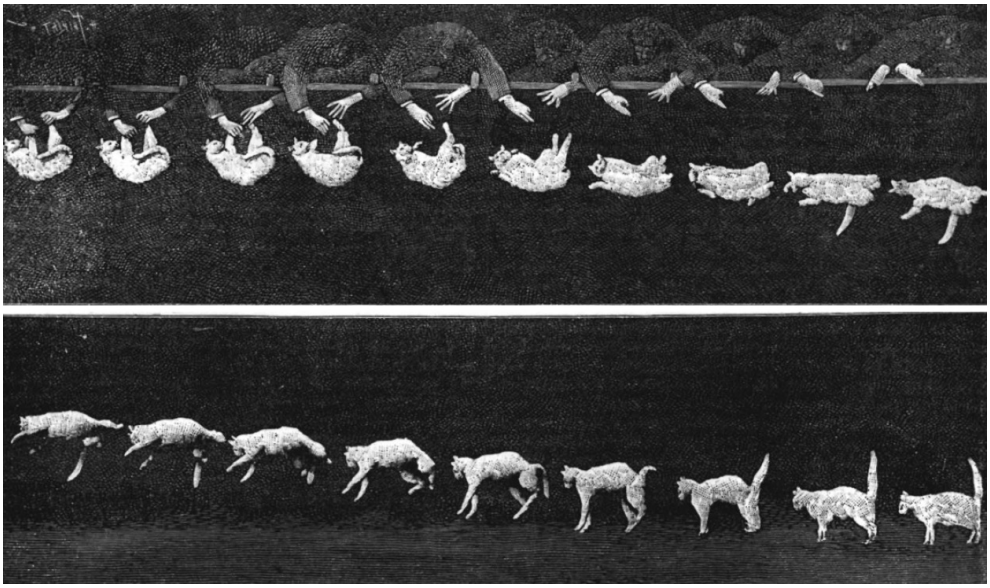

Figure 2.2: **Scientific photography: Marey's falling cat** | While Muybridge famously used photography to win an argument for California governor Stanford about how horses trot and gallop, Marey sought to use similar principles in a quantitative way to learn about the physiology of movement. He developed cameras to capture a series of frames of moving animals, people and objects on the same film so that physical measurements of the photos would be comparable from frame to frame, like those shown in this series of images which offered the first definitive insight into how a falling cat lands [19, 21]. It is also the world's first cat video.

as well as stable synchronicity between the pump and probe (spark light) attained via initiating both from the same electrical pulse. For faster dynamics and the increasingly short measurement windows attained with ultrashort laser pulses, this latter requirement — which ensures repeatable pump-probe delay — will be even more stringent.

2.2 Experimental setup

Thus we have all the necessary ingredients for direct observation of dynamics in nanostructured systems: a system evolving repeatably with time following excitation with a pump laser pulse; and ultrashort probe laser pulses to observe the evolving system at specific moments in time after the pump pulse. The experimental setup is shown schematically in Fig. 2.3. We fabricate nanostructured samples — specifically periodic arrays of metallic nanowires and nanodots on dielectric and semiconductor substrates. The metallic nanostructures strongly absorb infrared light, so we can launch repeatable dynamics with specific time-zero by heating them with an infrared laser pump pulse of consistent energy. The heat delivered by the pump pulse will cause a thermal expansion of the nanostructures that will evolve as the system relaxes back toward its initial state. Our probe pulse will measure these dynamic changes in the surface profile.

Both pump and probe pulses are derived from the same amplified Ti:sapphire laser, yielding the ultrashort pulses which confine our observation windows to below 20 fs with the required synchronicity between pump and probe pulses. Translation stages in the pump arm introduce specific path-length differences relative to the probe arm, yielding controlled time delay between the two pulses with resolution as high as ≈ 50 fs (due the step resolution of our finest delay stage) that labels the time axis of our measurements. Because the pump pulse is significantly shorter than typical thermal-expansion response times, the initial thermal expansion of the nanostructures will occur impulsively and launch acoustic waves in the system at the same time, giving us two classes of dynamics to focus on: heat dissipation, and acoustic oscillation and wave propagation.

As shown in Fig. 2.3, the probe pulse is coupled into a 5cm-long hollow-core waveguide with inner diameter of 150 µm filled with argon gas to generate the short-wavelength EUV beam that

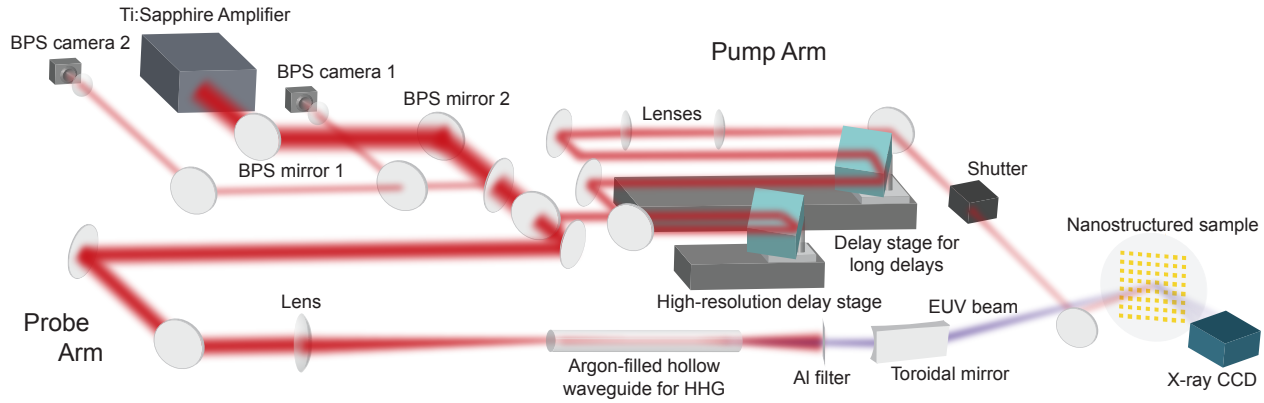

Figure 2.3: **Experimental setup** | The output from a Ti:sapphire amplifier with typical pulse energy of 1.5-2.0 mJ, 3-5kHz repetition rate, 25fs pulse length and spectrum centered around 800 nm in wavelength is split into a pump and probe beam. The pump beam traverses two computer-controlled mechanical delay stages, one with high step resolution (50fs) with maximum delay around 1 ns and the other with much longer travel range which can reach maximum delay times around 8 ns (when the beam travels across the stage four times rather than the two shown here). Two lenses enable an adjustable focal length and spot size for setting the beam diameter at the sample. The intensity can be further adjusted by a half-wave plate and polarizer that can reduce the pump power. A shutter blocks the pump for every other camera exposure to enable frequent comparison to a relaxed sample, and two 200nm aluminum filters mounted on the CCD block the pump light that reflects from the samples. The majority of the laser energy is left for the probe beam, which is focused into an argon-filled hollow waveguide with inner diameter = 150 µm to drive the process of high harmonic generation. This generates even shorter pulses of EUV light with wavelength centered around 30 nm that propagate through two aluminum filters that block the remaining infrared light. The EUV beam is focused by a glancing-incidence toroidal mirror onto nanostructured samples, where it reflects and diffracts to an x-ray-sensitive CCD. A small fraction of the amplifier output is also picked off and split to two cameras separated by a large propagation distance (not to scale) for an active-feedback beam-pointing stabilization (BPS) system which uses two motorized mirrors to compensate for drifts in the laser pointing.

yields sensitivity to the surface dynamics of nanostructures (as discussed in more detail below). Here is where we take advantage of another benefit of using ultrashort light pulses: the possibility for very high peak intensity. To illustrate the significance of this advantage, consider the average power typical of our amplifier output: 8 W at a repetition rate of 4 kHz. To couple into the waveguide, we focus this beam to focal spot size $\approx 120\,\mu$m. If this were a continuous-wave laser, this would imply an intensity of $\approx 1.8 \times 10^4$ W/cm^2. However, concentrating this power into 25fs pulses increases the intensity at the peak of each pulse by ten orders of magnitude to $\approx 1.8 \times 10^{14}$ W/cm^2. Put another way, the corresponding peak power of $8{\times}10^{10}$ W is a little more than the total capacity of the world's largest nuclear power plant, Kashiwazaki-Kariwa in Japan.

2.2.1 Tabletop EUV from high harmonic generation

These very high laser pulse intensities are used to drive the process of high harmonic generation (HHG) [23] to obtain coherent extreme ultraviolet (EUV) light from a tabletop source. The need for such high intensity can be considered in two complementary ways. First, HHG is an extremely nonlinear process, adding the energy from many of the fundamental infrared photons to produce one high-energy high-order harmonic photon. Intuitively this requires a high intensity to concentrate many IR photons in a small area at the same time to make this possible.

More precisely, the high intensity ($> 10^{14}$ W/cm^2) is necessary to make the strength of the laser's electric field comparable to the Coulomb potentials experienced by the electrons in the atomic gas medium. This sets HHG apart from low-order nonlinear processes in which anharmonic motions of bound electrons can radiate few-order harmonic photons. In HHG, the intensity of the driving laser field is high enough to significantly modify the Coulomb potential of the electrons such that they can tunnel ionize away from their parent ions and spend time moving freely in the laser's electric field. This allows a wide range of harmonics with consistent intensity corresponding to the region between having enough energy to ionize and the greatest amount of energy that can be gained during the laser field acceleration, known as the ponderomotive energy U_P. Notably, these constraints on the necessary driving intensity for HHG can be exploited to isolate attosecond pulses

generated only at the peak of driving laser pulse [24, 25], further improving possible resolution for time-resolved experiments utilizing stroboscopic measurement with short light pulses.

The high driving laser intensity implies that the free electrons with charge q and mass m can experience very high accelerations a and pick up a significant amount of kinetic energy, since the force F exerted by the electric field E: $F = qE = ma$. However, laser fields oscillate in amplitude and direction; when the direction reverses, the electrons will slow and then accelerate back toward their parent ions. Most will simply scatter away from the ions, but a few electrons will recombine (about 1 in 10^5 for the 800nm Ti:sapphire driving laser used in this work [26]), emitting the extra energy they gained from the laser field as a high-harmonic photon. For a given driving laser wavelength λ_L and intensity I_L (which set the magnitude of acceleration and maximum time before recombination), and atomic species with ionization potential I_P, this implies the highest photon energy that can be generated is [26]

$$E_{cutoff} \approx I_P + 3.2U_P \approx I_P + I_L\lambda_L^2 \ . \tag{2.1}$$

This simple, semi-classical picture of the HHG process, also known as the Three-Step Model, was developed by Corkum in the early 1990s [27, 28]. Figure 2.4 illustrates the model. While more complete descriptions of the full quantum-mechanical process of HHG have since been developed, this picture remains one that captures the essential elements of single-atom HHG.

However, one atom produces one photon at a time. To generate the photon flux necessary for applying this unique light source to material characterization experiments, we require many atoms creating many HHG photons all adding constructively. Here is where the hollow-core waveguide becomes important. By coupling the driving laser into the gas-filled waveguide, we can maintain a high intensity through a long interaction region. Compare this to a tightly focused beam, which will be characterized by strong divergence, leaving only a very small interaction region with the requisite high intensity near the focus.

Moreover, to ensure the constructive build-up of HHG intensity, all the HHG photons must be emitted in phase. This requires the phase velocity of the HHG light to equal that of the driving

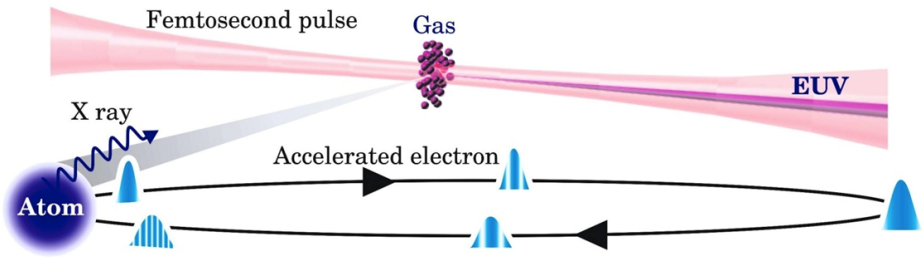

Figure 2.4: **Three-step model for HHG** | The intense laser field of a femtosecond pulse focused into a gas is strong enough to drive electrons to tunnel ionize away from their parent atoms. The electrons are then accelerated in the field, though their wavepackets spread according to the quantum mechanical evolution of free electron trajectories. When the laser field reverses in direction, the electron is driven back toward its parent ion. If it recombines, it can emit the extra energy gained from the laser field as a high-energy EUV or soft x-ray photon. Figure adapted from [29].

laser light, a condition known as 'phase-matching'. This way, those HHG photons created during a particular phase of the driving laser pulse will travel with the driving laser to match up with those HHG photons created at the next equivalent phase of the driving pulse. This is illustrated in Fig. 2.5. The phase velocity of the EUV or soft x-ray HHG photons is essentially always equal to the speed of light in vacuum. The infrared driving laser, however, is strongly affected by both the gas and the waveguide. Phase-matching between the two beams is achieved by tuning the gas pressure P to balance the effects on the driving laser of the waveguide and dispersion due to the ionized atoms (both of which increase the phase velocity) with the dispersion due to the neutral atoms (which decreases the phase velocity) [23] such that the following phase-matching condition is satisfied:

$$\begin{aligned} 0 = \Delta k &= q\left\{\left(\frac{u_{11}^2\lambda_0}{4\pi a^2}\right) - P\left((1-\eta)N_{atm}\frac{2\pi}{\lambda_0}\delta - \eta(N_{atm}r_e\lambda_0)\right)\right\} \\ &= \text{waveguide} - (\text{neutral atoms} - \text{ionized atoms}) \end{aligned} \tag{2.2}$$

where q represents the harmonic order, u_{11} is a constant related to the lowest-order electromagnetic propagation mode of the waveguide, λ_0 is the driving laser wavelength, a gives the inner diameter of the waveguide, η is the ionization fraction of the gas with number density N_{atm}, δ is a constant

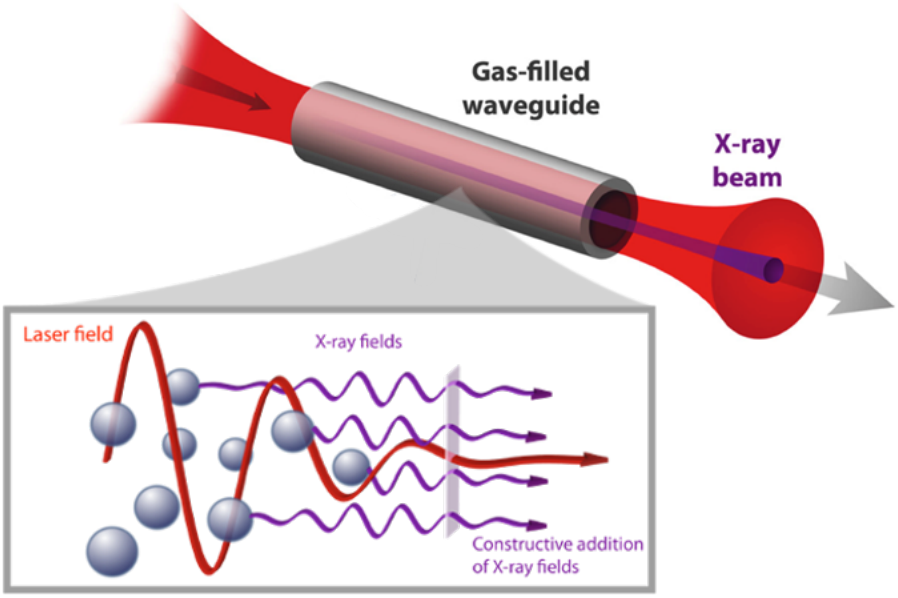

Figure 2.5: **Phase-matching for bright HHG source** | By tuning the gas pressure inside a waveguide, the HHG process can be phase-matched. This implies that the phase velocity of the driving laser field and the emitted x-ray fields are equal, such that x-rays produced at different phases of the driving field add constructively (shown in the inset) to produce a bright, coherent beam at the waveguide output.

(for a given laser wavelength) related to the index of refraction for the atomic gas species and r_e is the classical electron radius.

This phase-matching is possible only until the ionization fraction of the gas is so high that the balance of terms can no longer be achieved. Understanding the interplay between the phase-matching cutoff and the photon energy cutoff found in Eqn. 2.1 paved the way for a unified understanding of how choices in gas medium, driving laser wavelength and intensity can be made to optimize the generation of high-harmonic light spanning from vacuum ultraviolet to $>$ keV x-rays [26]. Thus, while the Ti:sapphire driving laser combined with argon is effective for generating a high flux at the 30nm EUV wavelength utilized in this work, the HHG source is incredibly flexible through different choices in driving laser and gas medium. Furthermore, the ionization fraction will grow through the progression of the driving laser pulse, such that phase-matching can be limited to a small portion of the full pulse duration — particularly for longer driving wavelengths. This has been demonstrated as a way of generating isolated attosecond pulses with much higher photon energies than were previously accessible [30].

The particular advantages of using EUV light from HHG to probe the thermal and acoustic dynamics in nanostructured systems are discussed in more detail in section 2.3. But this wavelength regime also presents a number of challenges. It is strongly absorbed by nearly every medium, requiring all measurements to be conducted in vacuum. This also implies that standard lenses and mirrors cannot be used to direct and focus the EUV beam. Where we need to focus the EUV beam, which diverges from the output of the waveguide, we make use of a glancing-incidence toroidal mirror to preserve as much intensity as possible (shown in Fig. 2.3). Specially-designed multilayer mirrors can also be engineered for relatively high reflectivities (up to about 70% for 13.5nm wavelength), but the high-reflection bandwidth is generally so limited so as to exclude all but one harmonic peak. As will be discussed in the following section, every harmonic wavelength contributes to building our signals, so such monochromatic reflectors would needlessly sacrifice a significant fraction of the EUV flux we generate.

2.2.2 Building a signal

The periodic arrays we study diffract the EUV probe light, yielding an interferometric measurement primarily sensitive to the difference in height between the substrate surface and the top of the nanostructures. The phase difference in the light reflected from these two surfaces controls the diffraction efficiency (the ratio of diffracted peak intensity to reflected zero-order peak intensity), and the changes in surface profile induced by the thermal and acoustic dynamics launched by the pump pulse will dynamically change this diffraction efficiency.

Like Marey in section 2.1, we make use of quantitative photography by capturing diffraction patterns on an x-ray sensitive CCD, where in addition to quantitative information about position across the detector, we also have quantitative information about the intensity of light incident at each pixel. Relative changes in the diffracted peak intensities are on the order of $\approx 10^{-2} - 10^{-3}$, so to construct a clear signal, we record an integrated change in diffraction between the pumped and unpumped sample at each time step. Specifically, the shutter shown in Fig. 2.3 blocks the pump beam for every other camera exposure, alternating the recorded diffraction patterns between that associated with the pumped sample and that from the unpumped sample (see Figs. 2.6 and 2.7). This alternation ensures that the two images are captured close together in time so they will be as comparable as possible. The shorter the exposure times, the less that can change between the two images. However, exposure time cannot be so short that the shutter just catching or just missing the last pulse significantly affects the total number of laser pulses contributing to each image. In practice, we have found that 30ms exposures usually result in high-quality signals, likely striking this balance between variation in number of pulses and variation in the probe from one exposure to the next. At a 4kHz repetition rate, this corresponds to 120 pulses per exposure.

The pixel-by-pixel difference image between the two patterns shown in Fig 2.7 reveals how the change in the zero-order peak is generally opposite to that in the diffraction peaks, as should be expected from conservation of energy. Thus, to integrate the signal in a way that constructs rather than cancels out the contributions from different diffraction orders, we flip the changes in

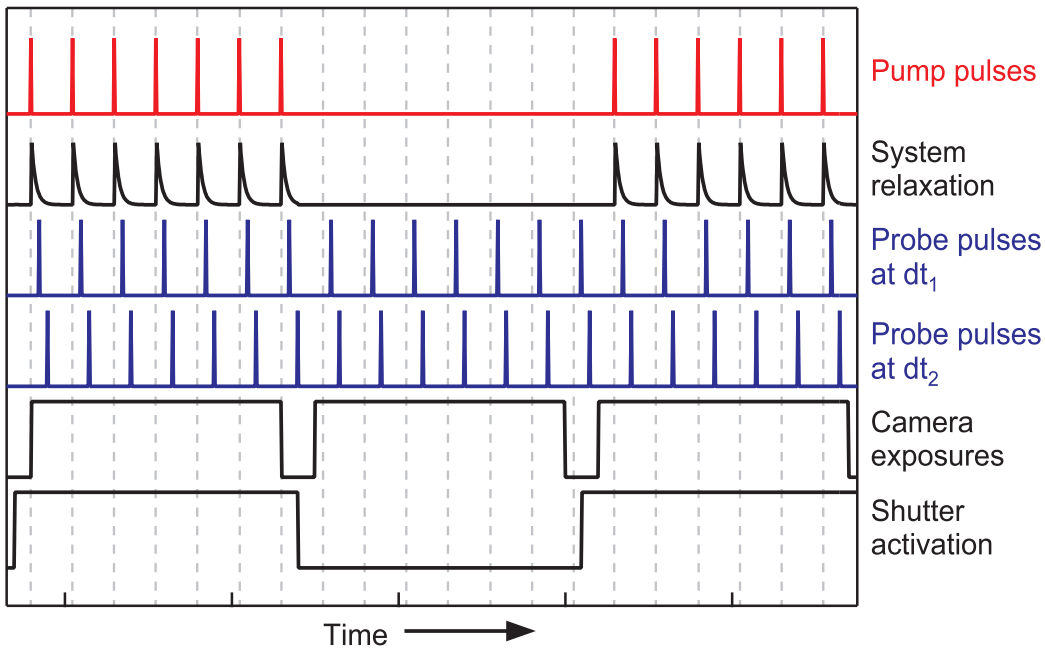

Figure 2.6: **Timing schematic** | Every pump pulse arriving at the sample launches the same dynamics, represented by a simple relaxation in this schematic. The dynamics are probed with a pulse train set to a particular time delay dt relative to the pump pulses, such that the camera exposures receive stroboscopic frames of each time step within the dynamics. A shutter blocks the pump pulses for every other camera exposure, enabling comparison of pump-on to pump-off images nearby in time, thus decreasing the influence of fluctuations in the probe intensity. Note that this schematic is not drawn to scale: each camera exposure actually spans > 100 probe pulses and the sample dynamics (< 20 ns) decay much sooner before the arrival of the subsequent pump pulse (after 250 µs).

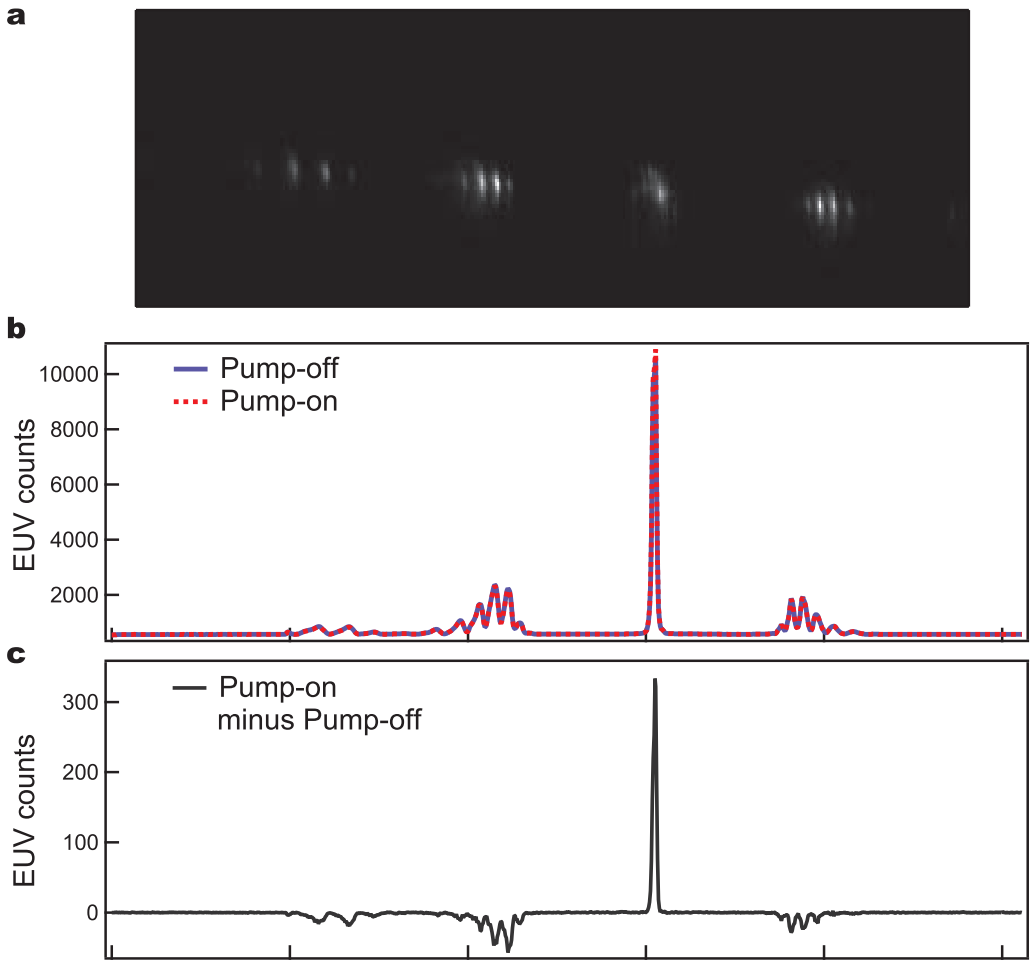

Figure 2.7: **From diffraction image to signal** | In order to speed acquisition time, we do not save full diffraction images like that shown in part **a**. Instead, we vertically bin the images to take advantage of the significantly faster read-out time from the CCD, creating the diffraction patterns shown in part **b**. A careful comparison of the pump-on (dotted red) and pump-off (solid blue) patterns can reveal small differences — the central peak is just slightly taller in the pump-on, the diffraction peaks are just slightly shorter. However, it's the difference image (**c.**) which most clearly reveals the differences between the pumped and unpumped case. After flipping the diffraction-peak differences to match the sign of the central-peak difference, we integrate across the regions with non-zero signal to extract the change-in-diffraction point for this particular time step, 40 ps.

the different peaks to match in sign and then sum across the image. The same combination of flipped and unflipped regions is used for every difference image in a given signal. Also, since HHG generates multiple harmonics simultaneously, a set of discrete harmonic peaks shows up in each diffraction order — and because of their differing wavelengths it is possible that the change in diffraction for one harmonic will be opposite in sign to that for another harmonic, depending on the initial height of the nanostructures (see Fig. 2.8). The time-dependent change in each part of the signal, however, will be the same such that proper summing across the difference images will in general build up the total signal. In principle, it would be possible to use the comparison of the different harmonic signals to determine the initial height of the grating structures — essentially finding the point along the x-axis of Fig. 2.8 where the ratios between the corresponding points on the curves shown matches those observed. In practice, however, too many of the harmonics have too low an intensity and the variation from shot to shot in the ratios between change-in-diffraction signal amplitude from different harmonics is too large to generate a result with useful precision.

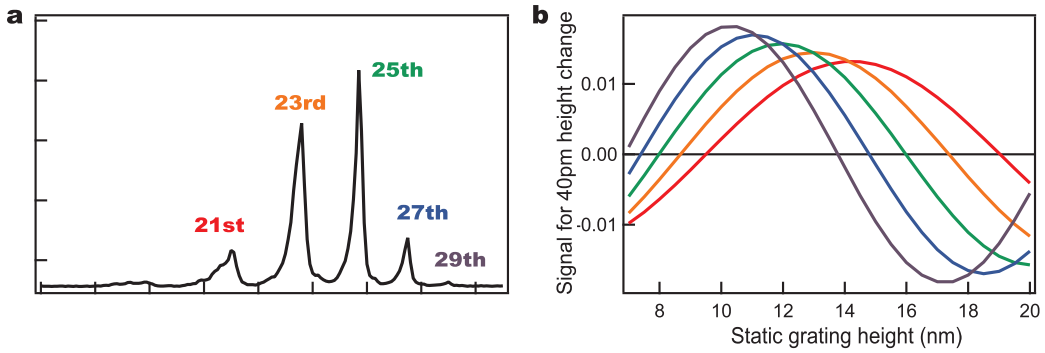

Figure 2.8: **EUV harmonics respond differently to height changes** | Phase-matching conditions for HHG differ from one harmonic wavelength to the next. This controls the relative intensities of the harmonic peaks, like those seen in the typical experimental spectrum shown in part **a**. Each harmonic will also display slightly different responses to a given grating height change (like those caused by laser excitation), depending on the initial static grating height. In particular, part **b** shows that for a given static height, each harmonic will contribute different magnitudes to the signal; at certain grating heights some harmonic signals even have different sign.

Note that simply taking the absolute value of the difference image would lose too much information since it eliminates the possibility of a signal crossing zero. Acoustic oscillations in

particular tend to oscillate around the unpumped state once most of the thermal decay has passed. Creating an artificially non-negative signal by using an absolute value in this case can make the signal appear to oscillate at twice its real frequency (like the absolute value of a sine wave).

To decrease the influence of exposure-to-exposure changes in the pump and probe beam intensities, we normalize the sum of the difference image to the sum of the pump-off image. This result is averaged tens or hundreds of times to produce the data point for one time step. Then the delay stage is moved, changing the pump-probe time delay, and the process repeated. One example of the resulting change-in-diffraction signal is shown in Fig 2.9. Over the time of taking a full scan of many time delays (typically around one-half to one hour), shifts in beam alignment can shift the pump beam location relative to the probe on the sample, and it can significantly change the probe beam intensity since the coupling of the beam into the fiber for HHG is strongly dependent on the beam pointing. To lessen these effects, we employ the active-feedback beam stabilization system visible in Fig. 2.3. This system picks off a small portion of the input laser beam before it splits into pump and probe arms. This diagnostic beam is further split in half and sent toward two cameras that image two points in the beam separated by a long propagation distance. When the beam moves on these cameras, motorized mirrors on the input beam adjust the beam back to its set position. One image point is chosen just downstream of the second motorized mirror in order to decouple corrections by the two mirrors as much as possible; the second image point is chosen to have at least as long of propagation distance as the distance to the sample. We observe that this system reduces fluctuations in the HHG counts and virtually eliminates long-term drift, typically maintaining the EUV intensity over > 10 hours.

Generated as it is by a whole array of nanostructures, though, how should we interpret this dynamic change in diffraction signal?

2.2.3 Diffraction as Fourier transform

Far-field diffraction is reached when the propagation distance z following an aperture is large compared to the ratio of the square of the aperture size to the wavelength λ, and here the output

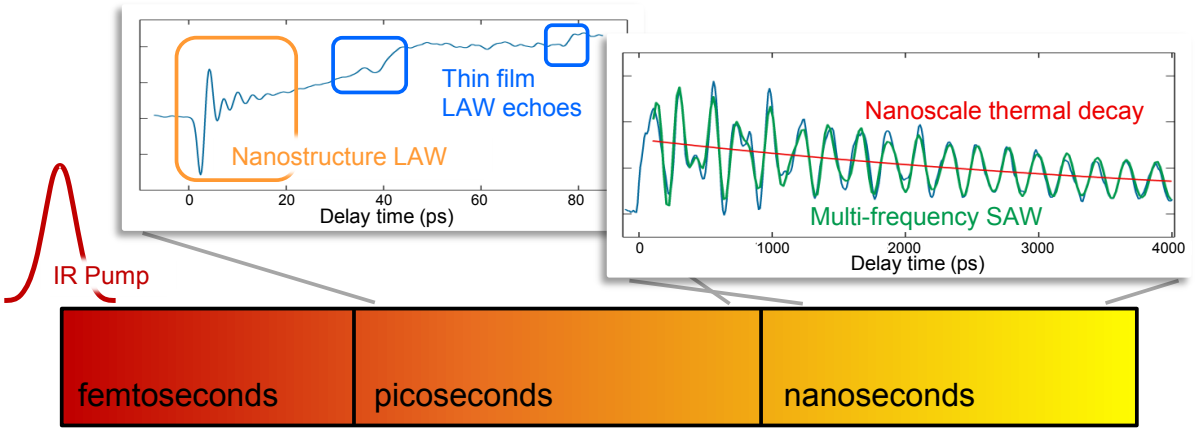

Figure 2.9: **Data separates dynamics by timescale** | The acoustic and thermal dynamics launched by the pump laser excitation naturally separate on different time scales, enabling simple parsing of the signal to extract clear information from each component. Within the first 100 ps, two sets of longitudinal acoustic dynamics appear: the high-frequency oscillation at the beginning corresponds to the longitudinal resonant mode of the nanostructures; the later echoes are the result of a longitudinal pulse that traveled down from the nanostructures into a thin film and reflected back to the surface from a buried interface between the film and the substrate. On the nanosecond time scale, we see multi-frequency surface acoustic oscillations superimposed onto a long, exponential thermal decay.

electric field can be calculated using the Fraunhofer equation [31].

$$U(x,y,z) \propto \iint A(x',y')e^{-i\frac{2\pi}{\lambda z}(xx'+yy')}dx'dy' \tag{2.3}$$

for aperture transmittance A. It can be seen that this is completely equivalent to a Fourier transform of the aperture function A evaluated at frequencies $f_x = x/(\lambda z)$ and $f_y = y/(\lambda z)$ [32].

While the $\approx$ 6 cm between our sample and CCD camera is not fully within this regime, this treatment still offers a useful approximation. Therefore we can use some simple properties of Fourier transforms to gain better intuition regarding what our diffraction signals correspond to.

First, our 1D periodic grating samples with linewidth L and period P are well approximated by the convolution of a *comb* of spacing P with a *rect* function of width L. The Fourier transform then approximates the diffraction pattern:

$$\mathcal{F}[comb(x/P) \otimes rect(x/L)] = comb(Pf_x)sinc(Lf_x) \tag{2.4}$$

where again $f_x = x/(\lambda z)$ relates the incoming spatial coordinate x to the outgoing spatial frequencies. The resulting product of *comb* and *sinc* reveals that the locations of the discrete diffraction peaks are set according to the grating period, and their relative heights are set by the *sinc* function associated with the diffraction pattern from a single nanostructure as shown by the black arrows sampling the red curve in Fig. 2.10. Thus, when we follow the changes in diffraction efficiency as a function of time following pump excitation, this signal corresponds to the response of a single nanostructure, averaged over all the structures illuminated by our probe beam.

This highlights the importance of ensuring a consistent pump excitation over the whole region we probe. For this reason we use a pump beam diameter $\approx$ 400-600µm — much larger than the probe spot of $\approx$ 100 µm such that the pump intensity (assuming a roughly Gaussian intensity profile) does not vary significantly over the area of the probe. The pump beam size can be measured on a CCD camera placed at the same propagation distance as that to the sample location and adjusted using the two lenses shown in the pump arm in Fig. 2.3. Note that these lenses must be placed after the delay stages since the beam must be collimated through the stages so that changing the

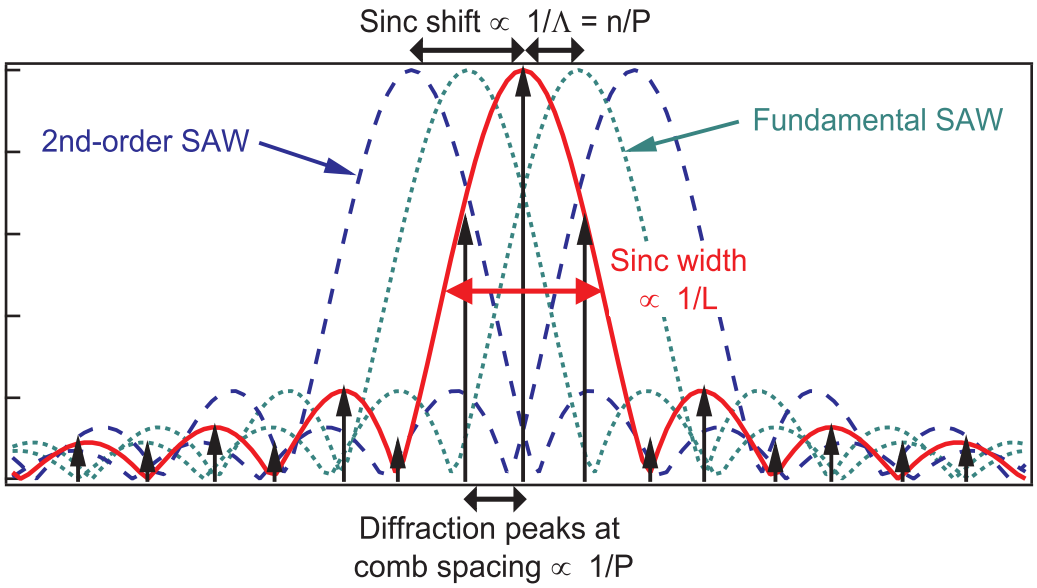

Figure 2.10: **Diffraction peaks highlight specific SAW orders** | The diffraction pattern from a single rectangular-profile nanowire is given by a *sinc* function, shown in solid red, with width set by the linewidth L of the nanowire. The effect of repeating that nanowire in a periodic grating is to sample the single-structure pattern at regular intervals with spacing set by the period P. This is shown by the black arrows (using $P = 2L$ as an example) and it results in the familiar discrete set of diffraction peaks we recognize from the patterns we capture on our CCD. Adding a cosine-shaped SAW excitation below the nanowires adds contributions from the shifted *sinc* functions (shown in dotted lines) to the original, single-structure pattern. Because the SAW wavelengths are set by the harmonics of the grating period, the peaks of these shifted *sincs* line up with existing diffraction peaks, concentrating the signal from specific SAW orders in their corresponding diffraction orders.

time delay does not alter the pump beam size at the sample. The beam must also be carefully aligned parallel to the stages so that it does not move on the sample for changing time delay. Pump beam power must be chosen to balance the desire for a large signal from stronger excitation with the need to avoid damage to the sample, or to avoid exciting it so strongly that the dynamics are no longer linear with pump power. In practice, we typically find this balance around a pump fluence of $\leq$10 mJ/cm^2.

Thus far, this intuitive analysis has only considered the dynamics of small perturbations to the original *rect* of our static sample. This can basically account for the thermal dynamics and longitudinal acoustic wave (LAW) modes within the nanostructures, but the surface acoustic waves (SAWs) launched in the substrate could be better included by adding a term where the *comb* and *rect* are multiplied by a *cos* wave representing the standing wave that forms below all the structures. The diffraction pattern we calculate here is a little more complicated:

$$\begin{aligned}\mathcal{F}\left[(comb(x/P)\otimes rect(x/L))\cdot(1+cos(\Lambda x))\right]&\\ &= comb(Pf_x)sinc(Lf_x)\\ &+(\delta(f_x-1/\Lambda)+\delta(f_x+1/\Lambda))\otimes(comb(Pf_x)\cdot sinc(Lf_x))\end{aligned}\quad(2.5)$$

where Λ is the SAW wavelength — equal to the grating period and integer-fractions thereof (higher harmonics of the spatial frequency) [33]. The first term in this result is the same as in Eqn. 2.4 — a *comb* sampling the *sinc* associated with diffraction from a single structure at points corresponding to the spatial frequency of the grating period. The second set of terms repeats the same pattern except that it is shifted by $\pm 1/\Lambda$. Because any order of the SAWs we excite has spatial frequency equal to one of the grating's spatial frequencies, this shift moves the peak of the repeated *sinc* onto the corresponding diffraction peak from the unshifted function as shown in Fig 2.10. For this reason, the different diffraction orders will display increased sensitivity to the corresponding SAW-order frequencies. This is demonstrated in Fig. 2.11 and often provides a useful method for extracting high-order SAW frequencies with increased precision by integrating the signal only over the corresponding diffraction orders.

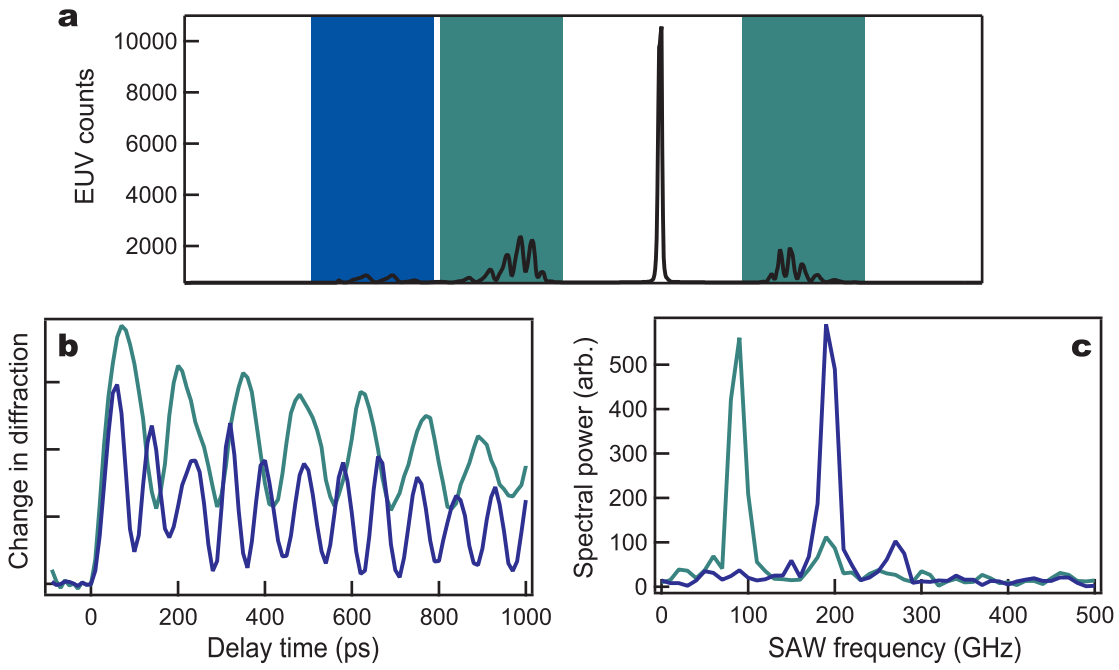

Figure 2.11: **SAW selectivity observed** | By integrating specific sections of the diffraction patterns to build a time-dependent change-in-diffraction signal, we can directly observe that the signal from different SAW harmonics is concentrated in their corresponding diffraction orders. Specifically, integrating over the blue sections (including only the second-order diffraction peaks) of a diffraction pattern shown in part **a** from a sample with nickel linewidth 200 nm and period 600 nm on a SiC:H thin film on a silicon substrate results in the signal plotted in blue in part **b**, while the green section (first-order peaks) results in the green signal. It is clear in both the signal and in Fourier transforms of the two signals, shown in **c**, that the fundamental SAW order has its signal concentrated in the first-order diffraction peak, while the second-order SAW is displayed quite clearly in the second-order diffraction peak. (Note that both Fourier transforms are displayed on the same vertical scale.)

Having established this intuitive argument for understanding the changing diffraction signals we measure as the average behavior of a single unit cell within a full periodic grating sample, we can now confidently assign the various signal features visible in Fig. 2.9 to specific dynamics occurring within our samples. The time steps before time-zero (i.e. when the probe pulse reaches the sample before the pump pulse, before the sample is excited) serve as a measure of the zero-signal level, since pump-on and pump-off images would ideally be identical. The fluctuations around this level show the noise level in the signal. The average of the before-time-zero difference images can also be used to subtract out unchanging features from all the difference images — like those caused by leak-through of scattered pump light around the filters in front of the CCD.

Within the first 100 ps following time-zero, two sets of longitudinal wave dynamics are visible. The initial high-frequency oscillation corresponds to the longitudinal resonance excited within the nanostructures themselves. The two echo features visible later are due to the return to the surface of LAW pulses which are launched into a thin film layer and reflect from the buried interface with the substrate. On the nanosecond time scale, another two types of dynamics appear. The slow, exponential decay represents the thermal relaxation that follows the sudden sharp expansion at time-zero. The oscillations superimposed on this overall trend correspond to the various SAW harmonics launched in the substrate. It can be seen that later times are more dominated by one, low-frequency SAW mode while early times display more higher frequencies. This is due to the fact that damping rates tend to be faster for higher-frequency SAWs. They are confined to propagate in a region nearer the surface where they are more strongly affected by scattering from the grating structures.

2.3 Why use EUV?

The clearest benefit of using EUV beams to probe the dynamics of nanostructured systems is the lower diffraction limit that the short wavelength enables. Since the diffraction limit goes as $\lambda/2\text{NA}$ for wavelength λ and numerical aperture NA, using 30nm light rather than visible wavelengths (as small as $\approx$ 350nm) immediately offers better than a factor of ten improvement in the

small structure sizes that we can measure. EUV is also sensitive to the very short structure periods that launch the shortest-wavelength SAWs, which are important for confining measurement sensitivity within ultrathin film layers at the surface as we will see in Chap. 5 [34, 35]. Particularly at this time when the nanoelectronics industry is beginning to push the smallest features into the single-digit nanometer regime [6], sensitivity to these small sizes will be mandatory for any technologically useful characterization tool. At the same time, nanofabrication capabilities have progressed in pace with the nanoelectronics goals, meaning that single-atom layers and few-nanometer structures can now be reliably fabricated. Since this capability is such a recent development, these are precisely the size regimes where much of the governing physics remains to be discovered.

A related benefit of the short-wavelength probe is seen in the phase difference induced by surface displacements. A shorter wavelength implies a larger relative change in phase for a given displacement. Because the resulting diffraction pattern serves as an interferometric measurement of the height difference between substrate and structure surfaces, this larger phase change creates a larger change-in-diffraction signal (see Fig. 2.12). In particular, our experiments see a typical noise level of about 10^{-4} relative to the total probe intensity, implying that height changes around 10 pm are detectable, a change corresponding to $\lambda/3000$ at our probe wavelength of 30 nm.

Finally, EUV photon energies avoid extraneous contributions to signal from electronic and photoelastic effects that must be accounted for in analysis of visible-wavelength experiments (*e.g.* [36]). When the pump pulse excites the metallic nanostructures, the light is initially absorbed by the electrons within the pump-photon energy of the Fermi surface. Only after the first few picoseconds does the electronic system fully equilibrate with the atomic lattice, creating the thermal expansion we ultimately observe. However, the excited electrons cause a very large change in the index of refraction for visible light by significantly increasing the electron population available to absorption of those lower-energy photons. Thus the evolving and relaxing electron population contributes significantly to the early-time signals in visible-probe experiments [37]. This effect is largely separable by time scale from other dynamics of interest, particularly for materials with maximal difference between electronic and thermal diffusivity, although this will be less manageable

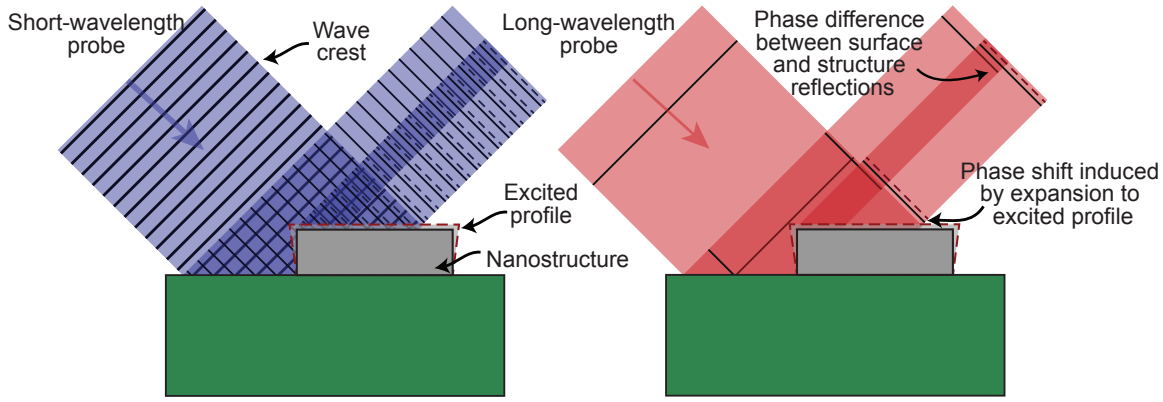

Figure 2.12: **Phase advantage from EUV beams** | The static diffraction pattern from an array of structures is determined by the reflectivities of both substrate and structure and the phase difference between the part of the beam reflected from the substrate and that reflected from the structures. This phase difference is highlighted by following the wave crests in a probe plane wave, particularly in the overlapping region of the two beams shown after reflection. The phase difference is shifted slightly when the structure is expanded, as by our pump excitation, shown by the dashed lines. The advantage of using short-wavelength EUV probes can be seen in comparing this phase shift to the full distance between wave crests for both the blue short-wavelength beam and the red long-wavelength beam. The much larger relative shift for the short-wavelength beam creates a much larger change in the diffraction signal we measure.

for smaller systems where dynamics occur on faster time scales. Notably these statements regarding negligible reflectivity changes for EUV do not apply to EUV beams near the absorption edges due to inner electron shell resonances in materials. Here the strong changes in reflectivity with sharp differences in absorption from one harmonic wavelength to the next can be exploited for element-specific measurements of material dynamics (*e.g.* [38]).

In contrast, the photoelastic effect refers to changes in the index of refraction caused by material density changes due to thermal expansion or the passage of acoustic waves. This effect will be a major contributor to signals on all timescales when the photoelastic coefficient of the observed material is large [39]. However, EUV again has the benefit of very weak coupling to these effects. Tobey *et al.* calculate that the density-induced change in reflectivity for EUV wavelengths is approximately 0.0006 — about 20 times lower than that for visible wavelengths [40]. Signal that could be attributed to such a reflectivity change would be about 50× smaller than the signals caused by displacements of the surface profile, usually below the level of noise in our data.

While the following chapters will discuss some ways that visible-probe experiments are used to address similar questions to those we study, they all require special techniques or extra signal processing to pick out the signal that is significantly smaller in magnitude than those generated by EUV probes. However, they may also offer inspiration for future improvements to our experimental technique.

2.4 Conclusion

In this chapter we have seen how the short wavelength and pulse duration of EUV light from HHG enables an incredibly sensitive probe to study any of the dynamics which deform the surface at the 10-picometer scale or above with the temporal resolution needed follow ultrafast dynamics at the nanoscale. This will include thermal and acoustic dynamics in structures as small as 20 nm in lateral size and layers as thin as 1 nm.

This chapter has also illustrated how the sample designs we choose serve several important functions. First, the preferential pump laser absorption in the metallic nanostructures creates the

impulsive stress needed to excite the acoustic resonances that will probe the mechanical properties of the substrate, thin film layers, or the nanostructures in which they are confined (as discussed in Chaps. 5 and 6). In particular, they have been used to launch the shortest-wavelength SAWs observed to date (< 45 nm) [41], which are fully confined within only the first ≈ 10 nm below the surface. Second, the nanostructures serve as nanoscale heat sources as small as 20 nm in linewidth, and their cooling rates reveal important transitions in the nature of thermal transport over short length scales, as will be explored in detail in Chap. 3. Finally, the nanowire periodicity allows for efficient diffraction of the EUV probe light, enabling the interferometric measurement with sensitivity to $\lambda/3000$ displacements and averaging over the dynamics of as many as a million individual structures to build up the strong signal we observe.

Chapter 3

New regime in nanoscale thermal transport

Critical applications including thermoelectrics for energy harvesting [42, 43, 44], nanoparticle-mediated thermal therapies in medicine [45, 46], nano-enhanced photovoltaics, controlled material processing with localized thermal annealing [46, 47] and thermal management in integrated circuits [48, 49, 50, 51] require a comprehensive understanding of energy transport at the nanoscale. Recent work has shown that the rate of heat dissipation from a heat source is reduced significantly below that predicted by Fourier's law for diffusive heat transfer when the characteristic dimension of the heat source is smaller than the mean free path (MFP) of the dominant heat carriers (phonons in dielectric and semiconductor materials) [52, 53, 54, 55, 56]. However, a complete fundamental description of nanoscale thermal transport is still elusive, and current theoretical efforts are limited by a lack of experimental validation.

Detailed study of heat-carrying phonons is very challenging for reasons summarized well by Maasilta and Minnich [57]:

> Unlike electrons, phonons have no charge and cannot be controlled by external electric or magnetic fields. Unlike photons, phonons have no benchtop source that can produce them at a particular frequency, nor can an arbitrary phonon mode be easily probed. Furthermore, whereas photons interact very weakly with each other, the nonlinear interactions between phonons are comparatively strong and responsible for thermal resistance at room temperature and above. Roughly speaking, studying phonons is akin to studying light using only light bulbs, without spectrometers, and with strong interactions between the photons. It's no surprise that thermal phonons have remained so poorly understood.

This chapter will discuss the first application of the ultrafast pump-probe technique with EUV described in Chap. 2. In particular we focus here on the thermal decay present in the change-in-diffraction signal shown in Fig. 2.9 and seek to understand how the heat flow and dissipation rates change with heat source size and geometry. By observing phonon-mediated dynamics (heat flow in non-metallic materials), we gain new understanding about their fundamental properties.

The chapter begins with a discussion of theoretical background on heat flow and the connection between macroscopic and microscopic views of thermal transport processes, as well as an overview of past experiments which have observed size-induced transitions away from continuum-level diffusive heat transfer. Then I discuss how we extend such observations to the smallest nanoscale heat sources observed to date at 20 nm in linewidth. There, through both experiment and theory we show that the size of the heat source is not the only important scale that determines nanoscale heat dissipation. We identify a new regime of thermal transport that occurs when the separation between nanoscale heat sources is smaller than the average phonon MFP [58, 59]. Surprisingly, we find that when phonons from neighboring heat sources are close enough together to interact, more of them dissipate heat in a diffusive regime, thus counteracting the inefficiency caused by ballistic phonon propagation seen in the case of isolated heat sources. This collective behavior can restore heat transfer to near the diffusive limit. Most importantly, the appearance of this new 'collectively-diffusive' regime mitigates the scaling problems for thermal management in nanoelectronics, which may not be as serious as projected [6, 53, 60].

3.1 Theoretical background

Thermal transport is generally categorized into three types: convection, radiation and conduction. Convection describes the transfer of heat by the bulk motion of material, as for magma in the earth's core or the motion of weather cells in the atmosphere, as well as smaller-scale phenomena like hot water circulating in a pot heating up on a stove.

Radiation is typically described as the transfer of energy by the emission and absorption of photons. This is the only heat transfer mechanism that does not require a material medium in which to occur since photons can carry energy across vacuum.

Conduction is the one of primary interest here. This involves the transfer of heat by microscopic movements within a material without motion of the material as a whole. In a gas or liquid, this may occur by the motions of atoms or molecules where collisions between more energetic and less energetic particles will tend to transfer heat energy from hot regions to cold. In solids, heat energy manifests as the vibrations of the atomic or molecular lattice and can be transfered by the movements of electrons in conducting materials, or by the lattice motion itself. Mathematically the lattice vibrations can be quantized as phonons populating the normal modes of oscillation of the whole lattice. Like atoms in a gas, these phonons will spread, scatter (and decay) to dissipate heat. Because all these descriptions involve collisions as the means to exchange, transfer and spread the heat, this is an inherently diffusive process.

Macroscopically, collisions will establish local thermal equilibria which create a smooth temperature gradient directing the flow of heat energy from hot regions to cold. This process is described by Fourier's law, which can be derived in one dimension by considering the phonon flux at some point x along a thermal gradient in the x direction. For a given phonon number density n and energy E, the heat flux q_x through a surface at x is given by the particle fluxes in each direction from a distance equal to what they can move at an average velocity v_x in lifetime t

$$q_x = \left(\frac{1}{2}(nE(x')v_x)\right)\Bigg|_{x-v_xt} - \left(\frac{1}{2}(nE(x')v_x)\right)\Bigg|_{x+v_xt} \tag{3.1}$$

since the random motion of phonons implies half will be moving in each direction. Applying a 1st-order Taylor expansion around $v_xt = 0$ for each component implies

$$\begin{aligned} q_x &= \frac{1}{2}\left((nE(x)v_x) - v_xt\frac{d(nE(x)v_x)}{dx}\right) - \frac{1}{2}\left((nE(x)v_x) + v_xt\frac{d(nE(x)v_x)}{dx}\right) \\ &= -v_x^2t\frac{dU}{dx} \\ &= -\frac{v^2t}{3}\frac{dU}{dT}\frac{dT}{dx} \end{aligned} \tag{3.2}$$

using the facts that $nE(x)$ gives the position-dependent energy density $U(x)$, v_x^2 is related to the overall average phonon velocity by $v_x^2 = v^2/3$, and we assume this average velocity is independent of position. Furthermore, $\frac{dU}{dT}$ is the volumetric heat capacity C, and we can approximate the thermal conductivity $K_{bulk} = \frac{1}{3}Cv\Lambda$ where $\Lambda = vt$, the average phonon mean free path. Combining this with Eqn. 3.2 gives

$$q_x = -\frac{Cv^2t}{3}\frac{dT}{dx} = -K_{bulk}\nabla T, \tag{3.3}$$

the well-known form of Fourier's law.

However, a few problems arise with this formulation once we move to thermal transport in nanoscale systems. First, the Taylor expansion assumes that $v_x t$ should be 'small'. However, since phonon MFPs in crystalline materials can vary by orders of magnitude from a few nanometers to hundreds of microns [61, 62], heat sources in the nanoscale regime and their associated thermal gradients will hardly be 'large' in comparison. Similarly, the ∇T in Eqn. 3.3 requires a continuous, differentiable thermal gradient, which can only be established by having enough collisions among heat carriers to maintain local thermal equilibria throughout the heat transport region. But at size scales below one MFP, phonons travel ballistically through the region without scattering, introducing a nonlocality to the heat transport as temperature conditions and gradients 'far' away from the heat source have an increasing role to play [63]

This transition also reveals a breakdown in the simple categorization of thermal transport that introduced this section. The ballistic motion of phonons is analogous to radiative photon transfer [64] rather than conduction, thus introducing a smooth transition between the two initially distinguishable heat flows. Ballistic transport sets an upper bound on the heat transfer rate. Phonons cannot carry heat away from a heat source faster than they themselves can move. Fig. 3.1 illustrates how this results in an over-prediction of the rate of heat dissipation by Fourier diffusion as the heat source size becomes comparable to or smaller than phonon MFPs in the substrate where heat is flowing. This occurs because the heat flux predicted by Fourier's law (Eqn. 3.3) diverges once dx is small and the temperature gradient becomes unphysically large [37]. As we will see

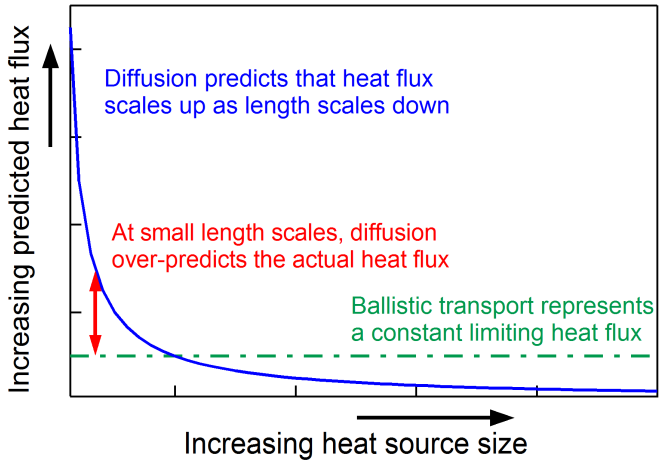

Figure 3.1: **Diffusive vs. ballistic heat flux predictions** | Because heat diffusion assumes that scaling of the heat source corresponds directly to scaling of the thermal gradient, its prediction for heat flux diverges for small heat sources (solid blue). Ballistic heat transfer represents the limiting case for heat flux as thermal energy is transported at the unimpeded speed of phonon motion (dash-dot green). The diffusive prediction is usually below the ballistic limit, but for small heat sources, the ballistic limit takes over. The diffusive over-prediction of heat flux (red arrow) can be quantified in a diffusive simulation by adding an effective resistivity term to artificially slow the diffusive heat flow.

below, this over-prediction can be accounted for by introducing an extra effective resistivity at the interface between the heat source and substrate to artificially model the lower heat flux and thereby quantify the deviation from purely diffusive thermal transport. However, the wide range of phonon MFPs present in the substrate material further complicates this picture. For a given nanoscale heat source size, phonons with MFPs shorter than the hot spot dimension remain fully diffusive and contribute to efficient heat dissipation and a high thermal conductivity (or equivalently, a low thermal resistivity). In contrast, phonons with long MFPs travel ballistically far from the heat source before scattering, with an effective thermal resistivity far larger than the diffusive prediction. Phonons with intermediate MFPs fall in between; here heat transfer is quasi-ballistic with varying degrees of reduced contributions to the conduction of heat away from the nanoscale source.

A full account of the phonon motions in a material can be obtained using the Boltzmann Transport Equation (BTE) – as long as the size scales in the system remain large enough to neglect phonon-wavelength related effects like interference. The time-dependent BTE follows the full evolution of the spatial and energy distributions of phonons in a system:

$$\frac{\partial f}{\partial t} + \vec{v} \cdot \vec{\nabla}_r f + \vec{F} \cdot \vec{\nabla}_p f = \left.\frac{\partial f}{\partial t}\right|_{collision} + s \tag{3.4}$$

where f is the time- and space-dependent carrier distribution, $\vec{p}$ is the momentum coordinate, $\vec{r}$ is the position coordinate, $\vec{F}$ is an applied force and s represents any source. The collision term must be calculated from the scattering matrix (S) element

$$\langle f(\vec{p'})|S(\vec{p},\vec{p'})|f(\vec{p})\rangle \tag{3.5}$$

Given three dimensions for each of position and momentum, plus time, the full BTE represents a seven-dimensional integro-differential equation. This poses a significant computational challenge, even for numerical models on modern high-performance computers. Even more importantly, a full account of the collision matrix requires very complete knowledge of the phonon modes throughout the full Brillouin zone and high-order force constants describing the anharmonic interactions between atoms in a lattice. Thus the complete collision matrix cannot be calculated from first principles nor can it be directly measured experimentally [65].

Several types of simplifications have been employed to make such calculations more feasible [66]. One of the most significant simplifying assumptions is that of the grey model approximation, where it is assumed that all the phonon dynamics can be approximated by a single average phonon mode with average wavelength, velocity and MFP. However, it has been shown in many cases that this assumption results in missing many important dynamics in the systems of interest today [67, 68]. Slightly less severe is to divide phonons into groups by ballistic vs. diffusive [67, 69], or propagating vs. non-propagating [66]. Accounting only for certain elastic or inelastic scattering possibilities allows more potential simplifications [62]. The relaxation time approximation has been the most broadly applied, assuming that every phonon mode is associated with one effective relaxation time to neglect the specific mechanisms and inelastic processes which cause them to decay [65]

More recent Monte Carlo methods for modeling only departures from an overall equilibrium state have offered good improvements ($\approx 10^4 - 10^6$ calculation speed improvements for typical modeling parameters) for computational efficiency [65, 70], and one study using the measured phonon dispersion of silicon as an input used such Monte Carlo simulations to successfully simulate the diffusive-to-ballistic transition in thermal resistance for heat sources smaller than dominant phonon MFPs [71]. However, while these newer methods are improving the computational efficiency and the available computational power continues to grow, the complexity of these methods and a corresponding lack of physical insight available from their results motivate the continued use and development of other models and nanoscale measurement techniques as well.

3.2 Previous work

The great technological interest in nanostructured systems and devices has both motivated a great number of experiments examining the unique dynamics that dominate small size scales and driven the progress in nanofabrication capabilities that enables the systematic study of such dynamics. In recent years, non-diffusive thermal transport has been the subject of an increasing amount of experimental effort due to its importance to nanotechnology development and to building a more

fundamental understanding of the physics of thermal transport. However, our EUV nanometrology technique continues to be the best method for observing dynamics in nanostructured systems with characteristic dimensions down to 20 nm.

There are two important effects that drive the appearance of non-diffusive (typically geometry-dependent) thermal transport. The spectrum of phonon MFPs involved in heat transfer can be modified by the increased importance of boundary scattering in nanostructures. Alternatively, the participation of phonon modes in thermal transport can be modified relative to diffusive assumptions as the heat transport distance or thermal gradient size scale becomes small compared to the MFPs. Many of the experiments addressing these effects have been reviewed in [72] and [73], but I will also highlight a number of important examples here.

Thermal transport through nanostructures (like nanowires) and near surfaces or interfaces (as in superlattices, for example) will be modified from that in a bulk material because the presence of additional scattering surfaces will affect the phonon MFP spectrum [43]. Reductions in thermal conductivity due to this mechanism have been observed in superlattices (*e.g.* [74, 75]), thin films [76, 77], nanowires [78, 79, 80] and graphene ribbons [81]. Engineering of the edge/boundary shapes and roughness can also be used to tune the degree of conductivity suppression [82]. In this way, small structures can exhibit conductivity at, and even below, the Casimir limit where thermal conductivity is dominated by boundary scattering, and is thus dependent on the size and shape of the medium [83].

Chen notes that boundary scattering effects are not the only ones at play in this conductivity modification, however [74]. When the transport distance across a layer in a superlattice, for example, is small compared to the MFP, the temperatures defined at the boundaries must be treated with care. Similarly, when graphene ribbons were made very short, the apparent conductivity depended on length simply because heat flux had reached the ballistic limit [81].

Whenever the transport distance becomes small compared to the MFP, heat transfer to the end location will become less efficient as long MFPs tend to pass through without interacting and 'dropping off' their thermal energy. This was directly observed by monitoring the x-ray diffraction

from a buried layer of 120-250 nm of In-doped GaAs to examine its thermal expansion [84]. When the layer was thin, it received less heat from an laser excitation at the surface than when it was thick. Similarly, transient-grating (TG) experiments, which induce spatially-periodic heating by interfering two pump laser beams at the sample surface, measure thermal transport across the distance from interference maximum to minimum [85]. When this distance is comparable to MFPs, heat transfer appears increasingly non-diffusive as the energy from phonons with MFPs longer than the grating period distributes uniformly over the peaks and nulls of the thermal grating, contributing nothing to the thermal transport observable by the experimental probe [37, 67]. Notably this is a very different case from our experiment which creates the spatially periodic heating with nanostructure heat sources and directly observes their thermal expansion. As illustrated in Fig. 3.2, the TG signal will disappear once the heat is uniformly distributed across the horizontal dimension, since the probe beam will no longer diffract to interfere with the reference beam. In contrast, we still observe a signal at this point, since the thermally expanded nanowires will affect the diffraction signal as long as their temperature is higher than their initial state. This means we measure the cooling rate of the nanostructures (and the full thermal relaxation of the system) with no regard to where the heat ends up. In contrast, TG experiments measure the rate of heat transfer across the specific distance from peaks to nulls, or half the thermal grating period.

This makes it clear that TG always measures the transport from effectively isolated heat sources. Most other work to date has focused on more obviously isolated micro- and nanoscale heat sources created by small thermal penetration depth (short transport distance) [53, 55, 56], laser absorption at a surface confined by pump spot size (small source size) [54], or in nanostructures (small source size) [52, 86, 87]. In all these cases, it is proposed that the apparent thermal conductivity is reduced because the contributions of long-MFP phonons to the total thermal conductivity are cut off by the small heat source size, an effect which can be described by a geometry-specific phonon suppression function [88, 89].

However, more care is needed in the interpretation of apparent conductivity suppression. The distinction between experiments which observe boundary-scattering-induced effects and those

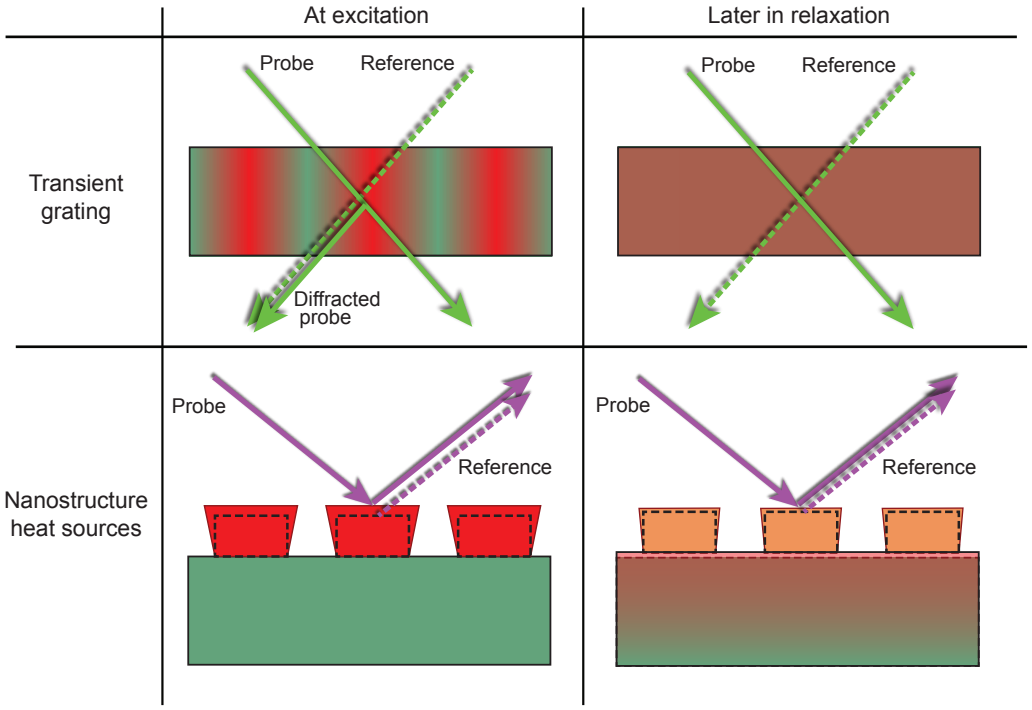

Figure 3.2: **Contrast between transient gratings and periodic nanostructures** | Transient grating measurements rely on the periodic thermal grating in a material to diffract a portion of the probe beam to interfere with a reference beam, thus constructing the signal of thermal and acoustic dynamics. Once heat has traveled from the peaks to the nulls and the layer thermalizes, the signal has fully decayed away. In contrast, the equivalent reference in the case of diffraction from nanostructure heat sources is the fully relaxed, cold system represented by the dotted lines. Each pump-on diffraction pattern is compared directly to this pump-off reference. As long as the structure temperature is different from their initial reference state, their thermal expansion will affect the probe diffraction — even after the surface of the nanostructured system has thermalized. Thus while transient gratings are sensitive to the thermal transport distance set by the period of the thermal grating, diffraction from nanostructure heat sources tracks the whole process of heat dissipation from the structures.

which observe non-diffusive transport due to ballistic phonon motion across steep thermal gradients is not as sharp as is often assumed [90]. In particular, apparent conductivity modifications should typically be anisotropic with in-plane conductivity strongly influenced by surface-scattering effects in addition to the break-down of Fourier assumptions. Notably Wilson and Cahill find that effective changes in conductivity observed in those experiments relying on varying the thermal penetration depth by the modulation frequency of a laser pump [53, 55] can be explained completely by the changes in sensitivity to thermal transport right at the surface where it is suppressed simply by extra boundary scattering[90].

These details will be an important factor to consider moving forward for accurate translation of effective conductivity measurements into characterization of the fundamental phonon properties of materials. It also emphasizes the care that is necessary when using temperature near interfaces where highly non-equilibrium phonon processes are important for determining the true heat transfer rates. Newer theoretical work has even suggested that a better account of the phonon flux at boundaries (rather than temperatures) could allow an accurate application of Fourier's law to describe ballistic thermal transport in nanostructured systems [91].

3.3 Observing non-diffusive thermal transport

The primary goal of my work on nanoscale thermal transport was to extend previous observations deeper into the nano-regime by examining heat sources that are smaller compared to the average phonon MFP Λ_{grey} than were possible to explore before, as well as to compare heat sources that are geometrically confined in two dimensions (nanodots) with those confined in one (nanowires). Using the techniques discussed in Chap. 2, we study two sets of sample gratings on two types of substrate, shown in Fig. 3.3, to pursue this goal. In particular, the change-in-diffraction signal we obtain can be used to directly extract the average thermal expansion and relaxation of each individual nanowire induced by laser heating and subsequent heat dissipation into the substrate.

3.3.1 Sample design

The first set of sample gratings includes both 1D nanowire and 2D nanodot arrays of nickel nanostructures with height $h \approx 13.5$ nm and linewidths L ranging from 750 to 30 nm. The duty cycle is fixed for all gratings in this set such that the grating period $P = 4L$. The second set also combines 1D and 2D arrays of nickel structures with linewidths ranging from 1000 to 20 nm (two linewidths, L = 30 and 100 nm, are repeated from the first set in order to compare measurements across two substrates), but the duty cycle is not fixed for all gratings. In particular, half of the gratings have the 25% duty cycle of the first set while the other half repeats each linewidth with larger period (P = 400 nm for $L < 100$ nm and P =1500 nm for $L \geq 100$ nm). Each set is fabricated in a single deposition on one substrate — on sapphire and on silicon. This way the intrinsic thermal boundary resistivity at the interface between the metallic structures and the substrate will be constant across all gratings in a given set: any variation in efficiency of heat dissipation as the structure size and period are varied can thus be attributed to different regimes of thermal transport. The sapphire substrate is transparent to the 800nm pump wavelength, while the silicon substrate has such a long absorption depth ($\approx 10\,\mu$m) that any small, uniform heating of the substrate can be neglected. The nickel nanostructure height is chosen to be smaller than the absorption depth of the pump light ensuring near-uniform initial temperature distribution inside the structures. Laser excitation of the nanostructures thus creates an array of nanoscale hot spots (lines or dots) on the surface of a cold substrate.

The use of nano-patterned structures rather than optical absorption allows us to explore the dynamics of heat sources much smaller than the diffraction limit of visible light, which represents a significant limitation to many of the experiments discussed in the previous section. The $L = 20$ nm heat sources represent a substantial improvement over the smallest structures previously observed on sapphire at $L = 65$ nm [52]. The silicon substrate also further extends L/Λ_{grey} because silicon has a larger Λ_{grey} than sapphire [52, 37]. In fact, substantial contributions to thermal conductivity in silicon have been observed from phonons with MFPs well above 1 µm [53, 37]. Furthermore,

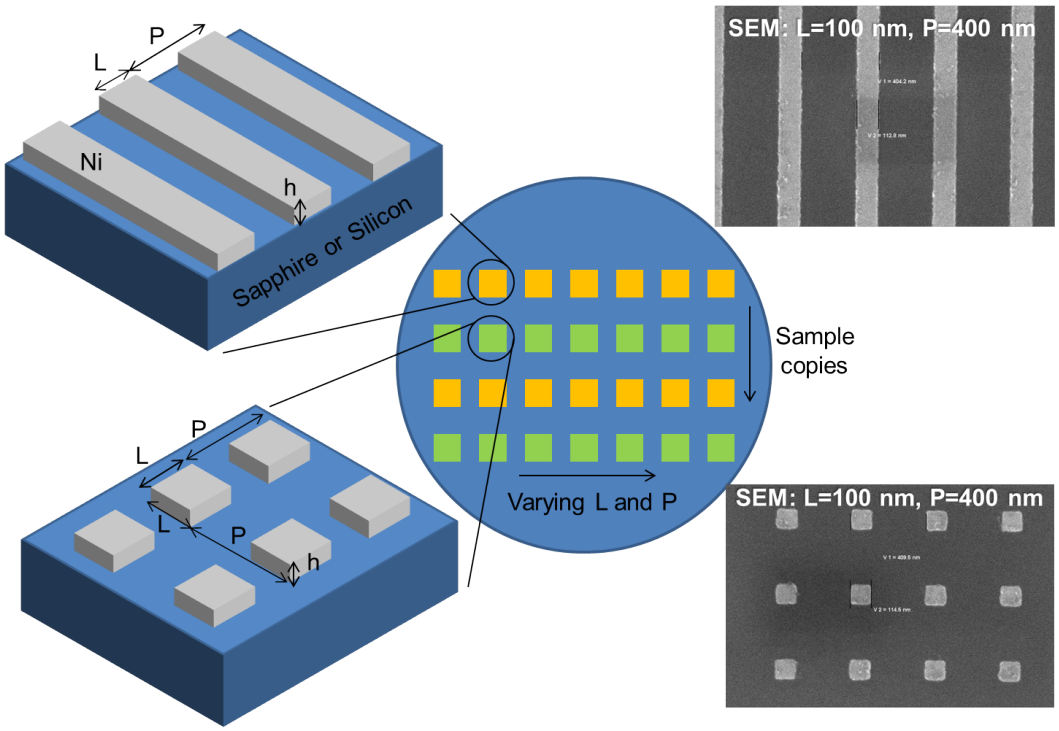

Figure 3.3: **Thermal sample layout** | We place 1D nickel nanowire and 2D nanodot arrays side by side on one substrate (shown in yellow and green squares respectively) so that differences in the heat dissipation dynamics we measure can be uniquely attributed to differences in the dimensionality of thermal transport rather than to unknown differences in the structure fabrication. The same set of linewidth (L)/period (P) pairs with structure heights h are fabricated on both sapphire and silicon substrates, allowing us to compare the trends in heat flow dynamics for two different materials. The two example SEM images of $L = 100$ nm, $P = 400$ nm gratings show that good uniformity in fabrication was achieved.

despite silicon's obvious importance to current nanoelectronics development, previous work on silicon has only addressed heat sources as small as 1 µm.

3.3.2 Quantifying deviations from diffusive transport

Unfortunately, observing the onset of non-diffusive transport as heat source size is varied is not as simple as plotting one thermal decay on top of the next and looking for slower dissipation. Heat dissipation rates for smaller heat sources will tend to be faster for both diffusive and non-diffusive cases. Instead, the cooling rates for smaller heat sources increase by less than predicted by macroscopic heat diffusion. To quantify these deviations from diffusive transport, we model the systems diffusively while allowing the thermal boundary resistivity (which sets the temperature discontinuity across the boundary between the nickel nanowires and the substrate) to vary in order to fit the thermal decay signals we measure. The intrinsic thermal boundary resistivity r_{TBR} is not expected to change with the size of the interface — at least not until the interface approaches the size scale of phonon wavelengths ($\approx 1-3$ nm) where one should begin to expect substantial changes in the interface transmittance of different phonon wavelengths. By artificially allowing changes in an effective r_{TBR}, the magnitude of variation indicates a degree of deviation from normal heat diffusion. This method is built upon that discussed by Siemens *et al.* [52], but we include more comprehensive finite element modeling of the heat transfer to reduce uncertainty in the comparison between experimental observations and the simulation output.

We model our experimental observation of the nanowire samples using a two-dimensional simulation unit cell with the plane strain approximation to follow the full thermal expansion and cooling dynamics of the nickel nano-gratings on the sapphire and silicon substrates [92]. We use measurements from atomic force microscope (AFM) characterization of our samples to set the height, linewidth and period of the structures according to the actual dimensions. The nano-grating geometry allows for periodic boundary conditions for the temperature T and the displacement $\vec{\mathbf{u}}$ on the sides of the unit cell. All mesh points are initialized at room temperature and zero displacement ($T = 293$ K, $\vec{\mathbf{u}} = 0$). The top boundaries are free to move but heat flux across them is set to zero

(no radiative heat dissipation). Continuity in the displacement is enforced at the interface between the nickel structure and the substrate, effectively joining the two materials such that no slipping is allowed. The bottom boundary is fixed and the heat flux across it is also set to zero. The height of the substrate section is set to 10 µm, much larger than the maximum thermal penetration depths of 1.7 µm in silicon and 0.7 µm in sapphire, to ensure no excess heat reaches the bottom boundary during the simulation time (up to 8 ns). An example of the top region of the unit cell geometry and mesh profile for the finite element simulations is illustrated in Fig. 3.4.

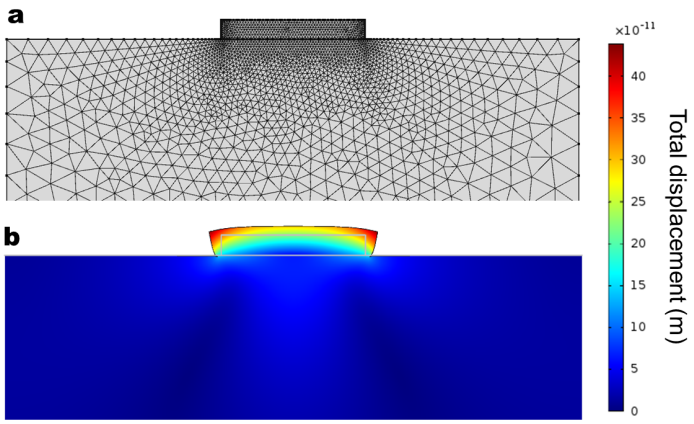

Figure 3.4: **Finite-element simulation unit cell** | **a.** The simulation mesh concentrates points inside the nanostructure and near the interface. **b.** The simulations output the time-dependent surface displacements following laser heating of the nano-grating (the surface deformation shown here is exaggerated for the purpose of visualization).

The simulations solve the coupled differential equations for the profiles of T and $\vec{\mathbf{u}}$ in the time domain including the inertial terms in the initial thermal expansion which lead to the acoustic waves that accompany impulsive laser excitation [93]:

$$\vec{\nabla} \cdot (\mathbf{c} : \vec{\nabla}(\vec{\mathbf{u}} - \alpha \Delta T_p)) = \rho \frac{\partial^2 \vec{\mathbf{u}}}{\partial t^2} \tag{3.6}$$

$$\rho C_p \frac{\partial T_p}{\partial t} + \rho C_p \vec{\mathbf{u}} \cdot \vec{\nabla} T_p = \vec{\nabla} \cdot (K_{bulk} \vec{\nabla} T_p) + Q \tag{3.7}$$

Table 3.1: Material parameters used in multiphysics simulations.

Material properties	**Nickel**	**Silicon**	**Sapphire**
C_p, Specific heat (at 300 K) [J/(kg K)]	456.8*	710.0‡	657.5*
K_{bulk}, Bulk thermal conductivity [W/(m K)]	90.9‡	149.0°	41.1*
Debye temperature (K)	450§	645§	1047§
Poisson's ratio	0.31†	0.27†	0.25†
Young's modulus [10^{11} Pa]	2.00◊	1.31☼	3.45χ
α, Linear coefficient of thermal expansion [10^{-6}/K]	12.77*	3.00~	5.21*
ρ, Density [kg/m^3]	8910*	2330☺	4000*

* Siemens et al. [52]; † Nardi et al. [92]; ‡ Desai [96]; ° Dean [97]; § Kittel [98]; ◊ Zacharias [99]; ☼ Wortman and Evans [100]; χ Wachtman et al. [101] ; ~ Okada and Tokumaru [102]; ☺ Weber [103]

where $\boldsymbol{c}$ is the elastic tensor, $\vec{\mathbf{u}}$ is the displacement, ρ is the density of the material, α is the linear coefficient of thermal expansion, T_p is the phonon temperature, C_p is the specific heat of the material, K_{bulk} is the bulk thermal conductivity and Q is the heat source term accounting for the laser heating of the nano-grating, calculated according to the two-temperature model as described by Banfi *et al.* [94].

$$Q = -\Gamma_{e-p} \cdot (T_p - T_e) \tag{3.8}$$

$$\vec{\nabla} \cdot [-k_e(T_e)\vec{\nabla}T_e] + C_e(T_e)\frac{\partial T_e}{\partial t} = P(t,y) - \Gamma_{e-p}(T_e - T_p) \tag{3.9}$$

where C_e, T_e and k_e are the volumetric specific heat, temperature and thermal conductivity, respectively, of the electrons in the sample materials and Γ represents the electron-phonon coupling of the material. (Values for nickel come from [95].) P represents the profile in time and depth below the surface of the power absorbed from the laser pump pulse, given by

$$P(t,y) = [\text{pulse peak power}] \times [\text{temporal pulse shape}] \times [\text{laser penetration}] \tag{3.10}$$

All the material properties used in the finite element multiphysics modeling are listed in Table 3.1. Given the maximum substrate temperature change induced in our experiment of ≤ 40 K, the

specific heat and bulk thermal conductivity can change by $\leq 10\%$, and we confirm that any change of this magnitude does not cause appreciable differences in the simulated time-dependent diffraction signal we use to compare with experimental data. Moreover, because we observe no pump-fluence dependence in the normalized measured signals [104], precise choices for simulation temperatures will not affect the resulting comparison with experimental data.

The more complete account of the physical dynamics in our sample allows for a more precise fit to our data and lowers our uncertainty, particular for small-linewidth samples. However, the added complexity significantly increases the computation time needed to model the full time scale of the thermal decay, especially for large linewidths, making it impractical for the large set of simulations with different r_{eff}'s required for fitting our data. Instead, we can use the comparison between complete inertial and simpler quasi-static simulations (where the right-hand side of Eqn. 3.6 is set to zero) to understand how they relate to one another (see Fig 3.5). Of particular importance is to understand how our data (which will include all the dynamics found only in the full inertial simulations) should be normalized to correctly choose the quasi-static simulation that should be considered the best fit. This relation only needs to be determined at one value of r_{eff} for a given linewidth. This is particularly an issue for large-linewidth samples where the initial inertial expansion occurs over a relatively long time scale and lateral dynamics across the wide lines strongly modify the vertical dynamics, such that there is a greater mismatch between the peak of the quasi-static simulation and that of the full inertial simulation.

The effective thermal boundary resistivity r_{eff}, which sets the temperature discontinuity, ΔT, across the boundary between the nickel nanostructures and the substrate, is introduced at the mesh points that join the two materials with the equation:

$$\hat{\mathbf{n}} \cdot (K_{bulk} \vec{\nabla} T) = -\frac{\Delta T}{r_{eff}} \tag{3.11}$$

where $\hat{\mathbf{n}}$ is the unit vector normal to the substrate surface.

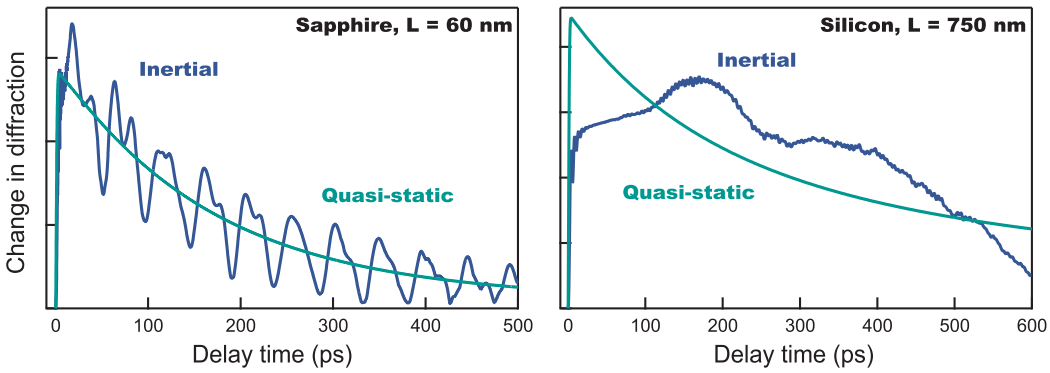

Figure 3.5: **Comparing inertial and quasi-static simulations** | Full inertial simulations of the thermo-mechanical dynamics in our samples allow a more accurate comparison to the data we measure, but they are also much more computationally expensive than simpler quasi-static simulations (which ignore the second-derivative inertial terms in Eqn. 3.6). Thus we use a comparison of these two simulations for each linewidth and substrate at the same peak temperature rise to inform how the experimental data should be normalized in order to correspond to the correct quasi-static simulation. The left panel from a small-linewidth sapphire sample provides an example of the simplest type of comparison: the normalization is such that the quasi-static curve follows the middle of the acoustic oscillations from the beginning of the scan. However, the early dynamics are more complicated for larger linewidths, as shown on the right for one of the most difficult cases. Here the lengthy onset of the first surface acoustic oscillation and the greater impact of dynamics occurring laterally across the wide structures mean that the quasi-static simulation must be normalized to a much higher value than might be naively assumed.

The simulations provide a time-dependent surface deformation profile of one unit cell, as illustrated in Fig. 3.4b. We tile this into a large array to represent our whole grating sample.

Using Fresnel optical propagation, we then calculate the diffraction patterns associated with the static, unpumped surface profile and with each time step of the deformed profile. First we construct the E-field at the sample surface E_{object} by multiplying three terms: the periodic amplitude grating formed by the different reflectivities of the substrate and grating structures; the phase grating given by $\exp(2ik * h(x))$ where $k = 2\pi/\lambda$ and $h(x)$ gives the surface height at every point x (the factor of two in the exponential function is necessary for the round trip applicable to reflection from the surface rather than transmission); and the incident EUV probe estimated by a Gaussian beam of waist radius $w_0 = 50\,\mu\text{m}$,

$$E_{probe} = w_0/w * \exp(-(x^2)/w^2) * \exp(-i(k * z_{foc} - \arctan(2z_{foc}/(kw_0^2))) * \exp(-ikx^2/(2R)) \quad (3.12)$$

where

$$w = \sqrt{w_0^2(1 + (2z_{foc}/(kw_0^2))^2)} \quad (3.13)$$

$$R = z_{foc}(1 + (kw_0^2/(2z_{foc}))^2) \quad (3.14)$$

where z_{foc} gives the distance from beam focus to sample (typically assumed to be zero, which is a good assumption for the loosely-focused beam we employ) [105]. The output field incident on our camera at distance z_{cam} from the sample is calculated using a Fourier transform by

$$E_{cam} = \frac{\exp(ikz_{cam})}{i\lambda z_{cam}} \exp\left(iX^2 \frac{\pi}{\lambda z}\right) \mathcal{F}\left[E_{object} \exp\left(ix^2 \frac{\pi}{\lambda z}\right)\right]. \quad (3.15)$$

The camera-plane coordinates X are determined by the object-plane coordinates x. Both have the same number N of evenly-spaced samples (spaced by dx in the object plane), and X extends from -$1/(2dx) \cdot \lambda z_{cam}$ to +$[1/(2dx) - 1/(Ndx)] \cdot \lambda z_{cam}$ (following MATLAB's convention that the zero-order peak will appear at the $N/2 + 1$ point for even N). The diffraction patterns are then given by $|E_{cam}|^2$. The difference in diffraction at each time step is integrated in the same way as the experimental signal is built (described in section 2.2.2). This procedure builds a simulated signal which can be directly compared to our experimental observations.

For each sample geometry, we further calculate the diffraction signals from a comprehensive set of deformation profiles related to different values of r_{eff}. The effective resistivity r_{eff} that then provides the best fit to the experimental data, like the two examples shown in Fig. 3.6, represents the sum of two terms: first, the constant intrinsic thermal boundary resistivity, r_{TBR}, that originates from the material difference between nickel and substrate [106]; and second, a correction term, r_{Corr}, due to non-diffusive transport in the substrate close to the heat source when either L or P is smaller than phonon MFPs. We also include fitting parameters to set the time offset (since the time-zero of the simulation could fall between the particular time steps we measure in the experiment) and normalization of our change-in-diffraction signals.

Notably this method assigns the effect of non-diffusive transport *in the substrate near the heat source* to a term which is specifically located *at the interface between them.* While this is a similar effective correction for non-diffusive transport near isolated nanoscale heat sources as that employed in previous works [37, 53, 54, 55, 56], by assigning the non-diffusive contribution to the thermal boundary resistivity rather than to changes in the thermal conductivity of the substrate, we maintain a simple modeling geometry while automatically limiting the effective changes to an area near the interface without having to assume a particular region of the substrate in which an effective conductivity change should apply. However, ongoing work is further exploring the connection between the two methods, as discussed below in Section 3.5.

3.3.3 Experimental results

The effective resistivity results of this analysis are plotted in Fig. 3.7. For large linewidths on both sapphire and silicon substrates, the effective resistivity converges toward a constant value which we associate with the intrinsic thermal boundary resistivity. As the linewidth approaches the dominant phonon MFPs in the substrate, the effective resistivity rises as thermal transport becomes quasi-ballistic and the contribution to heat dissipation of long-MFP phonon modes is suppressed [52, 54, 88]. This behavior was successfully described in past work using a simple grey model for sapphire and fused silica, which assumes a single phonon MFP to loosely describe a

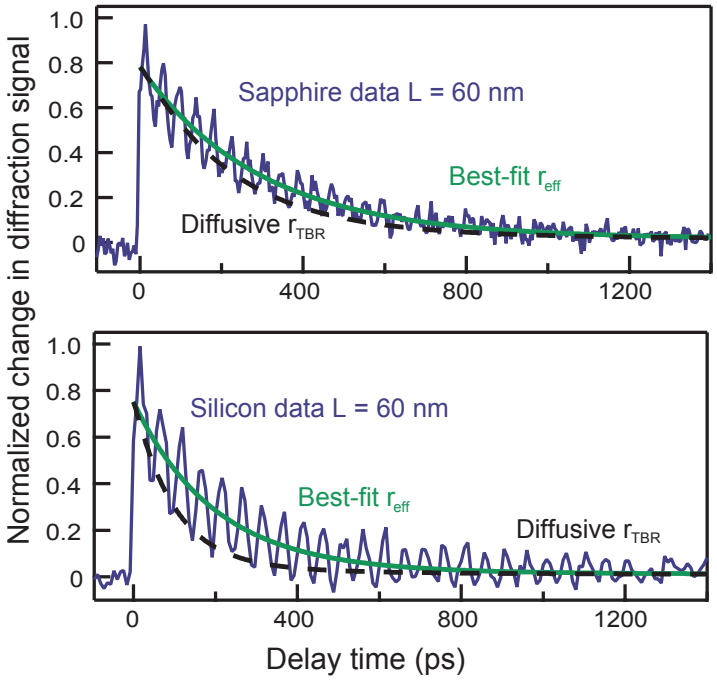

Figure 3.6: **Extracting thermal boundary resistivity from dynamic EUV diffraction** | The dynamic diffraction signals from 60nm-wide nickel lines on sapphire (top) and silicon (bottom) display a sudden rise due to impulsive thermal expansion following laser heating, a long decay due to thermal relaxation and oscillations due to surface acoustic waves. Dashed black lines plot the diffusive prediction for the thermal decay. Clearly it significantly underestimates the thermal decay time for both cases shown. Green lines plot the decay obtained from the best-fit effective thermal boundary resistivity.

weighted average of the MFPs from all the phonon modes contributing to thermal transport in a given material. According to this model, a ballistic correction term proportional to $\Lambda_{grey}/(L/2)$ can be added to the intrinsic thermal boundary resistivity [52, 106]; this prediction is plotted in red in Fig. 3.7.

However, as the linewidth (and period) shrinks further, Fig. 3.7 shows that the effective resistivity starts to decrease rather than continuing to increase [58, 59]. The constant grating duty cycle for our series of samples means that the smallest-linewidth nanowires are also those with the smallest separation between neighboring heat sources. Thus, for small linewidths the separation becomes comparable to dominant phonon MFPs, and we must develop a new theory to take this into account in order to describe this previously unobserved and unpredicted phenomenon. Notably for silicon, the peak in r_{eff} is shifted toward longer linewidths/periods compared to sapphire because the phonon MFP distribution in silicon is also shifted toward longer MFPs; *i.e.*, silicon has a longer average MFP than sapphire [37, 52].

Figure 3.8 illustrates the differences between the three regimes of heat transport from nanoscale heat sources represented by the colored background in Fig. 3.7 – purely diffusive, quasi-ballistic and collectively-diffusive. Quasi-ballistic transport (Fig. 3.8b) dominates when the size of isolated nanoscale heat sources is smaller than dominant phonon MFPs. In the new collectively-diffusive regime we uncovered (Fig. 3.8c), the separation between heat sources is small enough that long-MFP phonons, whose contribution to heat dissipation would normally be limited by the small size of nano-heat sources, can once again play a significant role and restore heat transfer efficiency to near the diffusive limit. Although these phonons travel ballistically away from each individual heat source, they can scatter with phonons originating from a neighboring heat source, thus creating an effectively larger heat source size. In the limiting case, the spacing between heat sources vanishes and this regime approaches heat dissipation from a uniformly heated layer.

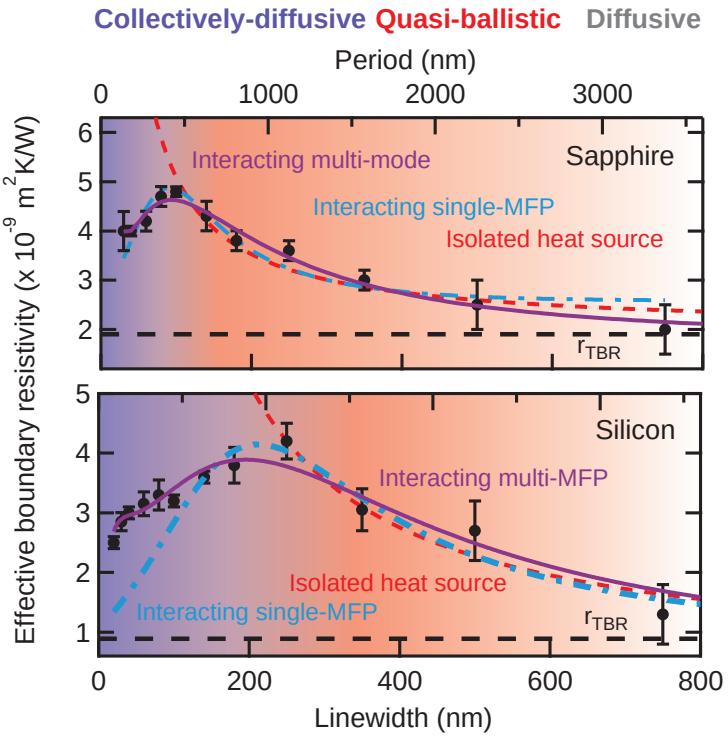

Figure 3.7: **Effective thermal boundary resistivity in sapphire and silicon** | The extracted effective resistivities for each linewidth L on both sapphire and silicon substrates increase with decreasing linewidth until the periods (equal to $4L$) are comparable to the average phonon MFP. For smaller periods (spacing), the effective resistivity decreases and approaches the diffusive limit (black dashed line), which was determined by fitting the large-linewidth data to extract the asymptotic value. The error bars represent the standard deviation among multiple data sets for the same linewidth samples. Dotted red lines: predictions for isolated heat sources based on the grey model. Dash-dot blue lines: grey model including the onset of the collectively-diffusive regime. Solid purple lines: more complete model that includes contributions from multiple phonon MFPs.

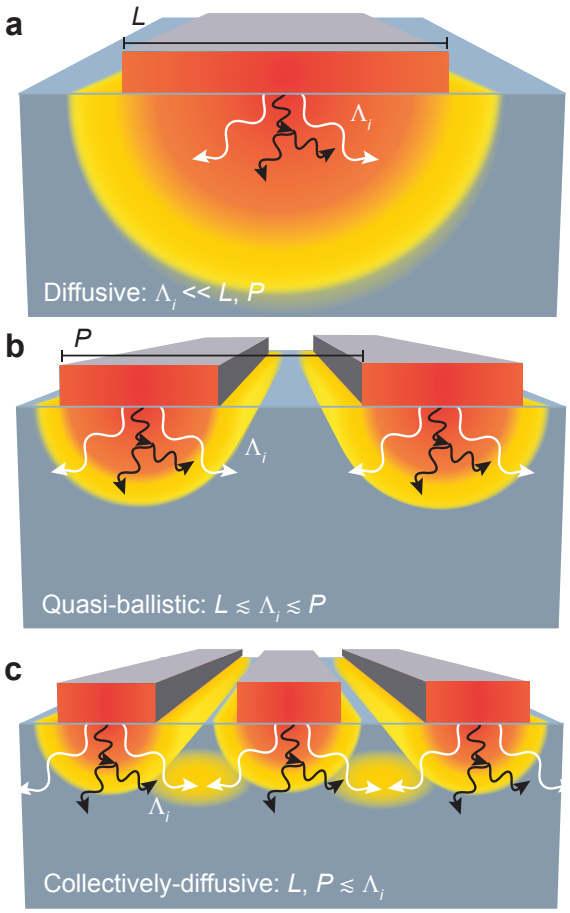

Figure 3.8: **Illustration of three thermal transport regimes** | Nanoscale heat transport is determined by the interplay between three length scales: the size of the heat sources L, the spacing of the heat sources P, and the MFPs Λ_i of heat-carrying phonons. Materials support a broad distribution of MFPs, represented here by short (black) and long (white) MFP phonons. **a.** When all MFPs are smaller than L, heat dissipation is fully diffusive. **b.** As L shrinks, long-MFP phonons travel ballistically until they are relatively far from the heat source, decreasing the rate of heat dissipation relative to diffusive predictions. Short-MFP phonons remain diffusive. **c.** When both L and P shrink, long-MFP phonons originating from neighboring heat sources interact as they would if they originated from a single, large heat source, enabling more efficient diffusive-like heat transfer.

3.4 Understanding a new thermal transport regime

To better understand and quantify the different regimes of thermal transport illustrated in Fig. 3.8, we consider three models: 1) the model described in our previous work that assumes isolated heat sources [52]; 2) an analytical model we develop here to account for interactions of phonons originating from neighboring heat sources using a grey, single-phonon-MFP approximation; and 3) a more advanced interacting model that includes a distribution of phonon MFPs.

3.4.1 Quasi-ballistic model for isolated heat sources

First, though we have already observed that isolated heat source theories will not be sufficient to explain or predict the r_{eff} trends we find in our experiment, it is important to understand the origin and implications of the model proposed by Siemens *et al.* [52] in order to implement the modifications required to account for closely-spaced heat sources. Moreover, a new and more comprehensive model must still reproduce the trends of the isolated model for the appropriate limiting cases.

Chen [64] and Siemens *et al.* [52] focused on the ratio of ballistic to diffusive heat flux near nanoscale heat sources to develop a sense for when and how ballistic contributions would become a significant factor to consider. This yielded a dependence proportional to $\Lambda_{grey}/(L/2)$. However, the connection between this ratio and the effective resistivity correction was not clear. Instead we can gain more insight into this connection by examining the full expressions for the approximate constriction resistance derived by Wexler [107] and Prasher [108].

For the 1D nanowire samples of focus in this work, the heat flux in the periodic sample can be fully represented by the unit cell with the flux between concentric half-cylinders: one of radius $L/2$, one of radius $P/2$, both centered at the center of the nanowire. Ballistic transport between the cylinders is phonon radiation with heat flux $q_{ballistic}$ governed by the phonon blackbody equation

$$q_{ballistic} = \frac{Cv}{4}\Delta T \tag{3.16}$$

where C is the volumetric heat capacity, v is the phonon group velocity and ΔT represents the

temperature difference between the two cylinders [108]. The resistivity associated with this heat flux component is given by $r_B = \Delta T/q_{ballistic} = 4/Cv$, containing no dependence on MFP, L or P. Given that the thermal conductivity K_{bulk} can be approximated by $\frac{1}{3}Cv\Lambda_{grey}$, this can be re-written as

$$r_B = 4\Lambda_{grey}/3K_{bulk} \ . \tag{3.17}$$

Diffusive heat flux between the cylinders from the Fourier equation is given by

$$q_{diffusive} = \frac{K_{bulk}\Delta T}{\ln(P/L)L/2} \tag{3.18}$$

so that

$$r_D = \frac{\ln(P/L)L/2}{K_{bulk}} \ . \tag{3.19}$$

Here the $\Lambda_{grey}/(L/2)$ dependence for the ratio of r_B/r_D is clear, but it must also be emphasized that r_B is not itself equivalent to the ballistic correction r_{BC} term employed by Siemens *et al.* [52]. To relate r_B and r_D to the varying r_{Corr} we observe, we must consider the manner in which we represent these two constriction terms by a single diffusive term. Specifically we set the sum equal to one diffusive term with a modified thermal conductivity, K_{nano}.

$$\frac{\ln(P/L)L/2}{K_{bulk}} + 4\Lambda_{grey}/3K_{bulk} \equiv \frac{\ln(P/L)L/2}{K_{nano}} \ . \tag{3.20}$$

Then the resistivity correction will be related to the effective conductivity change represented here.

$$\frac{1}{K_{nano}} - \frac{1}{K_{bulk}} = \frac{4\Lambda_{grey}}{3K_{bulk}\ln(P/L)L/2} \ . \tag{3.21}$$

$r_{Corr,iso}$ is then related to the difference in heat flux induced by this modified thermal conductivity at radius d which encloses the finite region in which non-diffusive effects are important.

$$r_{Corr,iso} = \frac{d}{K_{nano}} - \frac{d}{K_{bulk}} = \frac{4\Lambda_{grey}d}{3K_{bulk}(L/2)\ln(P/L)} \tag{3.22}$$

The size of the region where ballistic effects are important should be determined only by the phonon MFP distribution, so while d can depend on Λ_{grey} of the substrate, it should have no dependence

on L or P. Thus the proportionality to $\Lambda/(L/2)$ is maintained and the finite region where the conductivity change should apply is built in.

However, some problems do remain with the details of this approximate result. Most importantly the limiting case where $P = L$ implies a divergent r_{Corr} though it should imply a return to normal diffusion. Also, as $P \to \infty$, r_{Corr} in this expression will always go to zero even though small L with large P should imply a large r_{Corr}. Because of these problems with the precise form of the proportionality constant, as we develop a new model for incorporating the effects of close spacing on the heat transfer, we will seek to reproduce the $\Lambda_{grey}/(L/2)$ dependence for isolated heat sources and leave the rest to a scaling constant that we fit to the data.

3.4.2 Interacting heat sources, grey phonon approximation

The quasi-ballistic model for isolated heat sources clearly fails to capture the experimental observation that heat source spacing influences the effective r_{Corr}, and a new model for r_{Corr} is required to account for the transition to the new collectively-diffusive regime. As illustrated in Fig. 3.8, the transition from the diffusive to quasi-ballistic regime can be qualitatively attributed to a loss of phonon collisions near enough to the small heat sources to be adequately described by normal heat diffusion. This effectively suppresses the efficiency of heat transfer via long-MFP modes relative to the diffusive prediction. But if another heat source is placed nearby such that the long MFPs allow more overlap in the region between the heat sources, it is reasonable to observe that the scattering locations are once again 'close enough' to a heat source to appear more diffusive-like. Indeed the long-MFP phonons do not 'know' that they are propagating away from two small heat sources rather than one large source. Note that this qualitative description does not suggest a change in scattering rates (which would imply changes in the MFP distribution) or that phonons originating from the neighboring heat sources must specifically interact with each other. Rather, the scattering events for long MFPs transition from diffusive-like to non-diffusive-like and back to diffusive-like depending on the distance from the heat sources.

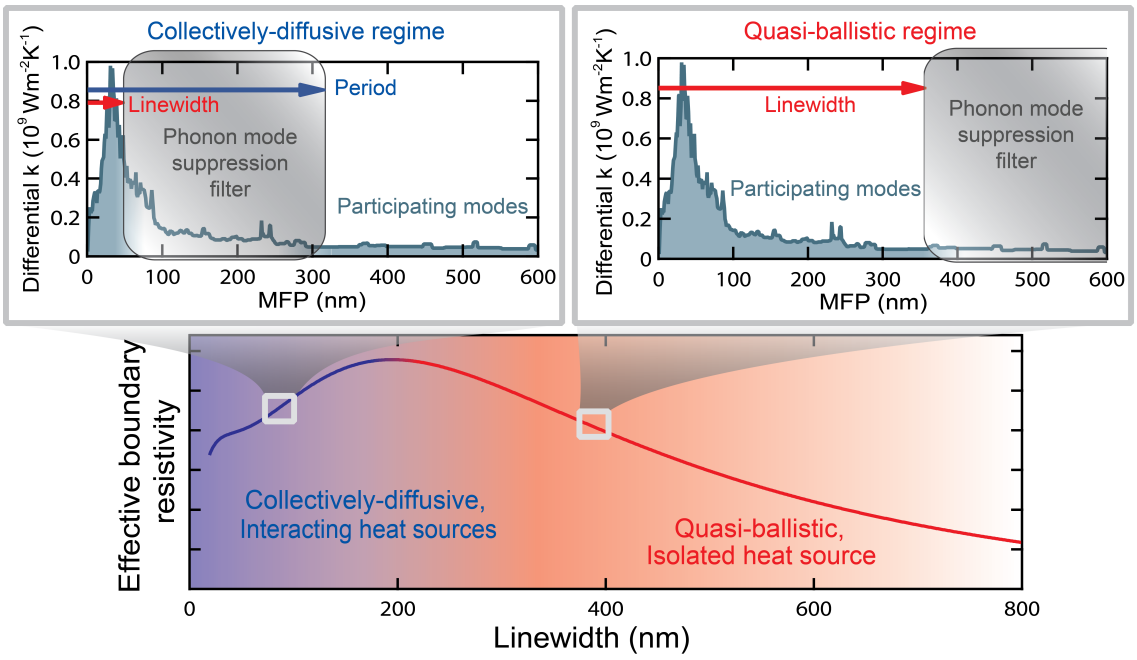

Figure 3.9: **Phonon filter model schematic** | Linewidth and period define a suppression filter for phonon MFP spectra. The observed increase in effective thermal boundary resistivity for small linewidths L is due to the suppression of the contribution to thermal conductivity of phonon modes with MFP larger than L. Decreasing the period P can reactivate modes with MFP larger than P, decreasing the effective resistivity. In the limiting case of a uniformly heated layer, P approaches L and all phonon modes participate in thermal transport. We use as an example the smoothed differential conductivity distribution for silicon (top graphs, green line), calculated from first-principles density functional theory [59].

Given this qualitative picture of the how closely-spaced heat sources can build the conditions for collective diffusion, we postulate that the conductivity contributions of phonon modes are suppressed according to the model for isolated heat sources as heat source size becomes smaller than the phonon MFP, but then smaller spacing reintroduces those contributions in the same way. This can be represented by a notch filter in the MFP spectrum to describe the effects of grating linewidth and separation, shown schematically in Fig. 3.9. The notch filter suppresses the contribution of phonon modes with MFPs that fall between the linewidth L and period P of the nano-gratings. Thus, if the grating period (separation) remains large while the linewidth is decreased, one would expect the effective boundary resistivity to continue to rise, as shown in the red dotted lines of Fig. 3.7. This is because the contributions of all phonon modes with MFPs longer than the linewidth L are suppressed in the quasi-ballistic regime of isolated heat sources. On the other hand, if the grating period shrinks, long-MFP phonon modes start to contribute again since phonons originating from neighboring heat sources interact with each other as they would in a bulk system. So the effective boundary resistivity should recover toward the bulk value, as seen experimentally in Fig. 3.7.

To build an analytical expression for r_{Corr} based on this idea, we use the concept of a phonon conductivity suppression function, $S(L, P, \Lambda)$, similar to those described by others [67, 88, 109]. This suppression function is applied to a bulk differential conductivity spectrum versus phonon MFP of the substrate, $k(\Lambda_i)$, to calculate an effective nanoscale conductivity K_{nano}:

$$K_{nano} = \sum_i k(\Lambda_i) \cdot S(L, P, \Lambda) \ . \tag{3.23}$$

We then relate r_{Corr} to the change in conductivity represented by this suppression.

$$r_{Corr} = A \left(\frac{1}{K_{nano}} - \frac{1}{K_{bulk}} \right) \tag{3.24}$$

where A collects geometrical constants discussed in section 3.4.1 and K_{bulk} is the bulk conductivity of the substrate, simply given by $\sum_i k(\Lambda_i)$.

From physical arguments it is clear that for a given phonon MFP Λ_i, S must approach unity in the diffusive regime when both L and P are large and at the limit of uniform heating when $L = P$.

Furthermore, for the limit of small, isolated heat sources when $L \to 0$ but P is large, $S \to L/(2\Lambda)$ to reproduce the behavior of the quasi-ballistic model discussed above. Finally, the effects of L and P should be uncoupled and the same but opposite to each other so that L suppresses phonon mode contributions in the same way as P reactivates them. In addition, we assume that the filter function should be smooth. The relevant non-dimensional variables are L/Λ and P/Λ. All of this behavior is captured by a special case of the generic family of logistic functions:

$$S_L(L/\Lambda) = \tanh(L/2\Lambda) \tag{3.25}$$

$$S_P(L/\Lambda) = 1 - \tanh(P/2\Lambda) \tag{3.26}$$

$$S_{total}(L, P, \Lambda) = S_L + S_P \tag{3.27}$$

These functions are plotted in Fig. 3.10 where we can see the similarity between the shape of S_{total} and standard notch filters.

While more rigorous methods of deriving suppression functions for various experimental geometries are currently being explored [67, 89, 110, 111], none have yet sought to account for closely-spaced heat sources or an accompanying reintroduction of phonon modes. Equation 3.27 represents the first attempt to include the contribution of heat source spacing and offers a model which is simple enough for fast integration into existing models of heat transfer in nanoscale devices, for example, but complex enough to capture the previously unobserved behavior and make successful predictions.

To test this new model for r_{Corr}, we first assume the simple single-MFP (grey) model (where the MFP distribution is a delta function). The resulting predictions are shown in the blue curves in Fig. 3.7. Specifically, r_{Corr} in this case is given by:

$$r_{Corr,grey}(L, P) = \frac{A}{K_{bulk}} \left(\frac{1}{S(L, P, \Lambda_{grey})} - 1 \right) . \tag{3.28}$$

Fitting this interacting model to the r_{eff} data for sapphire, we extract values for r_{TBR} and Λ_{grey} which are consistent with previous results [52]: $\Lambda_{grey} = 131 \pm 11$ nm, $r_{TBR} = 2.58 \pm 0.19 \times 10^{-9}$ $\mathrm{m^2K/W}$. This good agreement with the previous larger-linewidth data and the accurate fit for the

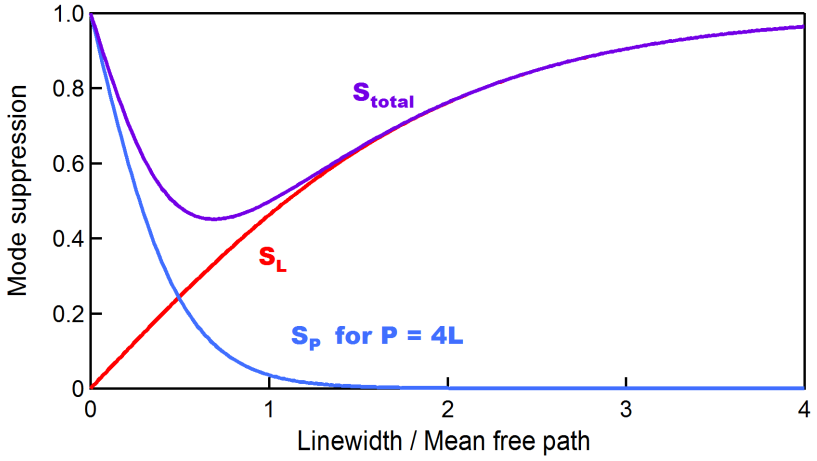

Figure 3.10: **Phonon suppression filter function** | For a phonon mode with a given mean free path, S_L describes the suppression of this mode's contribution to thermal conductivity as the linewidth of a heat source decreases. For large L/Λ it approaches unity as required for the diffusive limit. As $L \to 0$ the linear relationship to $L/2\Lambda$ is clear. S_P undoes this suppression, and S_{total} represents the total suppression when both small heat source size and interaction between heat sources are taken into account. Note also that each configuration for L and P can be related to one most-suppressed MFP (minimum of S_{total}). This information is used to partition the MFP spectrum into bins by the distribution of sensitivity to suppression of the different spectral regions given by our set of linewidth-period pairs, as discussed further in Chap. 4.

full range of our data validate our interacting r_{Corr} model as an improved method to account for nanoscale size effects in heat transport – for both quasi-ballistic and collectively-diffusive regimes. Interestingly, this single-MFP model provides a reasonable approximation for the entire range of heat transport in sapphire.

For silicon, the interacting r_{Corr} follows the general shape of the data and yields $\Lambda_{grey} = 306\pm$ 17 nm, which is consistent with previously reported values [37, 77]. However, the interacting grey-model approach, although more successful than the isolated model, fails to capture the additional structured tail in effective resistivity that appears for very small linewidths and periods, below L = 100 nm. The failure of this approach is not surprising, since the single-MFP model is known to be a poor approximation for silicon with its broad distribution of phonon MFPs [67, 88, 112].

3.4.3 Interacting heat sources, full phonon distribution

To successfully fit the silicon data, we must account for the full phonon distribution. To make this extension, we simply apply the same suppression function to each individual MFP-dependent contribution to thermal conductivity to calculate an effective $K_{nano} = \sum_i k(\Lambda_i) \cdot S(L, P, \Lambda_i)$.

The resistivity correction for heat transport from interacting nanoscale heat sources can again be related to the change in conductivity imposed by the suppression function:

$$r_{Corr,int} \propto \frac{1}{K_{nano}} - \frac{1}{K_{bulk}} \tag{3.29}$$

which gives:

$$r_{Corr,int}(L, P) = A \left(\frac{1}{\sum_i k(\Lambda_i) S(L, P, \Lambda_i)} - \frac{1}{\sum_i k(\Lambda_i)} \right) . \tag{3.30}$$

This more complete model can be used in combination with calculated differential conductivity distributions (like the one shown in Fig. 3.9) to test how well they can account for our observations of r_{eff}, including in particular the structured tail we observe for the silicon substrate. It can also be inverted to allow the extraction of differential conductivity information from r_{eff} data, as will be discussed in Chap. 4. This more complete fit to the data results in the purple curves shown in Fig. 3.7. While the grey model assuming a single MFP yielded a reasonably good approximation for

sapphire only, the r_{eff} data from both sapphire and silicon are well fit by including the extension to multiple MFPs.

While no models are fully 'correct', some are useful, and we can test the utility of this model by examining its implications. In particular, it makes the rather surprising prediction that nanoscale heat sources placed close together will cool more quickly than those that are isolated or spaced far apart from each other (see Fig. 3.11). This is due to the wide suppression filter associated with large spacing compared to the narrow filter associated with small spacing.

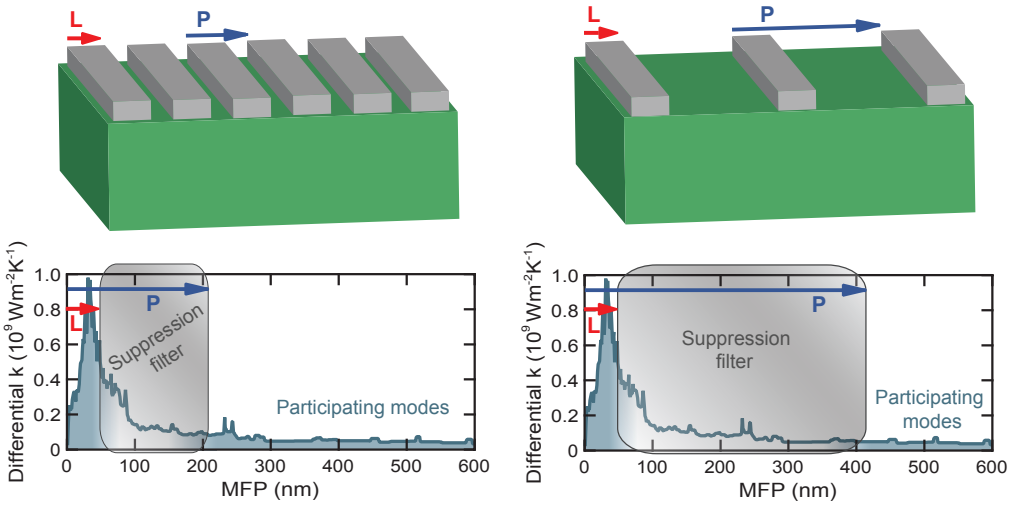

Figure 3.11: **Suppression filter model predictions** | The narrow conductivity suppression filter associated with small heat sources spaced closely together (left) predicts that heat sources in this arrangement will dissipate heat more quickly than the same size heat sources with wide spacing. Suppressing a smaller portion of the MFP spectrum maintains higher effective conductivity in the substrate and allows heat transfer closer to the diffusive limit.

This prediction is in opposition to what would be expected from an argument relying solely on shifting measurement sensitivity as discussed by Cahill and Wilson [90]. Fig. 3.12 represents this sensitivity argument schematically. It argues that when heat transfer is predominantly 1D in character with heat traveling primarily perpendicular to the interface between our nanostructure heat sources and the substrate, it will appear diffusive since the heat source size should not affect thermal transport in this direction. This situation would apply both to large heat sources and to

small heat sources closely spaced (when the lateral thermal gradient is small relative to the case of an isolated heat source). Deviations from diffusive, bulk heat transport would arise when heat flow becomes more 2D, as from small, isolated heat sources, because the surface plays an important role in modifying the heat current nearby by changing the MFP spectrum, and because the length scale of the thermal gradient becomes small in this direction. However, for the same small heat source with neighbors, the cross-plane heat current J_z should be identical while the in-plane heat current J_x would be smaller in the case where the heat sources are closely spaced. Therefore the overall heat current, and thus rate of heat dissipation, would be smaller for small, closely-spaced heat sources than for isolated or widely-spaced heat sources of the same size.

Both this sensitivity argument and our suppression function model can qualitatively explain the trends we observe in r_{eff} — transitioning from fully diffusive to higher resistivity as heat flow becomes more 2D in nature, and then back toward diffusive when the heat sources are close enough to diminish the lateral temperature gradient. However, an observation which directly compares the heat dissipation from the same linewidth heat sources at different periods will distinguish between the two model predictions. Using the set of periodic nickel nanowires on silicon with varied duty cycle, we directly observe that closer spacing does result in faster cooling. For example for both $L = 20$ and 30 nm (shown in Fig. 3.13) the blue curves with small period decay more quickly than the red curves with large period. Without any appeal to model comparisons, these data demonstrate unequivocally that the 1D-2D transport sensitivity argument is not sufficient to explain our observations. Furthermore, our new model successfully predicted this unexpected outcome, lending support for the utility of the phonon-suppression filter model.

3.5 Alternate understanding through effective conductivity

In principle, our new formulation for r_{Corr} in Eqn. 3.30 explicitly links our effective resistivity representation of non-diffusive effects in nanoscale thermal transport with the effective conductivity representation used by others. To test this link, we can fit our change-in-diffraction signals to simulations in which the substrate thermal conductivity is varied rather than the thermal boundary

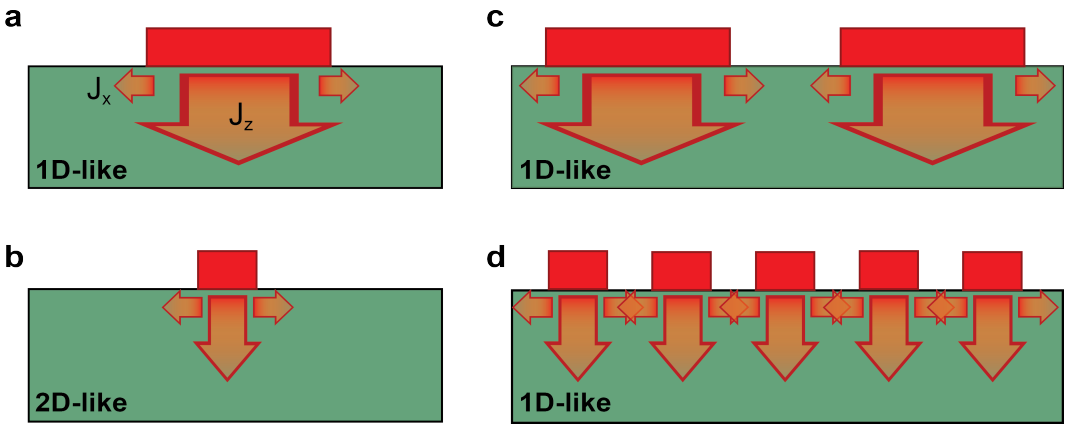

Figure 3.12: **Testing a measurement-sensitivity explanation of observed dynamics** | An explanation based on shifting measurement sensitivity from sample to sample makes predictions opposite to that of the phonon suppression filter model. Considering first isolated heat sources, when the heat source is large (**a.**), most of the heat current J is in the z direction, so while J_x will be governed by a modified MFP spectrum due to its proximity to the surface and lowered compared to heat diffusion in the bulk, it does not contribute significantly to the overall heat flux and will therefore not affect the measurement enough to be observed. When the heat source is small (**b.**), J_x is a more significant fraction of the total heat current, so its lower value will make the measurement appear to deviate from diffusive predictions as heat flow transitions to this more 2D nature. When the heat sources are no longer isolated, both large and small heat sources would display predominantly 1D heat flow as J_x is always a small perturbation due to the small lateral temperature gradients, particularly in (**d.**). Note however that J_z should be the same for both (**b.**) and (**d.**) while J_x would be smaller for case (**d.**), therefore yielding a lower total heat current. But this is contrary to the experimental results we observe.

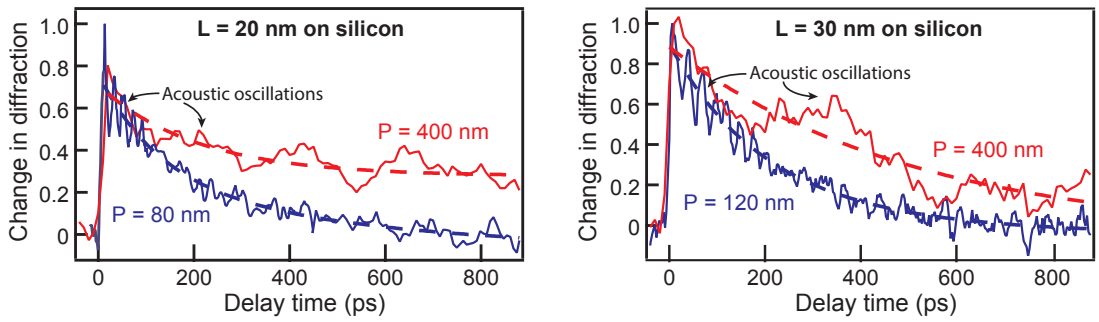

Figure 3.13: **Confirming predictions for closely-spaced nanoscale heat sources** | Our new suppression function model and the arguments for measurement sensitivity to 1D or 2D thermal transport make opposite predictions for the heat dissipation rates of nanoscale heat sources which are closely spaced compared to those far apart from each other. Here we observe that small-linewidth heat sources on silicon cool more quickly at small periods (blue) than the same size with large period (red). This behavior is only predicted by our new model for the phonon suppression filter.

resistivity. However, we quickly find that when we allow the conductivity to vary everywhere in the substrate as other works have done, it is impossible to find a good fit to the full time ranges of our data. One example is shown in Fig. 3.14. This observation is intuitively satisfying, since effective conductivity accounts for the deviations from diffusive heat transfer that should only occur within the first few MFPs from the heat source.

Instead we must explicitly include d, the length scale associated with the conversion from conductivity to resistivity that sets the region of the substrate over which the thermal conductivity is effectively modified. Thus far we have assumed this single parameter should apply for all MFPs, although one possible future improvement would be to allow it to vary with MFP. Fig. 3.15 shows how it is implemented in the simulation by adding a layer of thickness d at the top of the substrate where the thermal conductivity is set to K_{nano}; below this layer the conductivity is set to K_{bulk}. One can also observe that this is also an approximate way to implement anisotropic changes in K since the full layer of modified K_{nano} will affect in-plane thermal transport everywhere and cross-plane only before the heat crosses the lower boundary.

This procedure adds a fit parameter to the optimization algorithm since r_{TBR} must still also be fit using our data. However, it does introduce the opportunity for some comparisons that reassure our physical intuition. The first thing to note is that the need to use d to achieve a good fit to the thermal decay data is most apparent for large-linewidth samples. This can be understood by considering the time scale of thermal decay t and the corresponding thermal penetration depth, approximated by Fick's Second Law as $2\sqrt{\frac{K_{bulk}}{\rho C}t}$. As shown in Fig. 3.16, the longer measurement time scale for large linewidths implies heat can travel a larger maximum distance. If this distance is larger than d, a transition in the thermal transport behavior from quasi-ballistic to diffusive at large distances from the heat source will be required to fit the thermal decay data, requiring a transition from effective to bulk conductivity. In contrast, the short time scales of small-linewidth decay measurements imply the heat may only penetrate some fraction of the layer in which thermal conductivity is effectively modified. Thus the thermal penetration depth corresponding to the

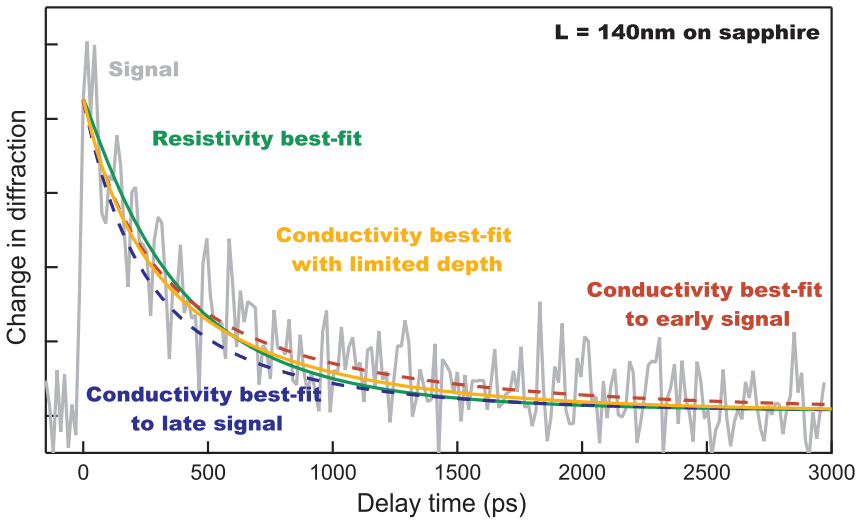

Figure 3.14: **Fitting data with effective conductivity** | When we try to model our data by varying effective conductivity rather than effective resistivity, we quickly find that reasonable fits to the whole time range of our signals require that the effective conductivity change only occur within a limited depth below the nanostructures. The original effective resistivity fit (solid green) to the data (grey) can be fit by a low effective conductivity at early times (dashed red) or a high effective conductivity at late times (dashed blue). The effective conductivity with limited depth (orange) can fit the whole range of time delays as well as the original resistivity fit.

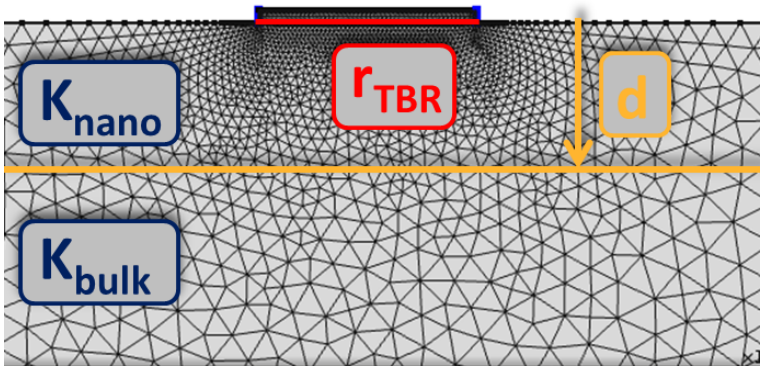

Figure 3.15: **Effective conductivity simulation cell** | Implementing an effective conductivity in a limited region within the substrate below our nanostructure heat sources requires an extra layer in the simulation cell. Within this layer of thickness d, the thermal conductivity is equal to K_{nano}. Outside, the thermal conductivity is set to the bulk conductivity value K_{bulk} taken from literature. The data fit is also strongly affected by a third fit parameter, r_{TBR}. The coupling of these three parameters makes it difficult to find unique solutions to fit the thermal decays we observe.

largest linewidth which displays no significant dependence on d when fitting the data provides a lower bound for this fit parameter.

Moreover we find that an initial fitting series which allows d to vary as a function of linewidth verifies that a single d can be chosen to allow good fits for all linewidths. And this d is equivalent to one or two times the Λ_{grey} we find through fitting our data with the grey suppression function model. This result is intuitively satisfying since it suggests the region of effective conductivity modification should be confined within one or two average MFPs of propagation away from the heat source. However, it is difficult to decouple the effects of d, K_{nano} and r_{TBR} to find a unique solution. Further improvement of the fitting methods will be necessary to enable a full analysis in effective conductivity.

If this fitting procedure can obviate the need for the proportionality constant A present in the resistivity formulation (Eqn. 3.30), this method will provide a simpler method going forward and extending this work to 2D nanodot heat sources, as well as to samples without fixed duty cycle where we are not yet sure if and how the proportionality constant should vary. It can also offer a more direct comparison to other experiments and theoretical work in this field where the use of effective thermal conductivity is the norm. In particular it will allow us to directly examine the validity of the first theoretical work that begins to explore the realm of periodic rather than isolated heat sources [113].

3.6 Outlook for the study of nanoscale thermal transport

3.6.1 Extension to 2D heat sources

While this chapter has focused thus far on 1D nanowire heat sources, we expect the quasi-ballistic phonon transport effects should be even more pronounced for 2D nanodot heat sources where the spatial confinement limits transport in two directions rather than only one. To enable as direct a comparison of these dynamics as possible, both nanowire and nanodot arrays are fabricated on the same substrate with the same sets of linewidths and periods as shown in Fig. 3.3. The

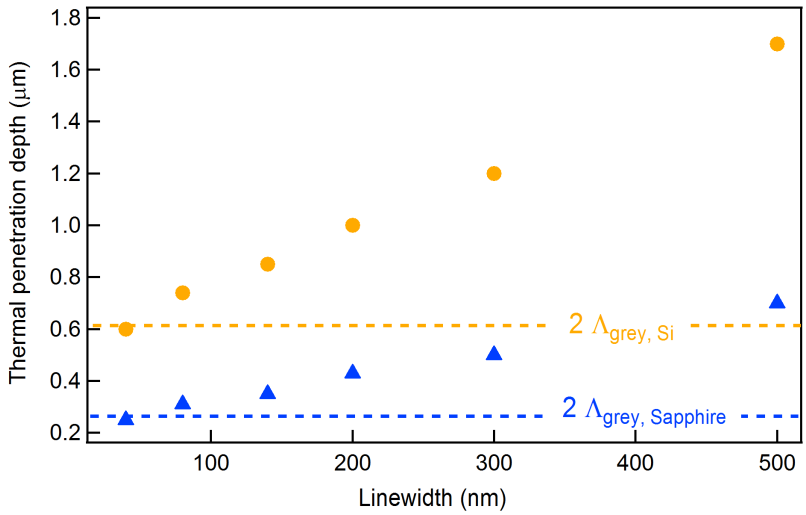

Figure 3.16: **Thermal penetration depth vs. heat source linewidth** | The shorter time scale of thermal decay from small-linewidth structures also implies that heat will not penetrate as deeply into the substrate during the measurement window, as plotted in blue triangles for sapphire and orange circles for silicon. Once the region of effective conductivity change represents a substantial fraction of the thermal penetration depth — as is true for the smaller linewidths represented here if we consider a modified-conductivity layer thickness equal to twice the grey MFP for each material — the decay will only be sensitive to K_{nano} and their thermal penetration depths set a lower bound on d.

theoretical analysis of the 2D results is complicated by the issues discussed above — particularly the question of whether effective resistivity or effective conductivity will offer a more useful parameter space for fitting the thermal decay data. However, some initial comparisons in the raw data are illuminating (see Fig. 3.17).

Greater dimensional confinement and further extension to smaller heat sources may also enable the observation of quantized heat dissipation dynamics [114].

3.6.2 Opportunities with dynamic imaging

Observing the average thermal dynamics of many nanowires or nanodots has already and will continue to reveal important new insight into the fundamental mechanisms of heat transfer at the nanoscale. However, recent significant developments in the application of coherent EUV beams to coherent diffractive imaging (CDI) opens the door to a more detailed look at thermal transport on a localized scale. In particular, 22nm lateral spatial resolution was demonstrated with tabletop HHG sources in 2011 [115], and non-isolated objects were imaged in 2013 [116]. CDI on opaque extended objects in reflection mode was demonstrated with visible wavelengths in 2012 [117] and extended to EUV from HHG in 2014 [118]. These developments in combination with a pump-probe setup for time-resolved measurements will enable the study of nanoscale dynamics with high spatial and temporal resolution.

For nanoscale thermal transport, this could enable direct imaging of dynamics over arbitrarily small distances where more details of the effects of quasi-ballistic transport will be apparent. It will also allow the study of arbitrarily-shaped heat sources where non-uniform laser absorption and heat flow around and from nanoscale features in larger objects may be observed. The localized detail that will be attainable with dynamic CDI will further enhance our understanding of nanoscopic processes like heat transfer.

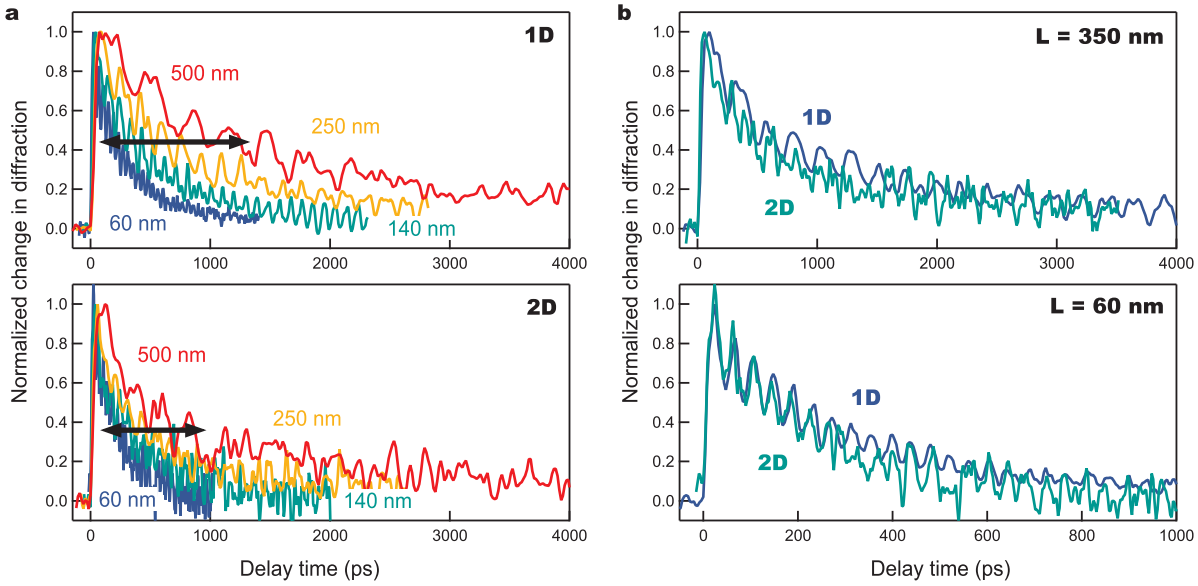

Figure 3.17: **Comparison of 1D and 2D heat transfer | a.** The change in decay time from large linewidth (red) to small (blue) is larger for 1D nanowire heat sources (top) than for 2D nanodots (bottom) on a sapphire substrate. Since we have already seen that the small-nanowire decay is not enough faster than large nanowires to match diffusive predictions, the smaller change across the 2D linewidths suggests even stronger quasi-ballistic effects at play. **b.** A direct comparison of the same large linewidth (350 nm) for 1D (blue) and 2D (green) heat sources (top) suggests a slightly faster initial decay in 2D, which has an extra spatial dimension into which to dissipate heat. Late in the decay, both curves overlap when substrate dynamics become dominant. For a small linewidth (60 nm, bottom), the initial decays look better overlapped, again suggesting there may be stronger ballistic effects working against the additional dissipation direction.

3.6.3 Avenues for further theoretical development

One clear opportunity for further improvements to our theoretical analysis of the thermal transport from nanoscale heat sources is suggested by Wilson and Cahill [90]. They incorporate anisotropic modifications to the effective or apparent conductivities and seek to better resolve the effects of boundary-scattering-induced MFP changes from the effects of MFPs being longer than the relevant thermal-gradient length scales. Such details will become more important moving forward to improve the physical interpretations of the heat dissipation measurements we make.

Currently one of the most significant limitations for the development of a more fundamental picture of micro- and nanoscopic phonon thermal transport is the continued application of diffusive heat flow models to characterize inherently non-diffusive thermal transport. While such effective theories have contributed much to our intuitive understanding of how and when nanoscale dimensions affect heat transfer, more comprehensive and fundamental insight into nanoscale thermal transport may be possible by adopting the framework created to bridge all types of anomalous diffusion [119, 120, 121, 122]. For example, Vermeersch *et al.* [123] point out that Fourier diffusion fails to capture the transition to quasi-ballistic (or super-diffusive) transport at short length and time scales because it assumes normally distributed jumps, as for Brownian motion. They argue the true jump-length distribution is better characterized by a truncated Lévy flight distribution (also used to describe the movements of foraging animals, protein movements along DNA and fluctuations in financial markets), which has a long tail of possible long jump-lengths with a characteristic fall-off in the probability of those long jumps. Thus they fit nanoscale thermal transport data using such a distribution to extract two parameters for a given material: u_{BD} to identify a characteristic length scale of transition from super to normal diffusion and α to characterize how quickly the tail of long-jump probability should fall off [122, 123]. Dhar *et al.* have also demonstrated the efficacy of Lévy flight distributions for characterizing heat transfer in the quasi-ballistic regime [124]. However, a comparison of these descriptions with the idea of phonon participation controlled by the relationship of MFP to important length scales in the system suggests that an even better approach

may be to use the MFP distribution directly to set the probability of different jump sizes. It may be that the truncated Lévy distribution is simply a better fit for real phonon MFP distributions than the distribution assumed by normal diffusion.

A similar two-parameter model has been proposed by Ma to characterize non-Fourier conduction by a diffusive conductivity and a ballistic transport length [125]. However it is addressed specifically to TG experiments and through nanowires of varying length, which both measure transport over particular distances rather than overall nanoscale heat dissipation.

In general, while much work is presently concentrated on improving the fundamental theoretical descriptions of thermal transport at the nanoscale, most models still fail to take into account the presence of multiple heat sources and their possible interactions in determining the overall heat transfer within a full system. Given the fact that most applications of nanoscale heat sources and devices do not fall into the category of isolated objects, exploration of non-isolated nanoscale heat sources will be an important contribution from our future work as our EUV-probe technique remains the only one that is sensitive to heat sources with such small dimensions and spacings.

3.7 Conclusion

Ongoing improvements in nanofabrication capabilities will continue to open access to nanoscale heat sources of smaller size and engineered shape, and enable the systematic study of the new physics that comes to dominate small size scales. Here we extended observations of heat dissipation to the smallest nanostructure heat sources to date and uncovered unexpected transport behavior in which the close spacing of heat sources can increase the efficiency of thermal transport from nanoscale heat sources when both size and spacing are small compared to dominant phonon MFPs. This discovery motivates new possible strategies for thermal management in nanoelectronics, informs design of nanostructured thermoelectric devices and contributes to a more fundamental understanding of phononic heat transfer which will be important for harnessing nanoscale heat sources in any application. Furthermore, as we will see in the next chapter, this new thermal transport regime

enables a new type of MFP spectroscopy for measuring the distributions of phonon contribution to thermal conductivity in materials.

Chapter 4

Probing phonon mean free path spectra

In Chap. 3 we saw how a new regime of nanoscale thermal transport could be described by a phonon suppression filter determined by the heat source size and spacing acting on the spectrum of phonon mean free paths (MFPs) in the material where heat is dissipated. Thus, to be able to predict and control the nature of thermal transport in nanostructured systems, it is clear that knowledge of such spectra of MFP-dependent contributions to thermal conductivity will be required [88]. However, theoretical calculation of these spectra requires significant computational power for all but the simplest crystalline materials, as well as accurate knowledge of the interatomic potentials that control the lattice dynamics, and means of measuring such spectra experimentally only began to be developed in the past 15 years.

Here I show how the new phenomenon of collective diffusion is used to extract the contribution to thermal transport from specific regions of the phonon MFP spectrum, opening up a new approach for thermal transport metrology and MFP spectroscopy. This is because by varying both nanostructure size and separation, an effective phonon filter is introduced that suppresses specific sections of the spectrum of phonon MFP contributions to thermal conductivity. The larger the resistivity correction needed to model the dissipation for a given nano-grating, the stronger the conductivity contribution of phonon modes which were suppressed. We compare our extracted phonon mean free path spectra with predictions from first-principles calculations and find good agreement between experiment and theory. Looking forward, we have a unique new capability for characterizing phonon transport in novel materials where predictions do not yet exist.

4.1 Developments in phonon MFP spectroscopy

The two types of conductivity suppression discussed in Chap 3 Sec. 3.2 — namely increasing the importance of boundary scattering or shortening the thermal length scale — have each been explored for methods of quantitative measurement of phonon MFP spectra. The former was demonstrated by Ju and Goodson in 1999 as they used Joule heating and electrical resistance in aluminum bridges to measure the thermal conductivity of thin silicon films (standard SOI, or silicon-on-insulator, systems) as a function of film thickness to extract an average MFP value of 300 nm [77]. More recently Cuffe *et al.* used transient grating (TG) measurements at large interference fringe spacing ($\approx 21\,\mu m$) on silicon membranes varying in thickness from 15 to 1500 nm to reconstruct a more complete distribution of MFPs [126]. The large thermal grating period ensured that heat flow remained in the diffusive regime, influenced only by the increasing importance of boundary scattering for the thinner membranes. If this effect can be fully accounted for, this can produce a measurement of the bulk material MFP spectrum. However, boundary scattering is a process that inherently involves many variables that are difficult to control, including parameters like surface roughness and oxidation. Therefore these measurements have been distinguished from 'MFP spectroscopy', which seeks instead to measure an unchanging MFP spectrum by monitoring the degree of non-diffusive heat transport observed in a macroscopic material for small thermal transport distances or thermal gradient length scales [65].

Although the idea of using observations of non-diffusive transport to quantify phonon relaxation times was first proposed in 1971 by Simons [127], it was first tied to experimental observations by Koh and Cahill in 2007 [55]. They observed thermal conductivity which depended on the modulation frequency of a laser pump beam heating the surface and attributed it to the suppression of long-MFP conductivity due to the short thermal penetration depth within the time scale set by the inverse of the modulation frequency. This idea was supported by Boltzmann Transport Equation (BTE) simulations in 2011 [62].

Following this development, a number of experiments sought to apply this idea to measure the cumulative contribution to thermal conductivity of phonon modes with MFP shorter than the relevant experimental length scale. Limiting heat source size by adjusting the size of the pump laser focal spot in time-domain thermal reflectance experiments (TDTR) yielded the first proof-of-principle demonstration for studying long-MFP ($> 1\,\mu m$) phonons in silicon [54]. Regner *et al.* [53, 128] and Freedman *et al.* [56] applied frequency-domain thermal reflectance (FDTR), again using thermal penetration depth to limit the thermal transport distance and suppress the contributions of longer-MFP phonons. They reconstructed cumulative conductivity functions down to MFPs of ≈ 200 nm for a number of semiconductor and dielectric materials by assuming the thermal penetration depth serves as a hard cut-off limiting the MFPs which contribute to the observed conductivity. Johnson *et al.* demonstrated that TG measurements with the transport distance limited by the TG period could be used in silicon membranes in a similar way [37]. In particular, they note that such measurements could distinguish the cumulative conductivity of membranes with different thickness since the effect of boundary scattering will have different levels of influence on the intrinsic MFP spectra, while the resonant modes of the full membrane will also affect the phonon dispersion [129].

The influence of heat source geometry, and how an experimental length scale actually acts to modify the contributions of phonon modes with different MFPs to thermal transport, is more complicated than simple cut-offs can account for. Thus geometry-dependent suppression functions, like the one derived in Chap. 3 Sec. 3.4, will be an important part of improving the MFP spectra extracted by these measurements. Suppression functions have been derived for the isolated heat sources of TG experiments [68] and of TDTR and FDTR experiments [89] from grey-approximation solutions of the BTE applied to every MFP. They can also be extracted from Monte Carlo simulations of any given geometry [111]. Once a suppression function for a given experimental geometry is known, Minnich proposed a convex optimization method using the suppression function as the kernel of an integral transform to convert measurements of the cumulative thermal conductivity into cumulative MFP distributions [110]. With this technique he demonstrated that existing TG

measurements using relatively large thermal grating periods (1 µm) could result in MFP spectra extrapolated down to 10 nm. This is due to the very broad suppression function serving as kernel, such that measurements at large length scales can contain information about much smaller MFPs. However, this broad kernel function also implies significant averaging, which will wash out any sharp features in the real MFP distribution, and he emphasizes that where the kernel function is close to zero (as for MFPs below 100 nm in his demonstration), unique solutions for the MFP distribution no longer exist.

It is important to emphasize that the accuracy of any reconstruction of the detailed MFP distribution will be closely tied to the accuracy of the suppression function derived for a given experimental geometry. Wilson and Cahill have recently highlighted some important factors that have thus far been ignored for the construction of these suppression functions, such as the role of changing measurement sensitivity to in-plane vs. cross-plane thermal transport and the intrinsically suppressed conductivity near surfaces due to boundary scattering [90]. Continuing to improve our understanding of the factors which control phonon MFP suppression functions will lead also to improvements in the interpretation of effective conductivity and resistivity measurements and correspondingly improved details in MFP spectra. However we also note that given the current levels of experimental precision, various proposed forms for suppression function approximations cannot yet be meaningfully distinguished in the results.

Some works have also suggested that cumulative MFP distributions may follow universal curves for broad classes of materials. In particular Freedman *et al.* find that a number of crystalline semiconductors, for which resistive scattering is dominated by Umklapp processes, fall along the same normalized cumulative conductivity curve when the MFP cut-off (set by the thermal penetration depth in their FDTR experiments) is scaled by the Umklapp scattering length for each material [56]. Aketo *et al.* suggest these curves may have even more universal characteristics for all crystalline materials with common expressions for estimating the bounds for MFPs contributing between 10 and 90% of the total thermal conductivity [130]. These bounds can be estimated solely from knowledge of the bulk single-crystal thermal conductivity, heat capacity, sound veloci-

ties and Debye temperature. More precision can be obtained through calculation of the harmonic and anharmonic force constants, but reasonable estimates can even be obtained simply from an empirical relationship between the lower 10% bound and upper 90% bound for thermal conductivity contributions.

4.2 Experimental measurement of MFPs down to 14 nm

All the previous work on MFP spectroscopy suffers from two significant limitations: most importantly, the experimental techniques discussed above cannot access MFPs below a few hundred nanometers even though the thermal conductivity of most materials is dominated by phonons with shorter MFPs; moreover, by limiting observations to isolated heat sources, the only direct measurement is of the cumulative conductivity. Our technique takes advantage of the phonon filtering effect of non-isolated heat sources to probe arbitrary segments of the MFP spectrum for any novel material, enabling more direct access to the differential, rather than only the cumulative, MFP distribution. At the same time, combining the use of periodic nanostructures as heat sources with the exceptional phase sensitivity of short-wavelength probes is the only way to experimentally access dimensions far below 100 nm in order to directly resolve the contributions of phonons with MFP down to 14 nm to date [59].

The general principle of this MFP spectroscopy technique is that the degree of non-diffusivity, represented by the magnitude of r_{Corr} for a given heat source size and spacing, is directly related to the integrated MFP range of thermal conductivity contributions that has been suppressed relative to the diffusive prediction. Because linewidth and period set the location and width of the effective notch filter in the phonon MFP spectrum, each nanograting configuration uniquely samples the contribution to thermal conductivity of different MFP ranges of phonon modes with a resolution controlled primarily by the number of configurations tested.

To quantitatively extract information about the differential conductivity spectrum, we use the full multi-MFP form of r_{Corr}, given by:

$$r_{Corr}(L,P) = A\left(\frac{1}{\sum_i k(\Lambda_i)S(L,P,\Lambda_i)} - \frac{1}{K_{bulk}}\right) . \tag{4.1}$$

We partition the full sum in bins between i_{bin}^- and i_{bin}^+ according to the MFP-sensitivity of each grating configuration.

$$r_{Corr}(L,P) = A\left(\frac{1}{\sum_{bins}\left[k_{bin}\sum_{i_{bin}^-}^{i_{bin}^+} S(L,P,\Lambda_i)\right]} - \frac{1}{K_{bulk}}\right) . \tag{4.2}$$

The upper and lower bounds of the full range of MFP contributions to which we are sensitive are set by the suppression functions related to each of our nano-gratings. We choose the minimum (14 nm) and maximum (5 µm) MFPs of our experimental spectrum to include only MFPs that are suppressed by at least 20% in our smallest and largest sample geometries, respectively. As can be seen in Fig. 3.10, each particular configuration for L and P can be related to one most-suppressed MFP at the minimum of S_{total}. We use this information from our set of nano-gratings to establish the MFP bins which we use when fitting r_{eff} data in the full interacting multi-MFP model, as shown in Fig. 4.1: bin boundaries are chosen halfway between neighboring most-suppressed MFPs for every other sample.

Then by fitting our set of r_{eff} data as $r_{eff} = r_{TBR} + r_{Corr}$ we extract the average $k(\Lambda_i) = k_{bin}$ which is associated with all modes Λ_i within each bin, thus assessing the relative contribution per nanometer to the differential thermal conductivity of each region of the phonon MFP spectrum (plotted in Fig. 4.2). The error bars in the histograms are obtained by varying k_{bin} while maintaining the residual of the fit within the range of experimental uncertainty to explore the full range of weights allowed by the shape of the data. By limiting the number of bins to be no more than half the number of data points, we ensure a conservative, well-conditioned fit, although we note that changing the bin number does not substantially alter the trends we observe.

Although the number of experimental data points limits the number of regions we can reasonably consider in this first demonstration, this approach still offers unprecedented new experimen-

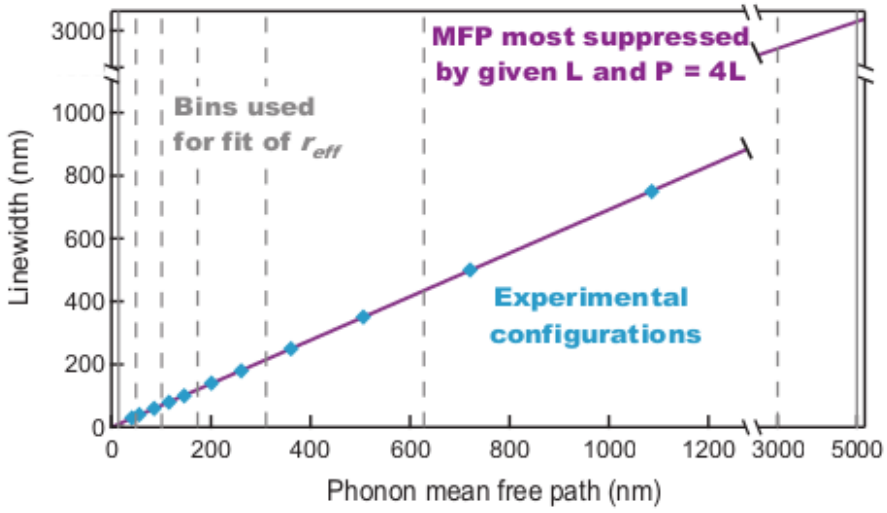

Figure 4.1: **Setting bins to extract MFP spectrum** | In order to fit our r_{eff} data using the full spectrum of phonon MFPs, we bin the spectrum according to the sensitivity of each linewidth-period pair to different regions of the spectrum. The teal diamonds mark the most-suppressed MFP for each linewidth represented in our initial sample set with constant duty cycle at $P = 4L$. The boundaries between bins are set halfway between every other sample point, as shown by the vertical dashed lines.

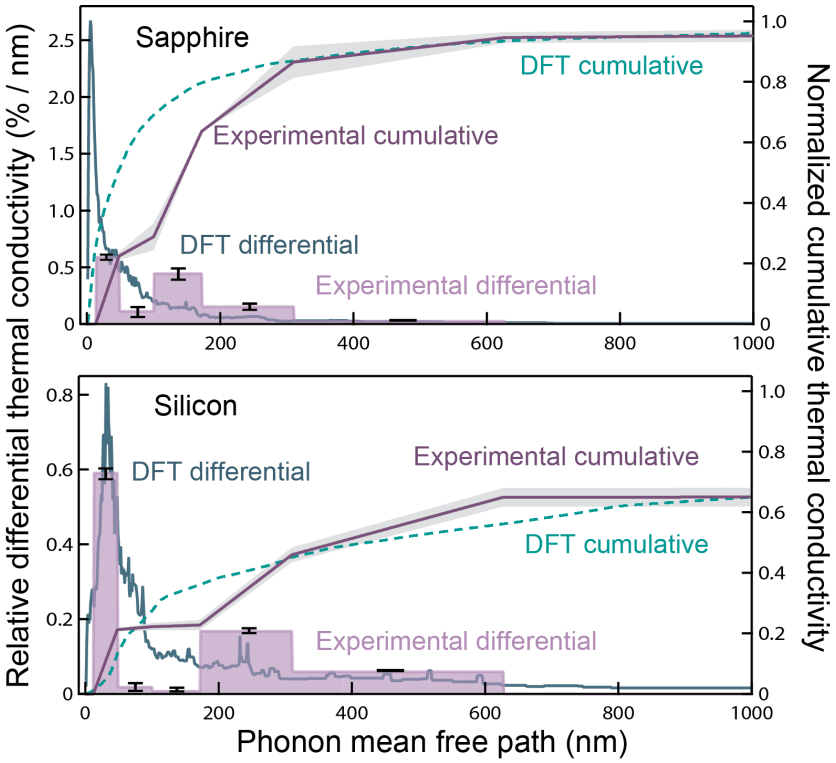

Figure 4.2: **Extracted MFP spectra for sapphire and silicon** | By fitting r_{eff} with multiple bins of phonon modes, the weight k_{bin} assigned to each bin gives the average relative contribution to the differential thermal conductivity (purple shading). Both differential (distributions) and cumulative (lines) conductivities are normalized to the total bulk conductivity. For sapphire (top panel), our data (solid purple line) and first-principles DFT calculations (dashed green line) indicate there are no significant contributions from long-MFP phonons, so the cumulative curves approach unity at 1 µm. For silicon (bottom panel), our data are consistent with large contributions from longer MFPs.

tal access to the differential thermal conductivity contributions of phonons with different MFPs. Furthermore it provides important benchmarks for theoretical predictions, including those from first-principles density functional theory (DFT) calculations shown in Figs. 3.9 and 4.2 calculated according to the methods presented by [57, 59, 61, 131]. In particular, our experimental data across all MFP ranges measured in silicon are in good agreement with our DFT calculations (which also agree with those in the literature [88]). However, some small discrepancies appear for phonon MFPs around ≈ 100 nm, where experimental verification was not possible before. Differences between the experimental and theoretical spectra in this region may also be exaggerated by our limited set of small-linewidth gratings; increased resolution with a larger sample set can address this issue. Our data are also consistent with observations by others which emphasize significant contributions from long-MFP ($> 1\,\mu$m) modes in silicon [53, 54, 37], but the limited number of data points we have for structures much larger than the average phonon MFP results in a relatively large uncertainty in this region. For the purpose of comparison in Fig. 4.2, we normalized the experimental spectra in silicon by assuming the integrated conductivity up to 1 µm should match that calculated by DFT.

For sapphire, both calculation and experimental data imply that phonons with MFPs shorter than 1 µm are responsible for $> 95\%$ of the thermal conductivity. The discrepancy below 300 nm between experimental and theoretical curves (most apparent in the cumulative distribution) is due to two factors. First, the sharper rise in the DFT cumulative curve comes primarily from the very strong short-MFP peak in the conductivity spectrum – a peak that lies at approximately 5 nm, below the lower bound of our experimental sensitivity (14 nm) using 30nm nanostructures. Thus, the experimental data simply does not include the shortest phonon MFP peak. Second, because of the complex crystal structure of sapphire, the DFT calculations required the use of relatively small interaction-distance cut-offs for determining the harmonic and anharmonic force constants, which may cause a larger error in the theoretical predictions than for silicon.

It is important to emphasize that different experimental geometries (for example, 1D- versus 2D-confined heat sources, or bulk materials compared with thin films compared with nanotubes) will result in observed conductivities that are specific to the given geometry. Consequently, effective

thermal conductivity results cannot necessarily be compared in a straightforward manner. However, the phonon MFP spectrum corresponds to a physically real attribute of a material alone and therefore provides the more appropriate tool for comparison across different experimental geometries. Furthermore, the effective thermal conductivity for any experimental geometry can then be predicted using an experimental phonon MFP spectrum combined with the appropriate theoretical model for conductivity suppression. We note that while both heat source geometry and spacing must be included in such suppression functions, spacing effects have only recently been explored, both by our group [132, 58], and more recently by numerical studies with a grey phonon model [113] using the phonon BTE [133].

The ability to experimentally extract a phonon MFP distribution down to such small MFPs offers a new useful method for validating existing first-principles predictions across the whole range of phonon MFPs significant for heat conduction, as well as the first access to such information for more complex materials where calculations have not yet been performed. Furthermore, combined knowledge of both the differential and cumulative thermal conductivity may offer intriguing insight into the full MFP spectrum with the detail necessary for accurate prediction of heat transfer in nanostructured systems.

4.3 Applying MFP spectroscopy with EUV light

Having demonstrated the utility of observing collective diffusion to extract the phonon MFP spectra of materials, we can now begin applying this new tool to the study of more complex materials. As a first step, we study a series of amorphous low-k dielectric SiC:H thin films with varying levels of hydrogenation, which significantly modifies the mechanical, electrical and thermal properties of the films. Some studies have already observed reductions in thermal conductivity of similar materials with increased porosity [134, 135]. Added information about the MFP spectrum and how it is changed with porosity and composition could yield new insight into how to control and optimize the material for the best combination of mechanical, electrical and thermal properties.

Moreover, the amorphous nature of these materials imply that *ab initio* theoretical methods for calculating the MFP spectra will not apply.

We compare how heat dissipation rates change with linewidth and period for nickel nanostructures deposited on this series of thin films (like those shown in Fig. 4.3). A future full analysis following the procedures outlined in this chapter will allow us to extract the contributions to thermal conductivity of a few ranges of MFPs as a function of thin film hydrogenation. One experimental challenge of studying these films is their very low thermal conductivity. This results in the very long decay times visible in Fig. 4.3.

Measurements of this type will also inform the design and optimization for many applications of phonon engineering, either to frustrate phononic thermal transport as for thermo-electrics [44, 43] or to take advantage of as much heat dissipation efficiency as possible as for the transistors in nanoelectronics [48, 49, 50] or bits in magnetic data recording media [51]. In all cases, knowledge of the particular distributions of differential phonon conductivity by MFP will indicate the size scales on which the engineering must take place. For example, mazes [136] and nanomeshes [137] on a size scale of phonon MFPs have been used to slow phonon but not electron transport, and MFP-scale corrugations along the edges of graphene ribbons can be designed to preferentially backscatter phonons [82]. These efforts can be more precisely targeted with knowledge of which phonon MFPs are most dominant in contributing to the overall thermal conductivity.

4.4 Conclusion

The differential phonon MFP contributions to thermal conductivity in materials are fundamental to determining how thermal transport is modified by nanoscale dimensions. They determine the nanostructure sizes and surface roughness levels at which boundary scattering will come to dominate the resistive processes that control thermal conductivity. And they set the length scales at which thermal gradients drive heat transfer that can no longer be approximated by Fourier diffusion, and thus the heat source size and spacing that will see significant deviations from diffusive dissipation behavior. Moreover, the often broad distributions of MFPs must be known in detail to

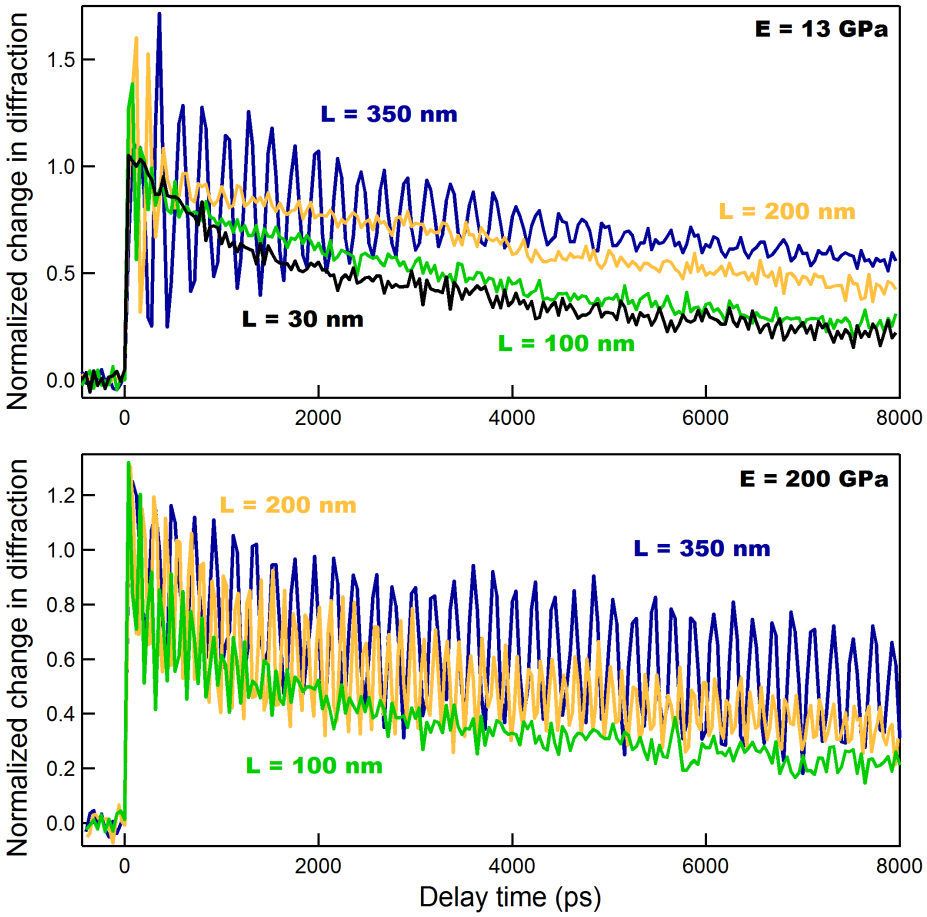

Figure 4.3: **Thin film thermal data for MFP extraction** | Comparing the linewidth-dependent thermal decays for a series of SiC:H thin films – like the two sets shown here for a highly hydrogenated, soft film with Young's modulus $E = 13$ GPa and a stiff film with $E = 200$ GPa – will allow us to study how the MFP spectra may change in correlation with thin film hydrogenation levels. The traces are approximately normalized so that the center of the acoustic oscillations starts at one.

enable accurate prediction of the few-order-of-magnitude ranges in length-scales where transitions in heat transfer behavior will take place and how they will manifest.

Harnessing the phonon-filtering effects of the collectively-diffusive regime of nanoscale thermal transport that we discovered enables a unique new MFP spectroscopy tool. I have demonstrated here that this offers the first experimental access to MFPs as short as 14 nm and the first direct measurements of differential, rather than only cumulative, distributions of thermal conductivity contributions [59]. This technique will be indispensable going forward both as a method for testing theoretical first-principles calculations of MFP spectra and for measuring these spectra in materials where such predictions do not yet exist.

Chapter 5

Thin film metrology

The mechanical properties of materials determine their strength and flexibility, and govern their reliability in the structures and devices they comprise. Tremendous progress in nanofabrication capabilities, particularly in service of increasingly tiny nanoelectronic devices, means that single-atom layers and sub-50nm structures have become commonplace. However, means of characterizing mechanical properties are still severely limited for dimensions below 100 nm [6]. In particular, optimizing the thermal and electronic properties of new materials in manufacturing is often detrimental to the elastic properties that allow reliable processing and fabrication [138]

In this chapter, I give some background about the physical meaning and significance of the elastic properties of materials and then summarize a number of techniques that are used to measure these properties in bulk and film materials. Then, to extend measurement capabilities to sub-100nm ultrathin films, I introduce EUV nanometrology, which makes use of the techniques discussed in Chap. 2, to fully characterize the elastic tensor of isotropic dielectric films as thin as 50 nm, and I demonstrate its applicability to a broad range of material stiffnesses. To improve the precision of our measurements, I also introduce an improved frequency extraction method beyond Fourier transforms to lower our frequency uncertainty by approximately a factor of 10. I then demonstrate the first application of this technique to characterize anisotropic materials before providing an outlook on a number of future opportunities.

5.1 Elastic properties of materials

The elasticity, compressibility, rigidity and hardness of materials are related fundamentally to the interactions between the atoms that comprise them, whether arranged in an ordered crystal lattice or packed together in an amorphous material. The strength of interatomic bonds and the density of atoms will determine how a macroscopic object responds to applied forces. These properties are also directly tied to how robust a material is, how much it can be stretched before failure, how susceptible it may be to cracking, how brittle or flexible it is. Therefore, characterization of elastic properties is important both for using materials in a wide array of applications and to learn about the microstructure of materials.

Displacements of atoms from their equilibrium positions in a crystal lattice will result in restoring forces, just as stretching or compressing a spring by a distance x from equilibrium results in a restoring force F characterized in the linear regime by Hooke's law, $F = -kx$. In the simple case of a spring, k is the elastic constant related to the particular spring. In an atomic lattice (or continuum material), an analogous law applies, but because the atoms can be displaced in any combination of the three dimensions, the full strain (or displacement) field and resulting stress (restoring force) of an object are characterized by 3×3 matrices, and the 'spring constant' relating them is a $3 \times 3 \times 3 \times 3$ tensor [93]. Symmetry reduces the number of independent components of this elastic tensor $\mathbf{c}$ to 21, and the symmetry of specific crystal lattice structures can reduce it even further. Then, just as k sets the resonant frequencies of spring oscillations or the speed of traveling waves, $\mathbf{c}$ will offer the same information for acoustic waves in materials specific to each direction of propagation and to wave type (longitudinal and transverse).

The elastic tensor $\mathbf{c}$ relates the microscopic displacements of atoms to the behavior of a material as whole, but its specific attention to directions of stress and strain means that relatively simple macroscopic processes require several components to fully encapsulate the material response. For example, linear compression along the axis of a rod combines compressive stress along the axis with resulting additional stress perpendicular to the applied force. Thus macroscopic elastic

responses are often related instead to elastic moduli, which are generally combinations of multiple components of **c**. Specifically, Young's modulus and Poisson's ratio are enough to completely characterize isotropic materials.

The Young's modulus E characterizes the stiffness (or rigidity) of a material, quantifying how far a material will deform along the direction of an applied force. Poisson's ratio ν records how much a material will expand (or sometimes contract) in one direction while it is compressed in the perpendicular direction. As shown in Fig. 5.1, E can vary over several orders of magnitude from MPa ($= 10^6$ N/m^2) to TPa, while ν is more narrowly confined between -1 and 0.5 for stable materials, making it an intriguing parameter for more universal characterization of materials from the softest solids to the strongest liquids [140]. Indeed, by quantifying the balance between a material's resistance to volume change and its resistance to shape change, ν is a quantity that can be used to indicate the structural performance of any material and has been shown to directly correlate with critical features like damage tolerance in metallic glasses [141].

5.2 Existing metrology techniques

While a number of techniques are available for characterizing the elastic and mechanical properties of thin films, challenges mount as film thickness shrinks.

Nanoindentation is a widely-used technique that follows the displacement of a specially-designed tip, called an indenter, into the surface of a material as precise loading forces are applied. This direct measurement of the stiffness and hardness of a material is used to extract the stress-strain relationship and various elastic moduli. These relations require careful modeling of the contact area between the indenter and the indented surface, and once the material layer is thin, further modeling must account for the influence of the substrate [142, 143, 144]. Accurate measurements still require relatively thick films (hundreds of nanometers) or reliable knowledge of some material parameters in the system, such as values for the Poisson's ratio of both substrate and film. Characterization of multilayers only yields average values. It is advantageous for local measurements across a film surface as its sensitivity is confined to the region directly compressed by the

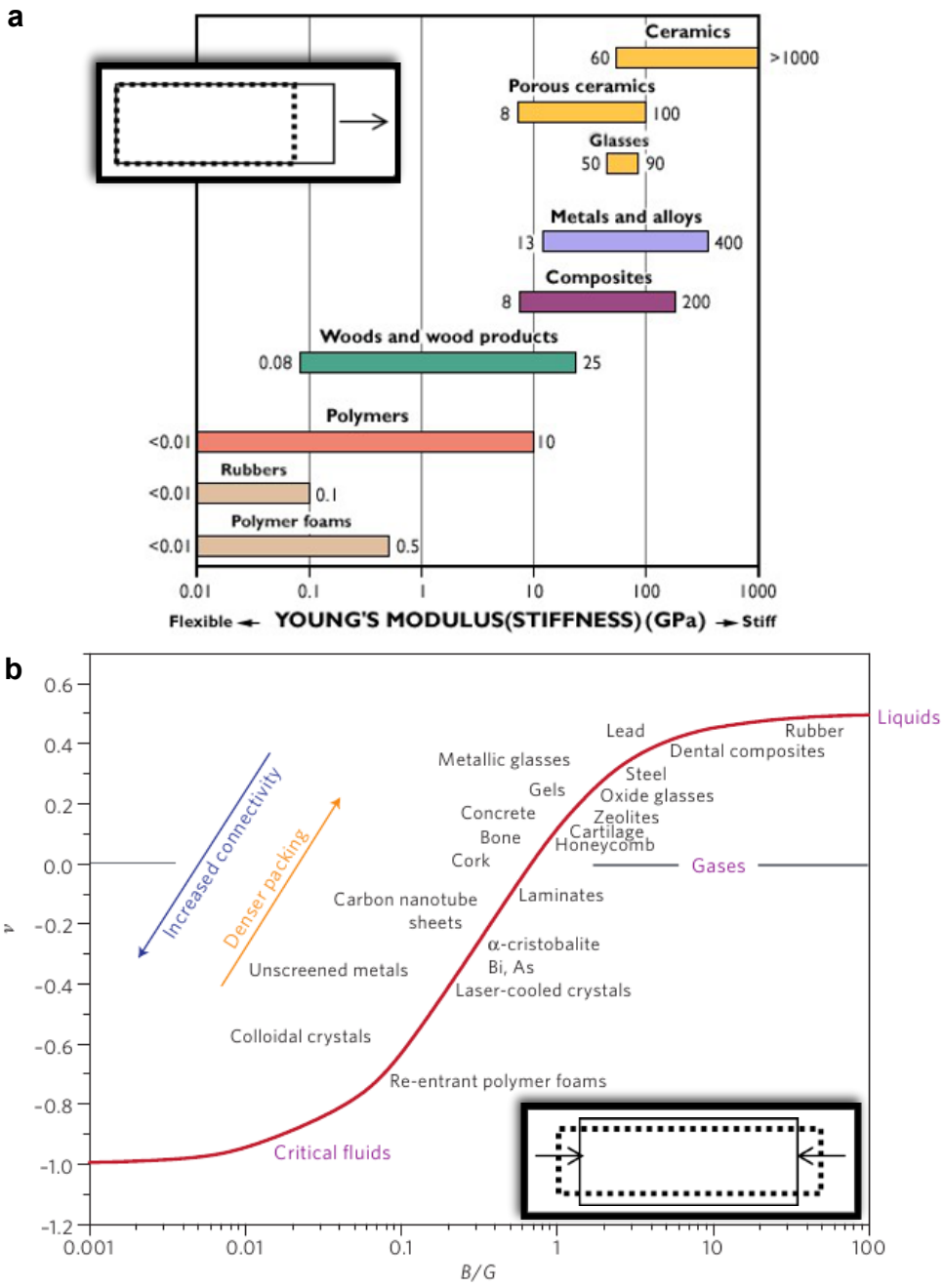

Figure 5.1: **Range of E and ν for materials | a.** Young's modulus can vary by orders of magnitude, describing the stiffness or resistance to deformation of materials (graph from [139]). **b.** Poisson's ratio ν is more limited, unifying all stable materials along a spectrum extending from -1 to 0.5 and quantifies the balance between a material's resistance to volume change and resistance to deformation. $\nu = 0.5$ implies a perfectly incompressible material which spreads out to the side as much as it is compressed in the other direction. Negative values describe materials which shrink perpendicular to an applied compression (graph from [140]) The two insets offer a schematic illustration of the forces and strains related by the two parameters.

nanoindenter. However, it is also a destructive measurement and has contact areas that are too large to apply to small structures.

A newer atomic force microscopy-based (AFM-based) technique relies instead on the mechanical resonances of the AFM cantilever, which shift when the tip is moved into contact with a material surface. This contact-resonance AFM technique involves much smaller contact regions because of the much smaller forces involved — especially for high-order resonant modes of the cantilever [145] — and is therefore less destructive to sample surfaces. Without shear components in the surface motion, this technique is only sensitive to the Young's modulus, leaving the Poisson's ratio to be assumed [146], and can still be influenced by substrate properties for films below 1 µm [147], with the onset of substrate effects depending on the properties of the AFM tip and sample [148]. Moreover, it requires strong models of the cantilever eigenmodes for quantitative measurements of the material properties [146] or comparison with precisely known reference samples [147]. However, properties of films as thin as 7 nm have been extracted from CR-AFM measurements when the substrate was characterized separately [149]. It further offers a very sensitive tool for mapping local variations in elastic parameters across a surface when the differences, rather than the absolute values, are of interest.

Non-contact thin film metrology typically relies on the interactions between light and acoustic waves or phonons in the material of study. Brillouin light scattering (BLS), for example, makes use of direct interactions between light and the acoustic phonon modes of a material. A photon that scatters with a phonon loses or gains the phonon energy and shifts slightly in frequency, yielding a spectrum of scattered light that can identify many phonon modes [150]. Because of the access to both transverse and longitudinal acoustic velocities, BLS does allow measurement of both Young's modulus and Poisson's ratio. However, interpretation is more complex: the weak intensity of scattered light and the difficulty of proper identification of phonon modes make the film characterization strongly dependent on the experimental accuracy attained, and strong understanding of both the scattering cross-sections of different modes and the response of the measurement system are required [151]. Moreover, though scattering from bulk acoustic modes tends to be stronger

than from surface modes and more separated from the bright elastically scattered spectral peak, they can only be observed for materials transparent to the probe light [150]. But given the right conditions, measurements with BLS can have very high precision [152] and have been demonstrated on films (free-standing) as thin as 8 nm [153].

The other major class of optical non-contact techniques falls under the title of picosecond ultrasonics or photoacoustics. Traditionally this has made use of the longitudinal acoustic wave (LAW) velocity to calculate the Young's modulus of an isotropic thin film by assuming a value of Poisson's ratio. Strong absorption of a laser pump pulse in the thin film or in an additional thin metal transducer layer launches these LAWs, which are observed by transient changes in the reflected intensity of a subsequent probe pulse [154, 155]. When the films are transparent to the probe and thicker than a few acoustic wavelengths, a traveling acoustic pulse can also cause oscillation in the interference between light reflected from the surface and light reflecting off the moving acoustic pulse, allowing a measurement of the acoustic velocity without knowledge of film thickness [156]. Because the probe signal does not require high spatial resolution to detect LAW signals in reflectivity across a large area, these techniques have been used to study films down to a few nanometers in thickness with visible-wavelength light [156]. The dispersion of broadband surface acoustic waves (SAWs) has also been used to evaluate the Young's modulus of a film as thin as 5 nm [157].

Nanostructured transducers were introduced to these measurements more recently as a way to simultaneously excite SAWs and LAWs [158, 159, 160, 161]. By accessing both the longitudinal and transverse acoustic velocities, this alleviates the need to assume a value for Poisson's ratio, but the continued use of visible-wavelength probe light inherently limits the sensitivity of this technique. Thinner films require shorter-wavelength surface displacements – smaller than those easily observable by the resolution available with visible light. Thus far, visible-light picosecond ultrasonics with nanostructured transducers has been used to characterize films as thin as 260 nm [158]. Narrowband SAWs can also be excited by interfering two pump laser beams on an absorbing surface to create a transient grating without the need for absorbing nanostructures and excite

SAWs with wavelength equal to that of the interference period [162, 163, 164]. This allows an all-optical method for capturing both SAWs and LAWs on any absorbing surface, but visible pump wavelengths limit the accessible transient grating periods to a minimum of $\approx$ 750 nm.

Two more developments have extended the capabilities of visible-probe photoacoustics. High-speed asynchronous optical sampling (ASOPS) uses two femtosecond lasers with slightly different repetition rates to set up a train of pump and probe pulses which scan the delay time without any need for a mechanical delay stage. This fact combined with the high repetition rates (hundreds of MHz) of the lasers enables very low noise levels, and signals at the 10^{-7} level are visible even after only one second of acquisition time [165]. Thus, even though visible probes are significantly less sensitive to the surface displacements of nanostructures than EUV probes, techniques like this improve signal detection compared to standard visible-light techniques and allow very small signals to be resolved. Devos *et al.* also demonstrated a new technique interfering two probe beams where one reflects from the sample before a pump pulse arrives and one at variable delay after. In this way, they gain sensitivity to the out-of-plane oscillations of nanostructures smaller than the diffraction limit of visible light [166]. These two clever techniques demonstrate how the applications of visible-probe photoacoustics can be extended further than previously thought possible. An exciting idea to contemplate is how similar techniques could be adapted for EUV wavelengths, potentially extending capabilities far beyond the resolution improvements intrinsic to short-wavelength probes.

5.3 EUV nanometrology

To enable full elastic characterization of ultrathin films we make use of nanostructured metallic transducers with periods as short as 90 nm to simultaneously excite LAWs and very short-wavelength SAWs in a series of 50-100nm thin films of varying elastic properties – the thinnest films directly probed to date using photoacoustic probes to extract both Young's modulus and Poisson's ratio. The shortest SAW wavelength implies a small penetration depth fully confined within the thin film of interest, as shown schematically in Figure 5.2. This allows us to selectively probe the properties of the thin film material without unwanted contribution from the substrate un-

derneath. Given the shortest achievable SAW wavelengths from nanostructured transducers within the present capabilities of nanofabrication, this approach to mechanical nano-characterization will scale to sub-10nm thin films [41]. Such capabilities are particularly important as a number of theoretical studies suggest thickness dependence in the elastic properties of thin film materials [167, 168], and experiments are needed to directly test theoretical models of these systems. At the same time, our technique enables the testing of new ultrathin film materials being developed in nanoelectronics, as well as a potential in-line characterization tool for process control.

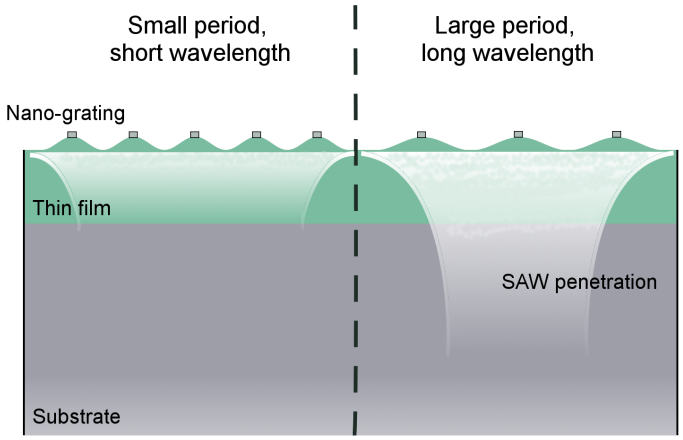

Figure 5.2: **Setting SAW penetration depth** | The propagation of surface acoustic waves is limited to a penetration depth equal to a fraction of their wavelength. Thus, by setting a short SAW wavelength with a suitably small-period nano-grating, the penetration and sensitivity of the SAW measurement can be confined to thin film layers at the surface of a sample, while long-wavelength SAWs from large-period gratings probe the properties of the substrate material.

In these experiments we probe a series of 50-100nm low-k dielectric SiC:H thin films (*i.e.* with low dielectric constant k) deposited on silicon substrates representing a range of elastic properties set by the levels of hydrogenation in the film material – in particular with Young's moduli nominally varying from 13 to 200 GPa [169]. Using electron-beam lithography and lift-off techniques, we deposit a series of periodic metallic nanostructures on the surface of each film to serve as transducers of nanoscale acoustic waves in the system. A schematic of the samples and the acoustic waves that will characterize the films is shown in Figure 5.3. Nickel is chosen as an efficient transducer material

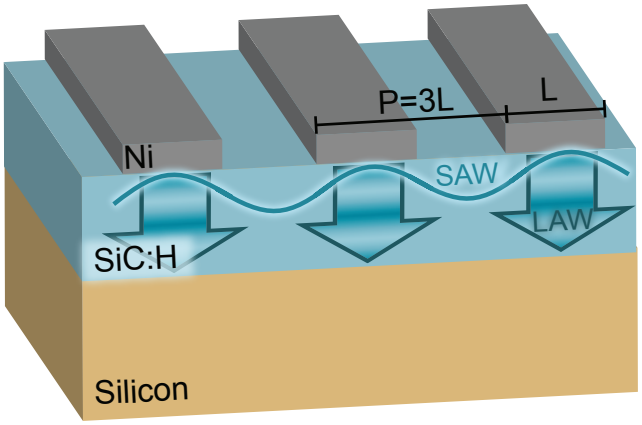

Figure 5.3: **Samples for EUV photoacoustic metrology of thin films** | Our samples consist of 1D nickel nano-gratings deposited on the surface of 50-100nm SiC:H low-k dielectric thin films on silicon substrates. An infrared pump pulse is absorbed by the nickel, and the subsequent impulsive thermal expansion launches acoustic waves in the system. The SAW and LAW within the film isolate the material properties of the film from those of the rest of the system. The SAW wavelength is set by the grating period P. LAW pulses launched downward reflect back to the surface from the buried interface with the substrate.

for its strong absorption of our 800-nm pump light and high coefficient of thermal expansion (at 12.77×10^{-6} K^{-1}).

As discussed in Chap. 2, an infrared pump pulse causes an impulsive thermal expansion of the nanostructures which launches the acoustic waves: LAWs traveling downward through the thin film as in traditional photoacoustics; and SAWs excited due to the transverse periodicity of the stress induced at the film surface. The SAW wavelength Λ is governed simply by the period of the nanostructures, which allows the excitation of shorter wavelengths than accessible by current transient grating techniques [35, 41].

For each of our thin film samples, we make use of a range of periods P from 90 to 1500 nm with constant filling fraction of 1/3 and constant nanostructure height of 10 nm. With the SAW penetration depth $\zeta \approx \Lambda/\pi$ (as observed in a number of simulations), full confinement inside a film of thickness t is achieved when $P \leq 3t$. Therefore, this range of periods can excite waves ranging from those fully confined within even our thinnest 50nm film to waves propagating primarily in the silicon substrate, allowing us to demonstrate unequivocally the layer-selective measurement of both film and substrate elastic properties. We achieve detection of the shortest-wavelength SAWs for full confinement by harnessing the similarly short-wavelength probe light we have from HHG.

5.3.1 Extracting acoustic velocities

The dynamic signals revealing the SAW oscillations and LAW propagation in thin films are directly used to extract the velocities of both types of acoustic waves. The longitudinal pulse echoes visible in Fig. 5.4 give the time required for a round-trip through the film layer of thickness t. We confirm this delay time τ_{LAW} by looking for these echoes in signals from all the available grating periods. As shown in Fig. 5.4, the echoes return to the surface at the same time regardless of grating period since all have traversed the same thin film layer. The velocity is then calculated from $v_{LAW} = 2t/\tau_{LAW}$. Note that the film thickness must be known independently; in this case we rely on accurate ellipsometry measurements of the thicknesses of each film. While we currently estimate the echo round-trip time as shown by the dashed lines in Fig. 5.4, more precision could likely be

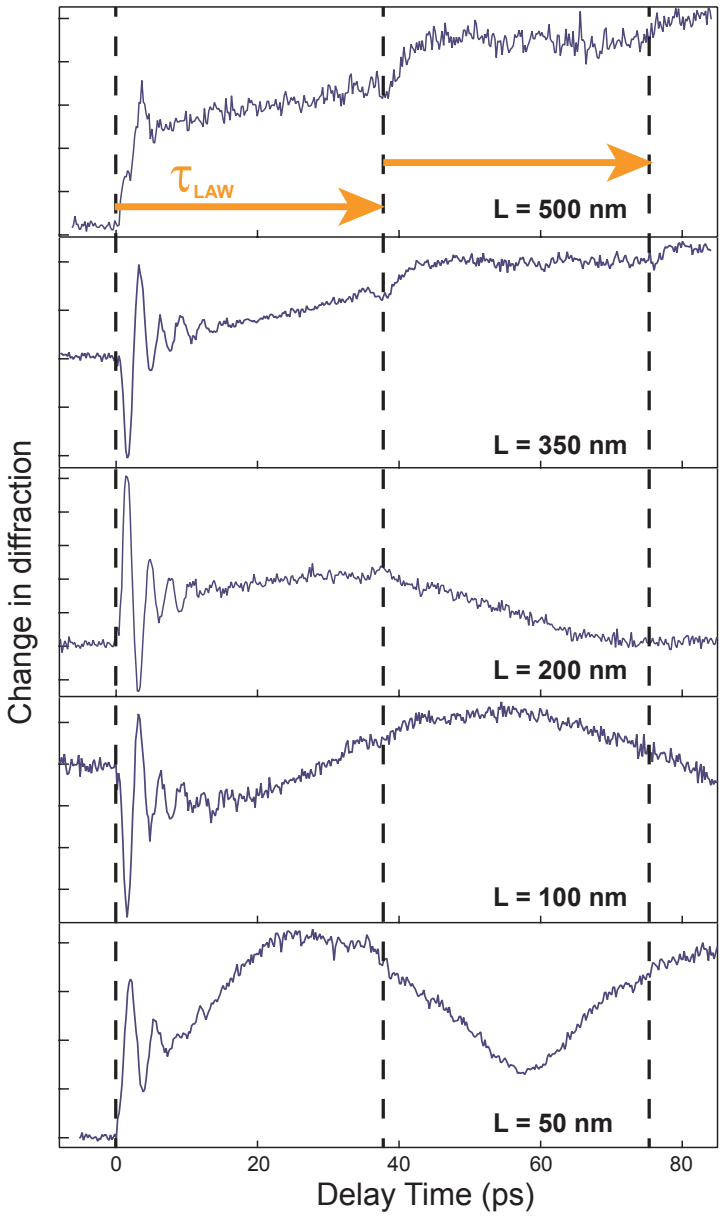

Figure 5.4: **LAW echoes in a set of grating periods** | The signatures of LAW pulse echoes returning to the surface arrive at the same time delay τ_{LAW} regardless of grating period because all have traveled across the same thin film layer. The high-frequency oscillations early in the signal correspond to the resonant LAW mode of the nanostructures.

obtained through a more thorough understanding and model of the shape of the echo signal. Such a model could be fit to the measured data to extract the precise delay time corresponding to the point in the signal that would yield the exact longitudinal velocity.

For the SAWs, we know their wavelength Λ from the period of the nano-grating that excites them (and its higher harmonics) [33]. Then by extracting the oscillation frequencies f we observe, the velocities can be calculated, $v_{SAW} = \Lambda \cdot f$. To isolate the f with high precision we employ a chirp z-transform (CZT) [170]. Unlike the discrete Fourier transform, the CZT allows an arbitrary number of frequency samples (up to the number of time samples) to be concentrated within a specified frequency range. This makes it well-suited for attaining high frequency resolution over a small bandwidth. We then fit the peak to a Gaussian function to extract the central frequency, as shown in Fig. 5.5, and average the peak values from many scans on the same sample. The standard deviations of these measurements generally represent a factor of 10 improvement in uncertainty compared to the standard deviation of Fourier transform peaks among the same set of measurements.

Figure 5.6 shows that for large-period gratings, the measured SAW velocity is consistent with literature values for bulk silicon ($\approx$ 5000 m/s [171]) because the wave penetrates so far below the surface that it travels mostly in the substrate. In contrast, the short-period gratings display the slower velocities associated with all the different film materials because these waves are truly confined within the film layer, isolating the film properties from any substrate influence. Even different SAW orders launched by the same nano-grating can illustrate this effect; in particular, the $P = 600$nm grating excites a fundamental wave which mostly represents the substrate properties and a second-order wave with wavelength $\Lambda = 300$ nm which is much more confined in and representative of the thin film material.

5.3.2 Elastic properties from acoustic velocities

For isotropic materials, measurements of the longitudinal and transverse acoustic velocities are enough to characterize the full elastic tensor $\mathbf{c}$, which has only two independent components in

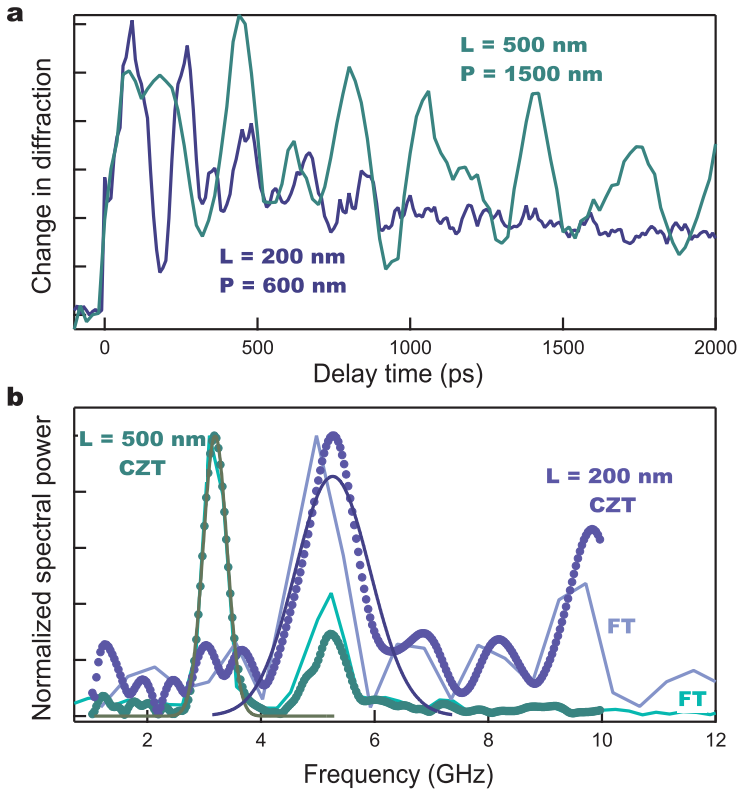

Figure 5.5: **Extracting SAW frequency from thin film signals | a.** Different nanowire linewidths, associated with different periods at a constant relationship of $P = 3L$, excite particular SAW wavelengths which appear at distinct frequencies in the diffraction signal. **b.** Fourier transforms (as shown by the light green and blue curves) identify the same frequency peaks as the chirp z-transform (marked in circles) but with lower resolution that can miss the actual peak locations by amounts smaller than the FT step size. Fitting Gaussian curves to the CZT peaks (solid curves across the data points in the first-order peaks) then extracts the central values.

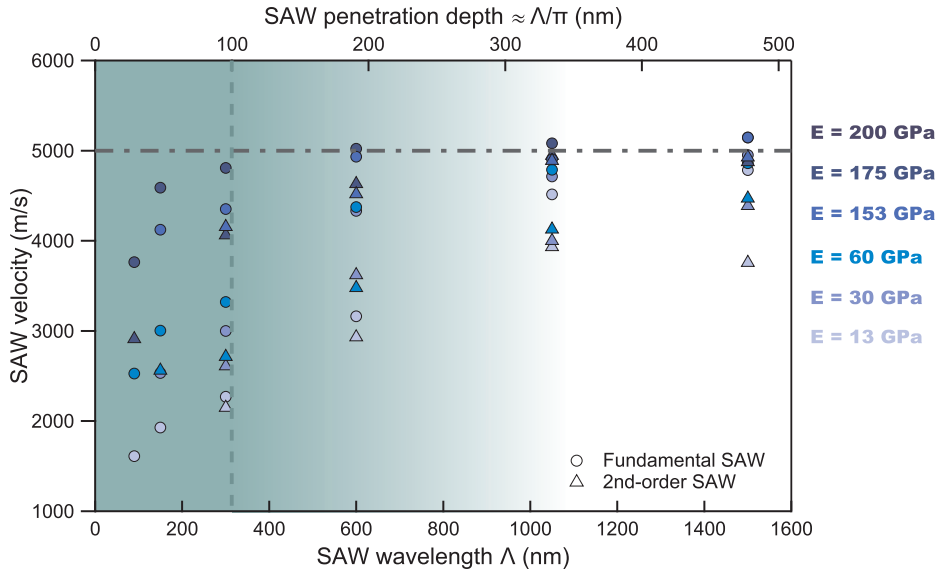

Figure 5.6: **Layer sensitivity in the SAW velocity** | While for long wavelengths and penetration depths all of the 100nm film samples display SAW velocities consistent with that of the silicon substrate, the short-wavelength, small penetration depth measurements clearly separate the different films with their slower velocities. The green dashed line represents the point at which the SAW penetration depth is approximately equal to the film thickness; green shading implies that the effect of the film is still important even for the intermediate wavelengths. In some intermediate cases – particularly $\Lambda = 600$ nm – it is apparent that the fundamental SAW (circles) is consistent with propagation mostly in the silicon substrate while the second harmonic excited by the same grating (triangles) is consistent with a slower thin film velocity.

this case [93]. Specifically $\mathbf{c} = (c_{11}, c_{44})$ where

$$c_{11} = \rho v_{LAW}^2 \tag{5.1}$$

$$c_{44} = \rho v_{TAW}^2. \tag{5.2}$$

Here the density ρ must be known independently, as from x-ray reflectivity measurements in this case, and the transverse velocity v_{TAW} is related to $v_{SAW} = v_{TAW}\sigma$ where σ is the Landau factor, which is generally > 0.9 [172]. These elastic constants can then be related to the Young's modulus E and Poisson's ratio ν, which are more typical quantities for describing the macroscopic responses of materials.

$$E = c_{44}\left(\frac{3c_{11} - 4c_{44}}{c_{11} - c_{44}}\right) \tag{5.3}$$

$$\nu = \frac{c_{11} - 2c_{44}}{2(c_{11} - c_{44})} \tag{5.4}$$

Of course, the presence of the nanostructures does introduce loading on the film, which will modify the measured SAW velocities from the case of a free surface. In particular, the SAW modes at a free surface are eigenmodes of the system and do not radiate energy into the bulk material or decay in an ideal system [173]. In contrast, the stress at the interface between film surface and nanostructures that allows the structures to move with the surface also serves to scatter energy into the bulk [173]. Put another way, the pure SAW modes are no longer eigenmodes of the nanostructure/film/substrate system; instead the nanostructures serve to couple the pure SAW modes to the bulk modes of the film/substrate, leading to the radiation of energy away from the surface [161].

To understand and account for the effect of the nanostructures on our measurement of the thin film properties, we employ finite-element simulation to model the whole system. As in the simulations of thermal dynamics in our samples (described in Chap. 3 Sec. 3.3.2), the laser excitation of the nickel nanostructures is modeled according to Eqn. 3.6. Following Nardi *et al.* [92], the displacements $\mathbf{u}_{max}(\vec{r})$ at each point $\vec{r}$ at the time of maximal deformation are projected onto the set of eigenmodes $\mathbf{u}_i(\vec{r})$ of the nanostructure-film-substrate system, calculated by solving

the acoustic eigenvalue problem,

$$\vec{\nabla} \cdot [\mathbf{c}(\vec{r}) : \vec{\nabla}\tilde{\mathbf{u}}_i(\vec{r})] = -\rho(\vec{r})\omega_i^2\tilde{\mathbf{u}}_i(\vec{r}) \tag{5.5}$$

and normalizing over the unit cell

$$\mathbf{u}_i = \sqrt{\frac{M_c}{C\int_{V_c}\rho\tilde{\mathbf{u}}_i^2 dV}}\tilde{\mathbf{u}}_i \tag{5.6}$$

where M_c and V_c are the mass and volume of the unit cell, respectively and C is a unity constant with units [m^{-2}]. The projection

$$|\mathbf{u}_{max}\rangle = \sum_i \langle \mathbf{u}_i|\mathbf{u}_{max}\rangle|\mathbf{u}_i\rangle = \sum_i c_i|\mathbf{u}_i\rangle \tag{5.7}$$

reveals the degree to which each eigenmode contributes to the impulsively excited displacement, and thus how strongly each eigenmode will be excited by the impulsive expansion. This technique unambiguously resolves which eigenmodes are excited, revealing that the main contributions to the sample dynamics are a symmetric SAW and its higher harmonics, as shown in Fig. 5.7, and we can directly determine their frequencies. By then adjusting the Young's modulus and Poisson's ratio of the simulated thin film material and seeking to match the predicted frequencies to those we observe for the whole set of grating periods, we can more accurately extract the properties of the film alone, having accounted for the influence of the grating structures. In practice this is often most readily accomplished by using the large-period sample acoustics to confirm the elastic properties for the simulated substrate and then tuning the film properties to match the shortest-period samples. Finally, one set of elastic parameters for the whole system is found to match the observations from all sample periods. This procedure results in the Young's modulus and Poisson's ratio for each SiC:H thin film sample, reported in Fig. 5.8.

In comparing our measurement of the Young's moduli to the nominal values obtained via nanoindentation on thicker samples of the same film materials, the measurements falling along the line with slope one indicates close agreement. However, it is interesting to note that for one sample (E_{nom} = 153 GPa), the initial nanoindentation value was much higher than what we observed.

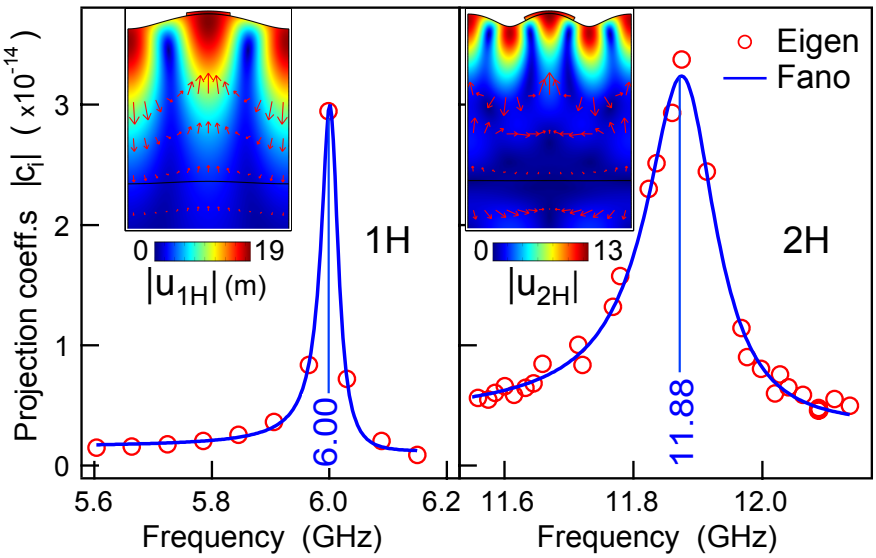

Figure 5.7: **Identifying excited SAW modes with simulation** | The initial thermal expansion displacement of the nanostructured system is projected onto the set of acoustic eigenmodes to determine which are most strongly excited by the impulsive pump excitation. Thus peaks in the projection coefficient $|c_i|$ can identify the mode frequencies that will be excited in the experiment. Here the peaks are fit to Fano profiles to extract the central frequencies and lifetimes. The two insets show the absolute total displacement fields related to each excited eigenmode — the fundamental and second harmonic are shown here. Figure adapted from [92].

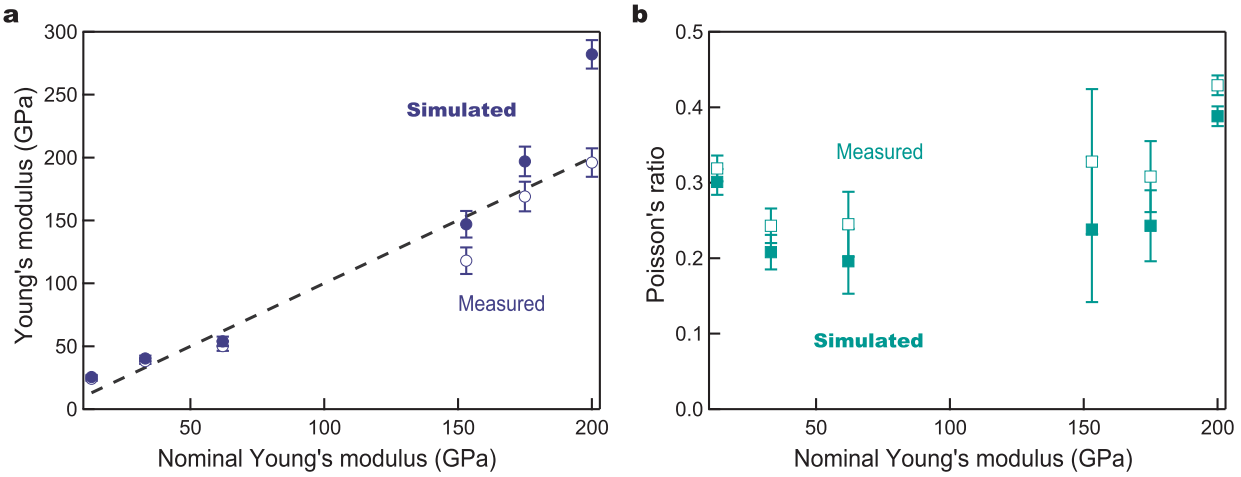

Figure 5.8: **Elastic characterization of thin film series** | From the measurements of SAW and LAW velocities in a series of SiC:H thin films with different degrees of hydrogenation, we demonstrate the capability of EUV nanometrology to extract both Young's modulus and Poisson's ratio across the whole range of nominal Young's moduli (characterized by nanoindentation on thicker samples of the same film material). **a.** The measurements of Young's modulus mostly match those indicated by the nanoindentation values (dashed line). Also note that accounting for the effect of the nanostructures with simulation (solid symbols) generally results in a larger E than simply calculated from the measured velocities (open symbols). **b.** Our nanometrology measurements were the first to address Poisson's ratio for these types of film materials. Again the simulations typically shift the results compared to those calculated directly from the measured acoustic velocities, to lower values in this case. Note that the sample with $E_{nom} = 200$ GPa is the only film with thickness 50 nm, and its particularly high Poisson's ratio may be anomalous for that reason. For the rest of the films, which all have thickness 100 nm, Poisson's ratio is mostly constant until an upward trend begins toward the soft end where the high levels of hydrogenation may push bond coordination past a critical point [138]. The large error bar for $E_{nom} = 153$ GPa is due primarily to the similarity between the film and silicon substrate which decreases the reflected amplitude of the LAW pulse.

A subsequent re-measurement of that film with nanoindentation matched our result much more closely.

Since we excite both transverse and longitudinal waves simultaneously, we are also able to measure the Poisson's ratio. And in fact, our measurements represent the first characterization of Poisson's ratio for these films. While the values appear mostly constant across this range of film stiffnesses (except for the only 50nm film at $E_{nom} = 200$ GPa where the isotropic assumption may begin to break down), we do note that the lowest-E_{nom} films may suggest the beginning of an upward trend in ν. This may be due to the crossing of a critical value in the bond coordination in these highly-hydrogenated films [138]. The future study of even softer, more highly hydrogenated films will allow further probing of this trend.

While our analysis thus far has only utilized the fundamental SAWs observed, similar fitting techniques that incorporate information from the higher SAW harmonics as well could likely improve the overall precision in the future.

5.4 Anisotropic materials

Launching SAWs with 2D arrays of nanodots increases the number of harmonics we observe. For example, it adds one in between the fundamental f_0 and second-order $2f_0$ frequencies of the 1D nanowire arrays. With frequency equal to $\sqrt{2}f_0$, it corresponds to the diagonal periodicity represented in Fig. 5.9. For a nanodot array aligned along the [110] direction of single-crystal silicon, the fundamental SAW and higher integer orders lie along the [110] direction while the diagonal orders are along [100]. Therefore, for an anisotropic crystal like silicon, the different modes could, in principle, be expected to display different velocities [174].

I examine the SAW frequencies observed from 1D and 2D arrays of nickel structures with linewidths L from 30-750 nm and periods $P = 4L$ on silicon to test this idea. Fig. 5.10 plots the observed frequencies vs. $k/2\pi = 1/\Lambda$ for all the observed harmonics. For both 1D and 2D arrays, all harmonics appear to follow the same-slope line for the long-wavelength (small-k) samples where the influence of the gratings does not significantly affect the dispersion relation, implying they all

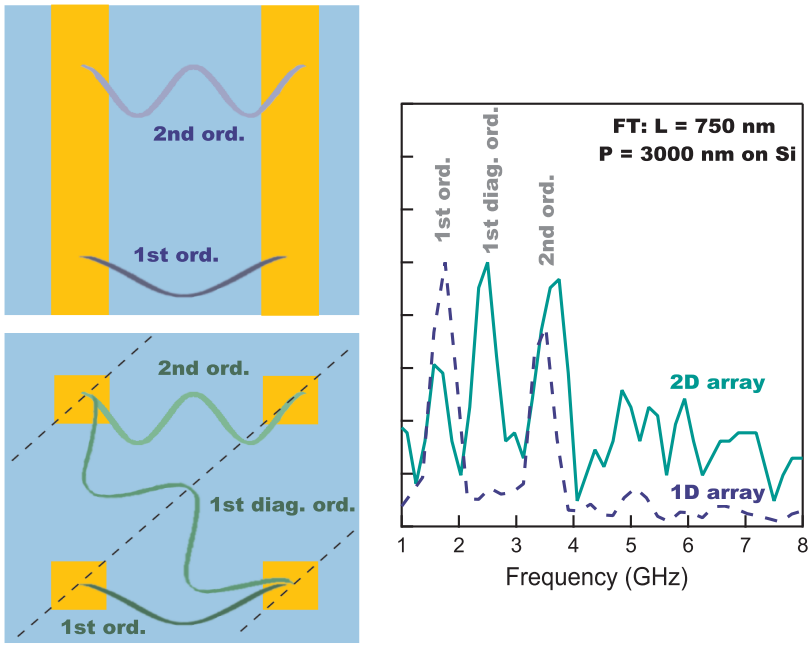

Figure 5.9: **Extra SAW modes from 2D nanodot arrays** | All of the SAW harmonics launched by 1D nanowire arrays cross the surface in the same direction. 2D nanodot arrays, on the other hand, add periodicity in the diagonal direction. As visible in the Fourier transform of signals from 1D (dashed blue) and 2D (solid green) gratings with linewidth $L = 750$ nm and $P = 3000$ nm on silicon, this additional periodicity adds frequency peaks in between the integer orders launched by 1D gratings. The first diagonal order showing here is $\sqrt{2}$ times the fundamental frequency.

propagate with the same velocity. While this is expected for the 1D arrays, for the 2D arrays this suggests that we do not detect any anisotropy comparing the integer harmonics with the diagonal orders.

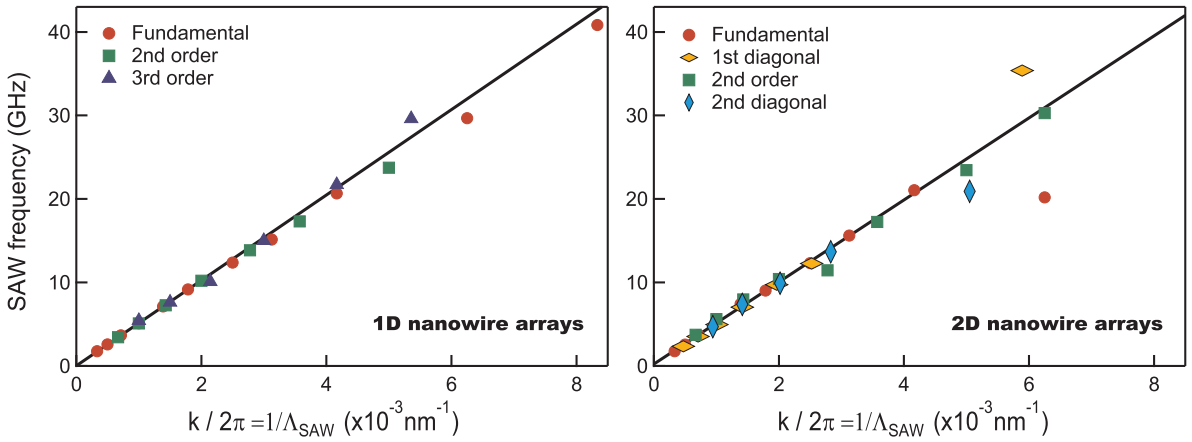

Figure 5.10: **Examining 1D and 2D SAWs to characterize anisotropy** | The long-wavelength (small k) SAWs follow a linear dispersion (black lines) where the slope gives the bare-substrate SAW velocity. If the diagonal orders (diamond symbols) launched by 2D nanodot arrays have speed determined by the [100] rather than [110] axis of silicon, they should lie along a distinct line from the integer orders (circles, squares and triangles). However, no difference is apparent in these plots.

For quantitative comparison, linear fits to the long-wavelength data of each harmonic yields the SAW velocity associated with each. Fig. 5.11 shows that integer harmonics compare well from 1D to 2D arrays, but the diagonal orders match in velocity within error bars. However, the anisotropy in silicon is not particularly large and the expected difference in velocity is only from about 5100 m/s along [110] to 4925 m/s along [100] [171]. If I compare the 1D measurement of the fundamental wave velocity ($v_0 = 5110 \pm 40$ m/s) with the first diagonal wave velocity from the 2D arrays ($v_{diag} = 4850 \pm 130$ m/s), they are consistent with this expected difference and are statistically distinguishable. Therefore observations of the SAW excited by 2D surface phononic crystals could offer simultaneous measurement of the multiple propagation directions needed to characterize materials with anisotropy across the in-plane directions.

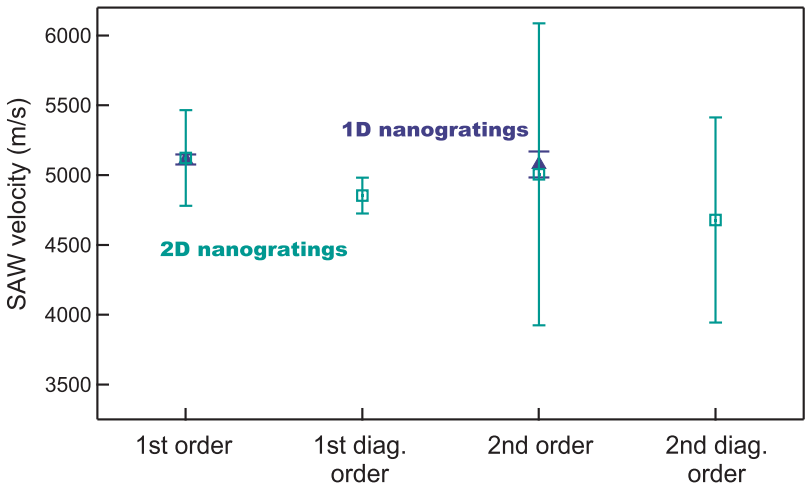

Figure 5.11: **Extracted velocities from 1D and 2D nanograting SAW** | By fitting a line to the long-wavelength SAW dispersion, we extract the velocity associated with each SAW order — the lowest two integer orders for the 1D nanogratings (blue triangles) plus two diagonal orders from the 2D nanogratings (green open squares). The overlapping measurements from 1D and 2D gratings agree well; the diagonal orders also match within error bars, but both appear slightly lower than the integer orders. This matches expectations for the known anisotropy of silicon.

5.5 Future opportunities in nano-mechanical characterization with EUV

Two distinct limitations are apparent in the methods discussed so far. The first is the need for nanostructures to achieve the small periodicities necessary to launch SAWs that are confined within ultrathin layers. Particularly as the film layers of interest become even thinner, the influence of the grating structures on the SAWs we measure and on the film material itself will be more significant. Moreover, the resonant LAW mode of the nanostructures will oscillate on a time scale much more similar to the longitudinal waves in the film, which may make it more difficult to extract the film's longitudinal properties. An adaptation of transient grating techniques that uses short-wavelength VUV or EUV pump beams could relieve these complications, and the photon flux achievable with present tabletop HHG sources is now high enough to make such experiments more plausible than they were a few years ago. However, the lack of simple reflecting and focusing optics at these wavelengths and the need to introduce relatively long delay times between pump and probe pulses still pose significant challenges. If VUV/EUV TG were implemented, though, it would greatly improve flexibility in the types of materials that could be studied without the need for strong absorption at visible wavelengths or the fabrication of nanostructures.

The second limitation, which would also still be an issue in a transient grating geometry, is the non-local nature of these measurements, averaging the elastic properties over the whole area that is probed. Here too, the application of dynamic imaging with EUV CDI could offer an extension to localized measurements of elastic properties. In particular, full maps of surface displacements caused by acoustic modes in anisotropic materials could be used for complete characterization of complex elastic tensors as in laser-based resonant ultrasound techniques [175]. Mechanical properties can also be used as a contrast mechanism for material-specific mapping of a surface which appears uniform to other types of microscopy [176]. Local mapping of elastic constants has even been used to identify the progression of malignancy in breast cancer cells [177]. In all these case, the enhanced spatial resolution available with EUV CDI would improve capabilities significantly, thereby opening opportunities for deeper studies of elastic properties at the nanoscale.

5.6 Conclusion

Here I have demonstrated that EUV nanometrology can be applied to characterize a wide range of ultrathin films, particularly emphasizing the layer-specificity which makes EUV-probed, short-wavelength acoustic nanometrology so attractive for the characterization of the mechanical properties of ultrathin films. Given the shortest SAW wavelengths we have observed with our technique at < 45 nm [41], this method of film characterization can extend directly to 10nm films. The changing layer sensitivity with SAW wavelength also shows that this could be applied to depth-profiling of inhomogeneous materials and multilayer stacks. I have also demonstrated the feasibility of using 2D nanodot arrays for a simultaneous measurement of SAW velocity in two directions across a surface to study materials with anisotropic elastic characteristics.

One great advantage of EUV nanometrology for thin film characterization is the possibility for a wide variety of separate measurements using the same setup. EUV high harmonics are sensitive to magnetic [178] and thermal dynamics (as discussed in Chaps. 3 and 4) and can also be used to directly image a nanostructured sample via coherent diffractive imaging [115]. Therefore this technique offers the possibility for the future development of a unique, flexible nanometrology tool capable of a wide variety of characterization modalities.

Chapter 6

Nanostructure metrology

The acoustic waves confined within ultrathin films proved a useful non-destructive tool in Chap. 5 for characterizing the elastic properties of films as thin as 50 nm where the density and thickness were independently known. Here I will show that these techniques can be extended to the study of the density and elastic properties of nanostructures with nickel (Ni) and tantalum (Ta) layers below 10 nm in thickness.

In particular, the SAWs excited below the structures will reveal the structure mass and density, while the LAW resonances of the structures themselves are very sensitive to the layer thicknesses and elasticity. In this case we use samples fabricated with carefully controlled layer thicknesses to focus on how elastic properties deviate from their bulk material counterparts. To resolve shifts in acoustic resonance frequencies below 1%, we again make use of the chirp z-transform (CZT) method introduced in Chap. 5 Sec. 5.3.1 for SAWs, and I will introduce a second frequency extraction method beyond simple Fourier transforms. Through the use of the Matrix Pencil Method, which is designed to extract both decaying and non-stationary oscillatory signal components, this second method significantly improves our experimental uncertainty in resonant LAW measurement.

This study represents the first to date to examine the elastic properties of ultrathin bilayers and extract the individual layer acoustic velocities. Here we observe their opposing trends in deviating from bulk properties and examine how one layer may influence the other. It is also the first demonstration of the EUV-based SAW mass sensor technique introduced by Nardi *et al.* [179] and proves that the density ratio of ultrathin material layers is not significantly different from bulk.

6.1 Nanoscale departures from bulk properties

While a significant departure from bulk mechanical properties for nanoscale materials was first observed in 1977 in superlattices with nanometer-scale periodicities [180], the precise mechanisms, magnitude and even sign of these changes are still open questions. A number of the earliest observations of superlattice in-plane stiffening $> 100\%$ were later attributed to artifacts of the bulge-testing measurement technique employed [181]. However, a number of more recent measurements with more reliable characterization techniques (like picosecond ultrasonics, nanoindentation and Brillouin light scattering, as discussed in Chap. 5 Sec. 5.2), and theoretical and simulation efforts observe and seek to explain nanoscale changes in elastic moduli.

In particular, stiffening by 14-50% has been observed for the in-plane elastic constant (controlling LAW velocity parallel to the surface and interfaces as $\rho v^2_{parallel}$) in superlattices [182, 183, 184]. The cross-plane elastic constant (perpendicular to the interfaces) softens by $\approx$ 15-30% with superlattice periods below 10 nm [182, 185, 186] or 40 nm [187] compared to what would be expected from the volume fraction of each material in the superlattice and bulk values for the individual elastic moduli. By varying the composition ratio in a series of Mo/Si superlattices, Pu *et al.* were also able to determine that the sound velocities in each of the 2-5nm material layers were both 2-6% lower than the corresponding bulk sound velocities [188]. Proposed mechanisms primarily focus on softening or weak bonding at the interfaces [182, 185, 186], or a change in the layer morphologies with smaller grain sizes in thinner layers leading to a larger volume fraction of softer intergrain space [187].

Results for nanoparticles and nanowires are even more mixed, with changes in elastic moduli ranging from -60 to +200% of the bulk material values [189, 190, 191, 192]. The much larger surface-to-volume ratio of nano-objects has led most explanations to consider effects of surface tension, surface energy and lack of surface bond coordination. However, some nanoparticle experiments which saw no change from bulk parameters suggest that most observed modifications may be due primarily to interactions with a substrate or other surrounding material [193, 194].

Measurements of sub-100nm metallic films have also observed a broad range of modification to the cross-plane elastic constant from -40% [195] to +15% [196] and changes which are not always monotonic with film thickness [196, 197, 198]. Softening was attributed to film defects [156], weak interfacial bonding [195], or lowered bond coordination contributing to differences in surface elastic constants [199, 200, 201]. The stiffening, on the other hand, can occur when a different process dominates the thin film behavior, whether strain in the films [196, 198] or electron redistribution at the surface [200].

There is not yet any comprehensive theory that predicts which materials should soften or stiffen or by what magnitude or at what size scale. The properties of the individual layers in a multilayer system have also not been explored in detail to understand how one might affect the other. Thus, there still remain many unanswered questions regarding the mechanical properties of materials in ultrathin films and nanostructures.

6.2 Samples for study of patterned films with sub-10nm layer thickness

To resolve the mechanical properties of the two components in an ultrathin bilayer film, we study a series of samples with varying composition. Ultrathin films of Ni and Ta are deposited on SiO_2/Si substrates (where the SiO_2 layer is 150-200 nm thick) using a calibrated sputtering deposition process to achieve precise layer thicknesses [195]. Sputtering rates are first calibrated using x-ray reflectivity (XRR) measurements of separate 30nm films of Ni and Ta. XRR employs the changing interference conditions of short-wavelength light reflecting from thin layers at different angles to precisely characterize film thickness and density. Even though the parameters must be extracted through a model-fitting process, the properties of $>$ 10nm single layers can be repeatably and uniquely determined in most cases. Then sputtering time is chosen to precisely deposit a 10nm layer of Ni for all samples and a Ta capping layer varying between 1-6 nm (see Fig. 6.1). This results in a thickness uncertainty of $\approx 5\%$ while layer thickness is varied by as little as 0.1 nm from sample to sample.

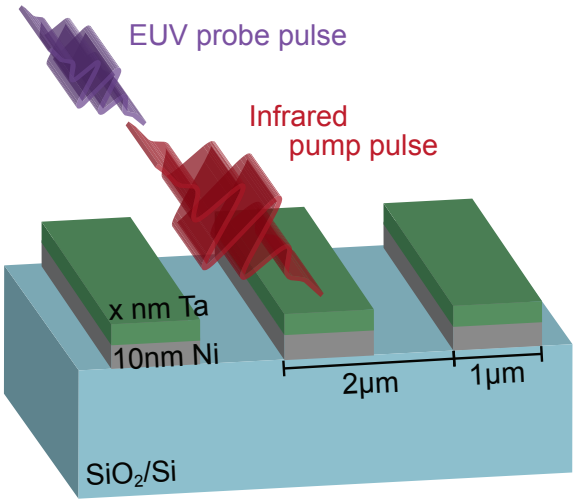

Figure 6.1: **Ultrathin bilayer samples** | To examine the mechanical properties of ultrathin bilayers, we study a series of samples with a Ni layer at a constant thickness of 10 nm and a Ta capping layer varying from 0 to 6 nm. As described in Chap. 2, the metallic structures absorb an infrared pump pulse and the change in diffraction of the EUV probe pulse follows the dynamics that ensue. Thus, while the large 1 μm linewidth implies these structures will exhibit essentially thin-film behavior, the periodic pattern gives us the probe diffraction that ensures sensitivity to the small surface displacements associated with nanostructure dynamics.

While XRR can also be applied to the ultrathin bilayers directly, the large number of model fit parameters and variation introduced by different fitting techniques, as shown in Fig. 6.2, make this an unreliable source of absolute thickness measurements. Particularly with such thin films, unique solutions are rare. To illustrate one apparent problem, consider the amount of Ta that is consumed to create a layer of tantalum oxide. The most stable oxidation state of Ta is +5 so that the typical oxide layer is Ta_2O_5 and has about 1 nm of thickness [202]. Given the Ta_2O_5 density $\rho_{oxide} = 8.20$ g/cm^3 [203], the surface density of a 1nm layer would be 8.20 $\times 10^{-7}$ g/cm^2. To determine the molar surface density, the molecular weights are required: $w_{Ta} = 180.948$ g/mol [202], $w_O = 15.999$ g/mol [204] and $w_{oxide} = 2w_{Ta} + 5w_O = 441.891$ g/mol. Thus the molar surface density is $\sigma_M = 0.0186$ $\times 10^{-7}$ mol/cm^2. There is twice this number of mols of Ta per cm^2 contained within the oxide, meaning that the surface density of Ta in the oxide layer is $\sigma_{Ta} = 2\sigma_M \cdot w_{Ta} = 6.731 \times 10^{-7}$ g/cm^2. This corresponds to $\sigma_{Ta}/\rho_{Ta} = 0.403$ nm of Ta lost per nanometer of oxide formed. However, XRR measurements from the sample which nominally had 1 nm of Ta initially deposited suggests that 0.4 nm of Ta remain below the oxide layer, but the 0.6 nm of Ta supposedly lost to oxidation would not be enough to form the 2.25nm oxide layer indicated.

On the other hand, sample-to-sample precision is strong, so that XRR characterization of this sample set demonstrates that the oxide and Ni layer thicknesses are essentially constant from sample to sample, and the Ta layer thickness grows as expected. Thus, nominal thicknesses can reasonably be used for analyzing the acoustic dynamics we observe; modifications suggested by the presence of the additional oxide layer are discussed below.

The films are then patterned using optical lithography and etched into a periodic array of wires that are 1 µm wide with a periodicity of 2 µm. Acoustic resonances of these arrays are excited by the infrared pump pulse absorbed in the metallic layers, causing an impulsive thermal expansion, as described in Chap. 2. We observe both individual longitudinal acoustic resonances in the through-thickness direction of each wire and surface acoustic standing-wave modes in the substrate launched by the whole array, with wavelengths set by the array periodicity and its higher harmonics [35, 41, 161]. The large wire width ensures that the longitudinal resonances we probe

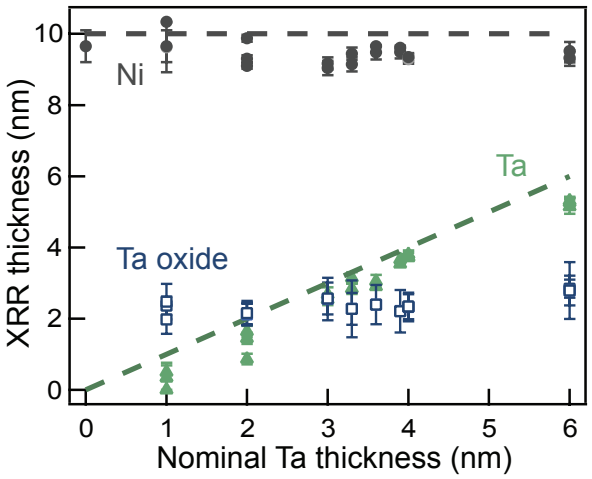

Figure 6.2: **X-ray reflectivity measurements of bilayer samples** | XRR requires fitting a model to reflectivity data to extract layer thicknesses and densities. The increased complexity of this model for multiple layers, along with the very small layer thicknesses represented in our sample set (down to 1 nm), makes it very difficult to find a unique solution. Different choices of input cause variations in the output fit parameters and uncertain levels of accuracy. For the three layers in our systems, Ni (grey circles), Ta (green triangles) and Ta oxide (blue squares), the error bars represent the fit uncertainty while multiple points at the same nominal thickness of Ta show the variability due to differences in the model fitting procedure. These measurements do indicate, however, that the Ni and Ta layers are essentially as they were designed, and the oxide layer is approximately constant from sample to sample.

are essentially those of thin-film bilayers, but the periodic pattern yields the diffractive interference that enables strong sensitivity to vertical displacements of the surface profile down to the picometer scale [40], as well as creating the periodic stress that launches the standing surface acoustic waves (SAWs).

6.3 Measuring material density with the surface acoustic resonance

SAW velocity is exquisitely sensitive to the mass of any structures on the surface, particularly for high-frequency SAWs since shorter wavelengths imply confinement to shallower layers below the surface where the wave velocity is most affected [179]. In Chap. 5 we needed to account for this effect by using finite-element simulation of the SAWs we observed experimentally to extract the 'real' elastic properties of thin films. Here, each sample with a different Ta layer thickness (over the constant thickness of Ni) exhibits a slightly different SAW velocity and oscillation frequency f_{SAW}, as shown in Fig. 6.3, and this can be used to gauge the structure mass.

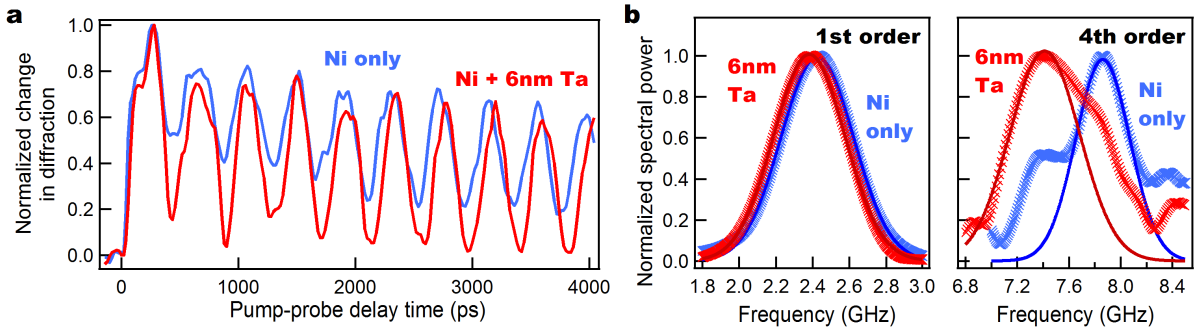

Figure 6.3: **SAW frequency shifts with Ta thickness** | **a.** The SAW frequency shift induced by adding 6 nm of Ta on top of 10 nm of Ni is clear in the raw change-in-diffraction signal. The additional mass slows the wave propagation, lowering the oscillation frequency. **b.** Because the frequency shifts are very small, we employ the chirp z-transform to generate high-resolution spectra, plotted in crosses, near the resonance peaks (examples of the fundamental and 4th-order peaks are shown here for the two raw-data curves from part **a**). The center frequencies are extracted by Gaussian fit functions (solid lines).

6.3.1 Extracting small frequency shifts with high resolution using CZT

With the large array periodicity present in our sample set, the SAW frequency shifts induced by the changing Ta mass are quite small: only around 30 MHz, or about 1%, across the whole range of samples for the fundamental SAW order. To extract the SAW frequencies with enough precision to resolve this small change, we again apply a CZT [170] to obtain the frequency spectrum near the frequency peak, shown in Fig. 6.3b. More detail is given in Chap. 5 Sec. 5.3.1. The average fitted peak values from many scans on the same sample yield the results reported in Fig. 6.4. The error bars represent the standard deviations of these measurements. This procedure yields frequency uncertainties of less than 0.5% for the fundamental order and better than 2% for the higher orders.

6.3.2 Interpreting frequency-shift data

The change in the volume of Ta from sample to sample can be derived from the known change in thickness. The SAW frequency shift can be related to the implied mass change, leading to a measure of material densities. Specifically, we see that the SAW frequency decreases linearly with Ta thickness. Fitting this line yields values for two parameters: the slope γ, and intercept f_0. The relationship between f_{SAW} and Ta volume has slope $\alpha = \gamma/(Lz)$ where L is the linewidth of the wires and z is the length of the wires. Then the relationship of f_{SAW} to wire mass must have slope $\beta = \alpha/\rho_{Ta}$ where ρ_{Ta} is the density of the Ta layers. Since we also know v_0 for when the mass of the wire is equal to the mass of just the 10nm layer of Ni m_{Ni}, $\beta = (f_0 - f_s)/m_{Ni}$ where f_s is the SAW frequency for the same wavelength propagating along the bare substrate surface. The frequency f_s must be known *a priori*, as for example by using finite-element analysis and literature properties for the materials comprising the substrate to identify the dominant excited modes [161, 205, 206]. Therefore,

$$\rho_{Ta} = \frac{\alpha}{\beta} = \frac{\gamma}{Lz}\frac{m_{Ni}}{f_0 - f_s} = \frac{\gamma}{Lz}\frac{\rho_{Ni} h L z}{f_0 - f_s} \tag{6.1}$$

where ρ_{Ni} and h are the density and thickness of the Ni layer, respectively. While the densities of

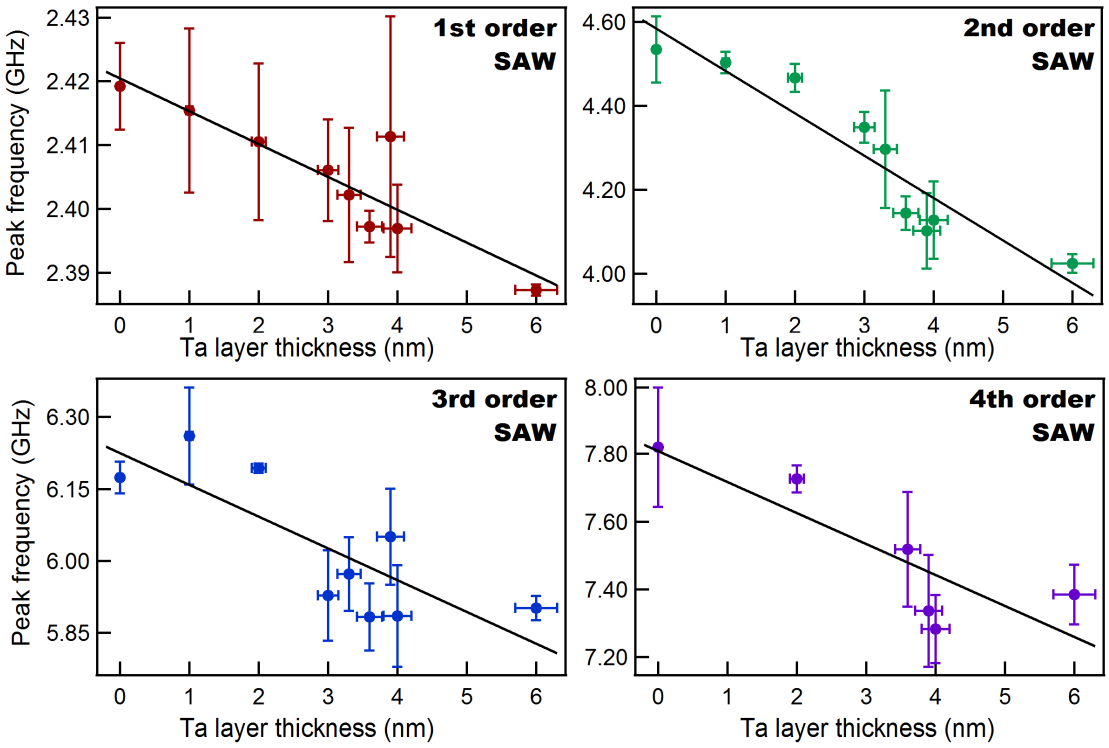

Figure 6.4: **Extracted SAW frequency shifts in four harmonics** | The increase of Ta thickness from sample to sample results in a linear shift in the SAW frequency. This is visible in all the four lowest-order SAW harmonics, but the magnitude of change is significantly higher for higher orders. This is because the shorter wavelength implies the wave propagation is confined closer to the surface where the material is most affected by the extra mass in the bilayer structures. The linear fits to each set of data are used to calculate the Ta-to-Ni density ratio.

Table 6.1: Fit results from SAW resonances for the lowest four SAW orders.

	1st order	**2nd order**	**3rd order**	**4th order**
f_0 (GHz)	2.420 ± 0.003	4.584 ± 0.048	6.23 ± 0.06	7.81 ± 0.11
γ (GHz/nm)	-0.0051 ± 0.0009	-0.101 ± 0.014	-0.067 ± 0.019	-0.092 ± 0.028
ρ_{Ta}/ρ_{Ni}	1.93	13.88	1.70	1.88

the two materials in the bilayer cannot be independently determined in this way, the ratio between them can be found as

$$\frac{\rho_{Ta}}{\rho_{Ni}} = \frac{\gamma h}{f_0 - f_s} \ . \tag{6.2}$$

Linear fits to the SAW frequency data for each of the first four SAW harmonics, shown in Fig. 6.4, yield values for the Ta-to-Ni density ratio calculated according to Eqn. 6.2. These results are reported in Table 6.1. The values obtained from the 1st, 3rd and 4th harmonics are consistent with each other while the ratio extracted from the 2nd-order SAW data is significantly higher. Possible causes for such a large discrepancy are the subject of ongoing discussion. Averaging the three similar values yields $\rho_{Ta}/\rho_{Ni} = 1.84 \pm 0.12$, which is somewhat lower but statistically consistent with the ratio of the bulk material densities, 1.92 [207]. Note that because this measurement relies on the slope of the lines with respect to the change in Ta thickness, the presence of a constant oxide layer will not alter the conclusions.

This measurement demonstrates the first all-optical, non-destructive characterization of the density ratio between materials in ultrathin bilayers. Notably the slope is significantly higher for higher SAW harmonics due to the higher mass sensitivity enabled by shorter wavelengths. This illustrates that greater precision for density measurements with this technique could be attained by using shorter array periodicities.

6.4 Characterizing elastic properties with the longitudinal acoustic resonance

While the SAW dynamics dominate the diffraction signal over many nanoseconds, Fig. 6.5 shows that the first 20 picoseconds following excitation by the pump pulse reveal the resonant longitudinal oscillation of the wires themselves [156]. Again the frequency shifts significantly as the Ta thickness is varied. Also, by comparing three identical Ni/Ta film samples etched for different amounts of time, we verify that the resonant frequencies we measure are not systematically affected by potential over-etching of the wire pattern into the substrate (see examples in Fig. 6.6). This ensures that the shifts we observe are uniquely related to the changing Ta thickness.

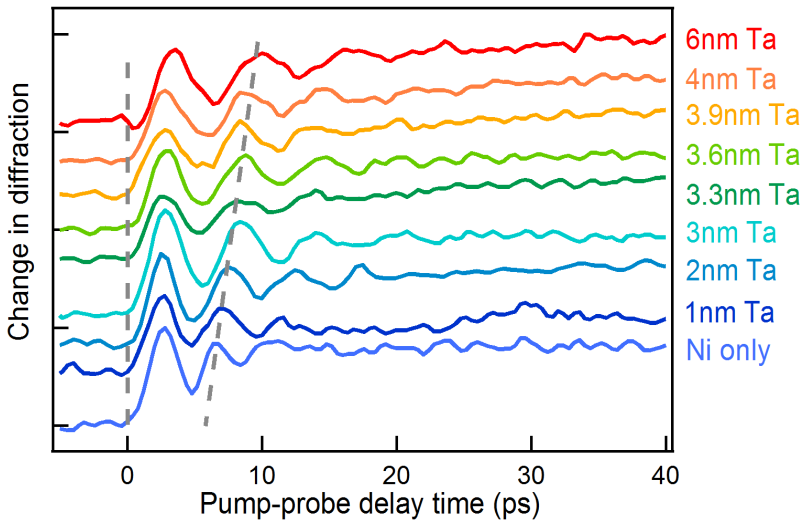

Figure 6.5: **LAW resonances observed as a function of Ta thickness** | The increase of Ta thickness from sample to sample also results in a shift in the resonant LAW frequencies of the bilayers themselves. The dashed lines serve as guides to the eye, marking time-zero and the shifting location of the second oscillation maximum.

6.4.1 Extracting LAW periods from fast damping using MPM

The fast decay of the LAW oscillations makes a Fourier transform, which assumes stationary oscillations, an inappropriate and unreliable tool for extracting the resonant frequencies. Instead we employ the Matrix Pencil Method (MPM) which projects a function onto the set of exponentials

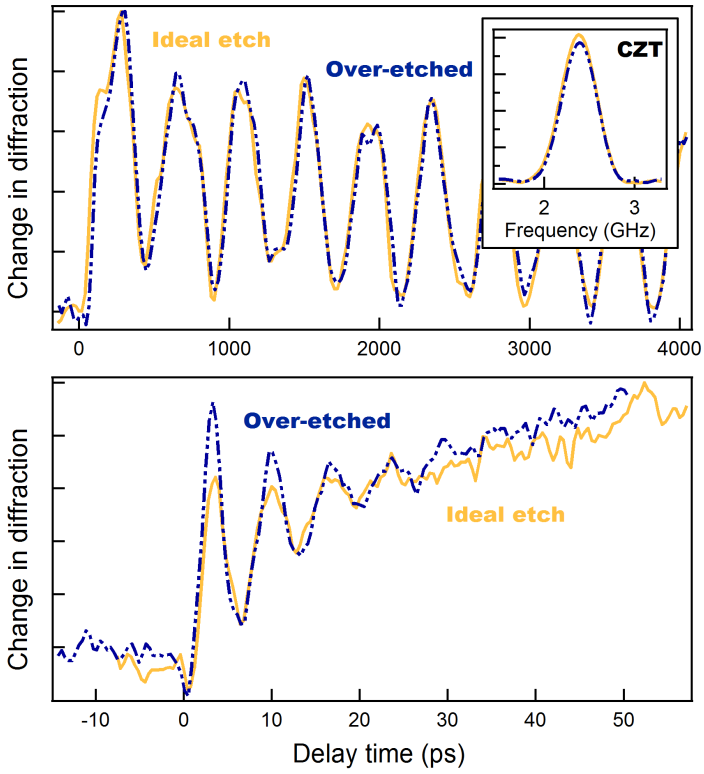

Figure 6.6: **No systematic effects due to etch depth** | By testing three samples etched to different depths from the same 10nm Ni/6nm Ta bilayer, we confirm there are no systematic effects in our observations of resonant LAW and SAW frequencies arising from potential over-etching into the substrate. These plots compare the SAW signals with their CZTs (top) and LAW signals (bottom) from the ideal-etch (solid orange) and the most over-etched (dash-dot blue) samples.

with complex exponents e^{a+bi} to a specified precision limit, allowing it to reliably capture both oscillation frequencies and damping rates of the signal components isolated from the noise inherent to experimental data [208, 209, 210]. As shown in Fig. 6.7 we remove irrelevant parts of the data — namely the signal before time-zero and the background rise due to thermal expansion and the onset of the first surface acoustic oscillation.

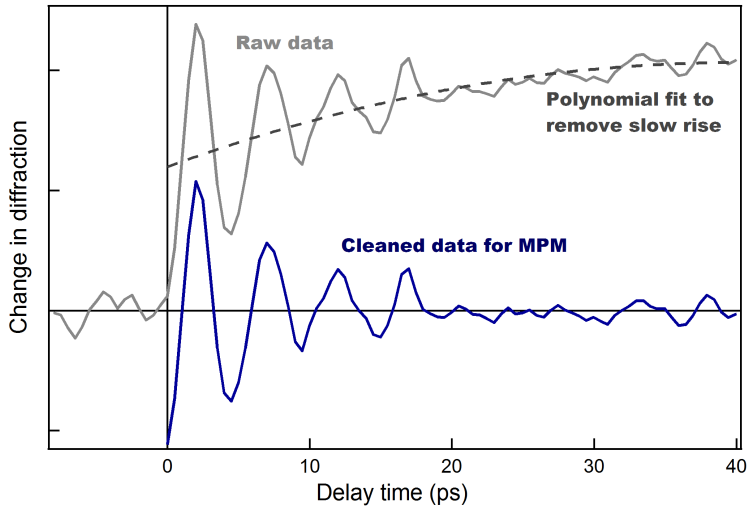

Figure 6.7: **Preparing LAW data for MPM** | To achieve the best results from the MPM algorithm, we first clean out the irrelevant parts of the measured signal (solid grey) by cutting off the points from before time-zero and subtracting out a polynomial fit (dotted grey) to remove the slow background rise. From the remaining signal data (blue) we construct the Hankel matrix for use in MPM.

The cleaned data is used to construct a Hankel matrix. For (2n+1) data points $[a_1, a_2, a_3, ...a_{2n+1}]$, this matrix takes the form

$$\begin{bmatrix} a_1 & a_2 & a_3 & \dots & a_n \\ a_2 & a_3 & a_4 & \dots & a_{n+1} \\ a_3 & a_4 & a_5 & \dots & a_{n+2} \\ \vdots & \vdots & \vdots & \ddots & \vdots \\ a_n & a_{n+1} & a_{n+2} & \dots & a_{2n+1} \end{bmatrix} \tag{6.3}$$

The singular value decomposition of this matrix gives something analogous to eigenvalues and eigenvectors that can represent the underlying organization of patterns in the data. A plot of

the relative strength of the singular values, shown in Fig. 6.8a, shows a sharp transition from signal components to a long tail of random noise where all the modes are similarly populated. The number of values appearing before this transition represents the number of signal components that exist above the noise level. In this example, two are clearly visible. They represent the complex exponentials with positive and negative imaginary parts of the same magnitude which sum into the real oscillation signal visible in Fig. 6.7. MPM then constructs a new matrix from the singular vectors corresponding to the signal components identified and finds the eigenvalues that give the complex exponentials that best represent each signal component. Figure 6.8b shows where the two exponential components lie in the complex plane for our signal from Fig. 6.7. The symmetric placement on either side of the real axis again displays that they combine to form the real oscillation of the signal. Their location inside the unit circle arises because the signal decays. Stationary oscillations would lie on the unit circle with modulus one. Pure exponential decay components (like the thermal decays we observe in long time scale data) appear as individual nodes on the real axis inside the unit circle.

The real component gives the amplitude decay while the imaginary components give the oscillation period and initial phase. Plotting the extracted oscillatory component with the original data in Fig. 6.9 shows that the overlap is very good. Moreover, the residual difference between the measured data and the extracted oscillation (shown in grey) is comparable to the noise signal recorded before time-zero (red).

While the same amplitude, period and phase parameters could be accessed via a least-squares fit to the data, in practice, results are significantly more reliable when using MPM. In particular, they are not strongly influenced by choices like the starting guesses for least-squares algorithms, and in this data set MPM generally lowered the relative uncertainty in the extracted periods by a factor of about five. In this way we extract the set of oscillation periods shown in Fig. 6.10 with uncertainties below 0.7%.

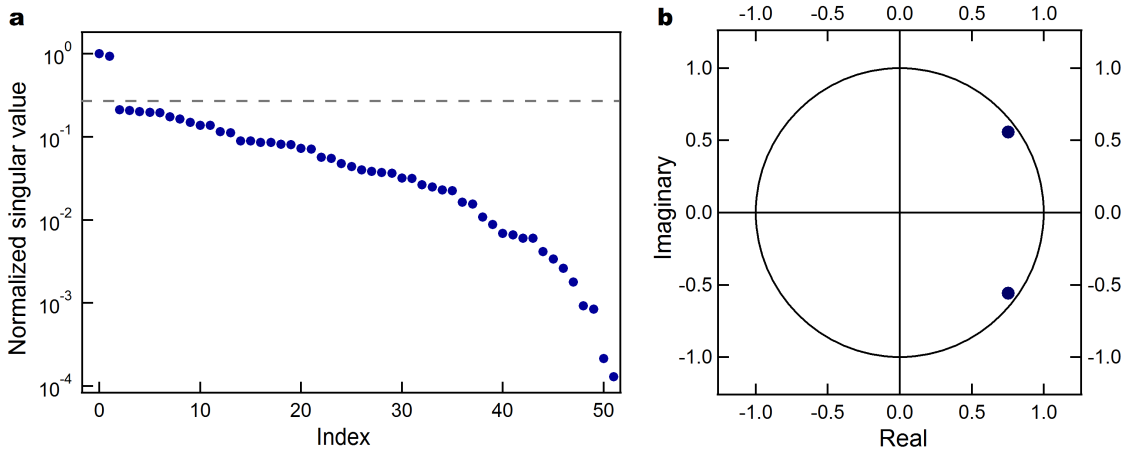

Figure 6.8: **Separating data from noise with singular values** | **a.** A plot of the singular values from the data shown in Fig. 6.7 displays a sudden jump between the two strong signal components and a long tail of similarly-valued noise components. We use this cut-off, marked by the dashed line, to select the number of signal components to solve for using MPM. **b.** The output of MPM then gives the nodes in the complex plane corresponding to the complex exponential that best represents each signal component. The oscillation visible in Fig. 6.7 shows up here as a pair of nodes with the same magnitudes of real and imaginary parts but opposite sign on the imaginary part. Pairs like this sum to a real oscillation signal with frequency (or period) given by the magnitude of the imaginary part and amplitude decay time given by the magnitude of the real part. Both lie inside the unit circle, because the oscillation is decaying rather than growing or remaining stationary. Non-oscillatory decaying signal components would appear as individual nodes on the real axis inside the unit circle.

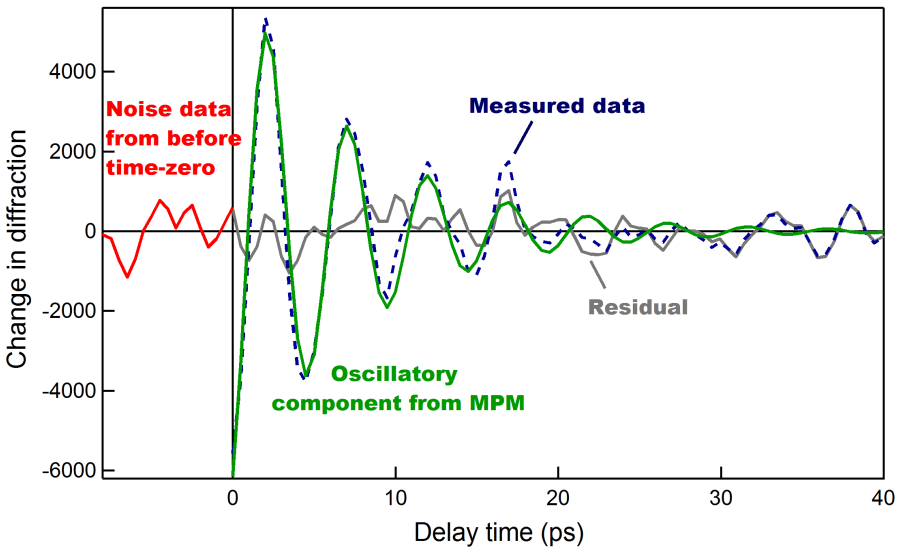

Figure 6.9: **Comparing MPM output with measured data** | The residual difference (grey) between the measured data (dotted blue) and the oscillatory signal component extracted using MPM (green) is comparable in magnitude to the noise signal recorded before time-zero (red). Thus it is reasonable to assert that the MPM-extracted component successfully accounts for all the signal above the noise level in our measurement.

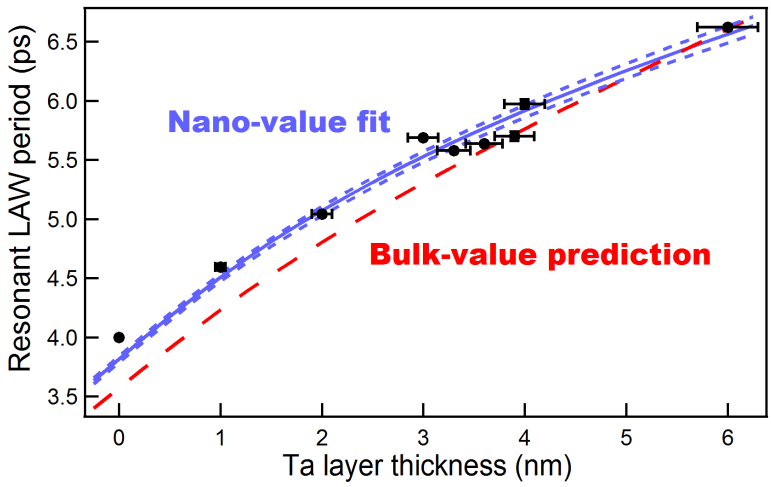

Figure 6.10: **Extracted resonant LAW periods** | The resonant LAW periods of the bilayer structures extracted by using MPM clearly are not well matched by the predictions resulting from bulk material parameters (dashed red). Instead, we use a least-squares optimization algorithm to fit the data in order to extract effective nanoscale longitudinal velocities of the Ni and Ta layers. This fit is plotted in solid blue, while the dashed blue lines mark the fits to the diagonal extremes of the error bars and indicate the upper and lower bounds of the extracted effective velocities. Note however that the data point at 0 nm of Ta thickness (the Ni-only sample) must be excluded to achieve a good fit to the rest of the data. The vertical error bars on the data points (most of which are too small to distinguish from the points themselves) represent the variation in the MPM-extracted periods related to different choices of the data starting point and number of singular vectors to keep as signal. The horizontal error bars represent the 5% uncertainty in layer thickness resulting from the calibrated sputtering deposition process.

6.4.2 Interpreting LAW oscillation periods

The resonant frequencies of a bilayer can be calculated by enforcing the condition that (displacement, stress) = (**u**,0) be an eigenvector of the appropriate acoustic transfer matrix (stress-free boundary condition), as in calculating the localized surface modes of a semi-infinite superlattice [195, 211]. Like the optical transfer matrix method for calculating the propagation of electromagnetic waves across layered media, the acoustic transfer matrix applies continuity conditions for the stress and displacements across boundaries from one medium to the next to construct the matrix operation that relates an input field to the output field at the next boundary.

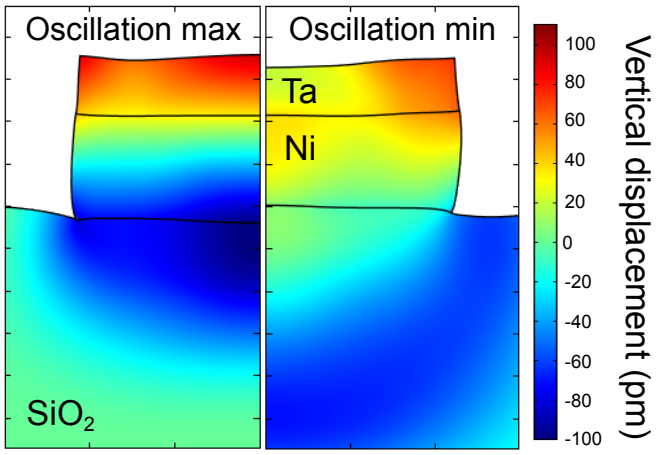

Figure 6.11: **Finite-element model of the open-pipe-type resonant mode** | Comparison of the displacement fields calculated by finite-element-analysis [212] at the peak and subsequent valley of the oscillation in the diffraction signal from our Ta/Ni bilayers on SiO_2 (seen in Fig. 6.10) clearly reveals the symmetric shape of the mode, placing antinodes at both the top surface and the interface with the substrate.

In our case where the SiO_2 substrate has lower acoustic impedance than the Ni layer, the resonant modes will be analogous to organ-pipe modes with two open ends (see Fig. 6.11); i.e., the resonant frequencies will be the same as those for an unsupported bilayer membrane with antinodes (and the stree-free boundary condition applied) on both sides [213]. We test this principle by simulating the laser excitation and subsequent dynamics of excited metal lines on substrates with Young's modulus varying from 10 to 1000 times stiffer or softer than the metals [212].

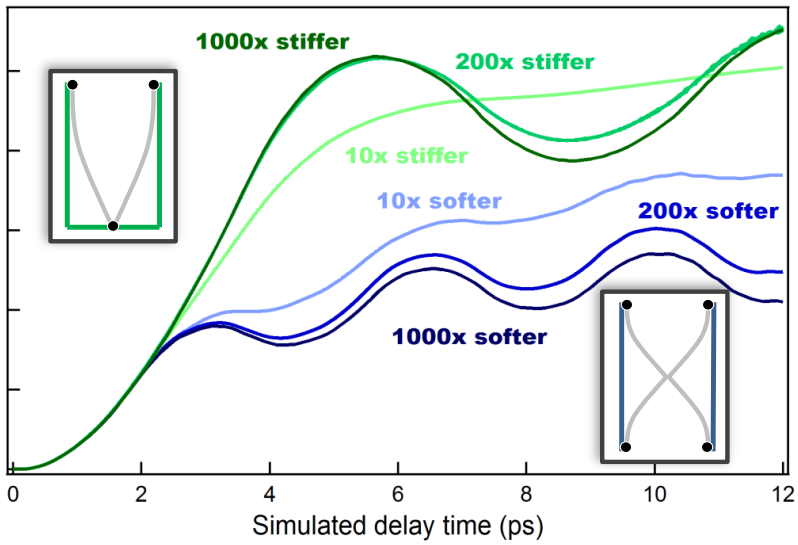

Figure 6.12: **Resonant frequency determined by sign of acoustic mismatch** | Simulated signals compare the resonant LAW periods for cases where the substrate is 10-1000 times stiffer (green) or softer (blue) than the metallic structures. This confirms the idea that the magnitude of acoustic mismatch effects the oscillation amplitude, but the period only relies on the sign of the mismatch — all the stiff substrates result in a period that is twice that from the soft substrates (even for the very low-amplitude oscillation seen for the substrate that is 10× stiffer). The two insets schematically represent this difference between closed-pipe and open-pipe resonances with anti-nodes at the open ends and a node at the closed end.

The simulation results in Fig. 6.12 clearly show that while the amplitude of oscillation is strongly related to the degree of acoustic mismatch between the structures and the substrate, the resonant periods are set only by whether the substrate is stiffer or softer. Also, the periods on the soft substrate are indeed what would be expected from free-standing membranes. Therefore they can be calculated by enforcing the eigenvector condition for a transfer matrix corresponding to one-way propagation across the Ta and Ni layers. This transfer matrix τ is given by

$$\tau = \begin{pmatrix} \cos(q_{Ni}d_{Ni}) & \sin(q_{Ni}d_{Ni})/\omega Z_{Ni} \\ -\omega Z_{Ni}\sin(q_{Ni}d_{Ni}) & \cos(q_{Ni}d_{Ni}) \end{pmatrix} \times \begin{pmatrix} \cos(q_{Ta}d_{Ta}) & \sin(q_{Ta}d_{Ta})/\omega Z_{Ta} \\ -\omega Z_{Ta}\sin(q_{Ta}d_{Ta}) & \cos(q_{Ta}d_{Ta}) \end{pmatrix} \quad (6.4)$$

where ω is the LAW angular frequency, d_x is the thickness of the respective layers, Z_x is the acoustic impedance ($Z_x = \rho_x v_x$ for LAW velocity v_x) and $q_x = \omega/v_x$. We require

$$\tau \begin{pmatrix} \mathbf{u} \\ 0 \end{pmatrix} = \lambda \begin{pmatrix} \mathbf{u} \\ 0 \end{pmatrix} \quad (6.5)$$

for any scalar eigenvalue λ. The second component of this matrix equation implies that resonant frequencies will solve the transcendental equation

$$\tan\left(\frac{\omega d_{Ni}}{v_{Ni}}\right) + Z_{Ta}/Z_{Ni}\tan\left(\frac{\omega d_{Ta}}{v_{Ta}}\right) = 0. \quad (6.6)$$

Note that these equations simplify dramatically in the long-wavelength limit ($q_x d_x \to 0$), predicting an effective velocity through alternating material layers that is set by the weighted average of the cross-plane elastic constants $C = \rho v^2$ of each material ($(d_1 + d_2)/C_{eff} = d_1/C_1 + d_2/C_2$) or of the individual acoustic velocities for the further case of low impedance mismatch

($Z_1/Z_2 \rightarrow 1$). But these cannot be applied to our case where the wavelength of the open-pipe resonance is twice the total thickness of the bilayer. Furthermore, we confirm that the full transfer matrix approach is the only one to reliably predict the resonant frequencies extracted by MPM from simulations with finite-element models where layer thickness and acoustic properties are precisely known inputs for the simulation.

As shown by the red dashed line in Fig. 6.10, the resonant periods predicted by this approach using bulk material properties clearly fail to match those we observe experimentally as the Ta layer thickness is varied.

Before analyzing the data further to understand how layer properties may deviate from those of bulk materials, it is important to consider how the presence of the typical tantalum pentoxide layer on Ta would affect our measurements. Since every nanometer of Ta_2O_5 that forms consumes approximately 0.4 nm of Ta (as calculated in section 6.2), we compare simulated dynamics of the Ni/Ta bilayer with nominal thicknesses to those of a Ni/Ta/Ta_2O_5 system with nominal Ni thickness and nominal Ta thickness minus 0.4 nm per nm of added oxide. Given literature values of all material properties for the sake of comparison, we find that the resonant frequencies from the two simulations are the same within our experimental error bars; the effect of the excess oxide is essentially compensated by the Ta loss so that it is reasonable to conduct our analysis assuming the nominal Ni and Ta thicknesses and no oxide. Therefore, we conclude that the discrepancy between the observed resonant periods and those predicted by bulk material properties can be attributed primarily to changes in the elastic properties of the ultrathin layers.

We then use v_{Ni} and v_{Ta} as our only fit parameters in a least-squares optimization algorithm using Eqn. 6.6 to find the effective nano-layer velocities that provide the best fit to the data. Specifically, for a wide range of values for v_{Ni} and v_{Ta}, we use Eqn. 6.6 to solve for the largest resonant periods (corresponding to the lowest-order mode that we observe) for each bilayer sample predicted by every possible pair. To enable the best comparison to the data, we fit a low-order polynomial to the data points which will serve as a representation of the data over the range of measurement. We then calculate the root-sum-squared difference between the polynomial fit to

the measured periods and each set of predicted periods and seek the minimum (see Fig. 6.13). We also compare this residual function to the average uncertainty in our data points, marked by the plane crossing the surface. Because the transcendental equation is very sensitive to the input parameters, I find that using the polynomial representation, which assumes that the period should change smoothly as the Ta thickness is varied, to mediate the comparison with predictions enables a more consistent result. It also produces a lower final residual between the fit and measured data than is obtained by fitting the data points directly with this algorithm.

However, we find that the point from the Ni-only sample (at Ta thickness = 0 nm) must be excluded to achieve a good fit to the rest of the data. This is quantified in the comparison of the residual surface to the error plane representing the uncertainty in the measured data: when the Ni-only sample point is included in the fitting algorithm, the surface never drops below the error plane.

The blue solid line in Fig. 6.10 displays the final fitting result, while the blue dotted lines mark the outer bounds determined by fitting the diagonal extremes of the error bars on each data point. The effective longitudinal velocities extracted are summarized in Table 6.2. Note that the effective velocities differ significantly from their bulk counterparts. Moreover, the best-fit v_{Ni} is indeed significantly different from the value associated with the Ni-only resonant period τ, calculated by $v_{Ni,only} = 2d_{Ni}/\tau$. This implies both that the 10nm layer of Ni has different elasticity from that expected for a bulk material and that it is further modified by the addition of the Ta layer — though in a way that lessens the difference from bulk elasticity. Moreover, the two layers deviate from their bulk counterparts in opposite ways such that they are more similar to each other than bulk Ni is to bulk Ta. It should be noted that this should not be caused by significant intermixing between the two materials since independent measurements on similar samples show that the magnetic properties of the Ni layer remain those of pure Ni.

Fitting the data in this way presumes that the elastic properties of Ni and Ta are constant across the entire set of samples. While this is a reasonable assumption for the constant 10 nm layer of Ni, one could argue the Ta layer may well behave differently at 1 nm of thickness than

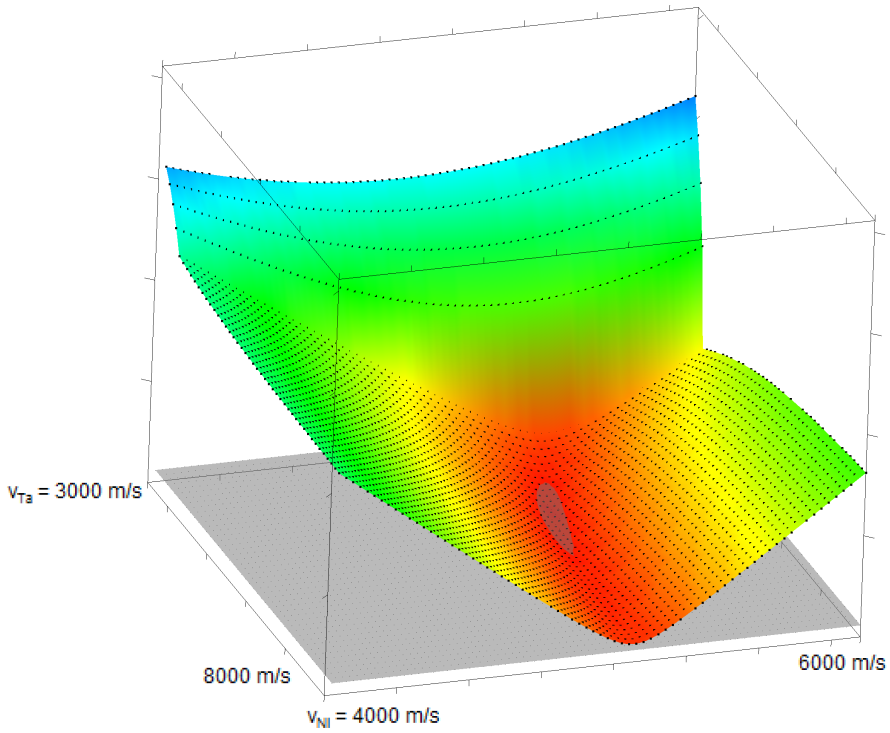

Figure 6.13: **Best-fit residual surface for range of v_{Ta} and v_{Ni}** | To find the best-fit effective velocities of nickel and tantalum, we use many possible pairs of v_{Ni} and v_{Ta} to predict the periods that would correspond to our set of bilayer samples. This surface plots the root-sum-squared difference between those predictions and the polynomial representation of the data for each pair, and the minimum will mark the least-squares best-fit pair of velocities. The grey plane marks the level of data uncertainty. Where the surface drops below this plane, possible solutions are indicated.

Table 6.2: Fit results from the LAW resonances of the Ni/Ta bilayers. Bulk values from [207].

	Bulk v_{LAW} (m/s)	**Best-fit v_{LAW} (m/s)**
Ni only	5600	5000 +10/-10
Ni under Ta	5600	5240 +40/-30
Tantalum	4100	5180 +150/-170

at 6 nm. Given the lower sensitivity of the measured oscillation periods to the Ta velocity in the thinnest layers we examine, we can neither confirm nor rule out this possibility. If we assume the v_{Ni} extracted by the method outlined above and then solve for v_{Ta} with each measured period (as represented by the polynomial fit), we find the trend shown in Fig. 6.14, which shows that our set of measured periods would be consistent with an effective velocity in Ta that varies from 5000 m/s at 6 nm to about 6000 m/s for < 3 nm. Notably, trying to solve for the varying v_{Ta} using either $v_{Ni,only}$ or the data points directly (rather than the polynomial representation) results in there being no solutions to Eqn. 6.6.

6.4.3 Potential mechanisms for modified nanoscale elastic parameters

A number of mechanisms for nanoscale elastic changes in films and superlattices of the magnitude that we observe have been proposed. For example, the atomic layers near a surface will exhibit different elastic constants than those deep within a volume, and these layers will make up a significant portion of ultrathin films [199]. However, the surface elastic constants calculated by Shenoy [214] suggest a change that is at least an order of magnitude smaller than we observe.

Interface layers and bonding across them will also influence the effective elastic constants we extract. In particular, the fact that the ultrathin Ni layer alone behaves differently than the Ni layers under Ta lends evidence to the importance of these effects. Mismatch between different materials and residual stress have been used to explain some elasticity changes comparable to those we observe [167], although the trends predicted by more rigorous models for this effect [185, 186] do not account for what we observe. Softening due to a weak interfacial bond or, equivalently, interface layers with different properties than a bulk-like core was modeled by Rossignol *et al.* [195], but notably their single parameter describing the displacement discontinuity across the interface does not allow enough freedom to fit our data if either bulk velocities, or $v_{Ni,only}$ and the best-fit v_{Ta} are assumed.

Ultrathin films are also prone to large volume fractions of defects or soft intergrain areas between small grains which will contribute to an apparent overall softening of the film material

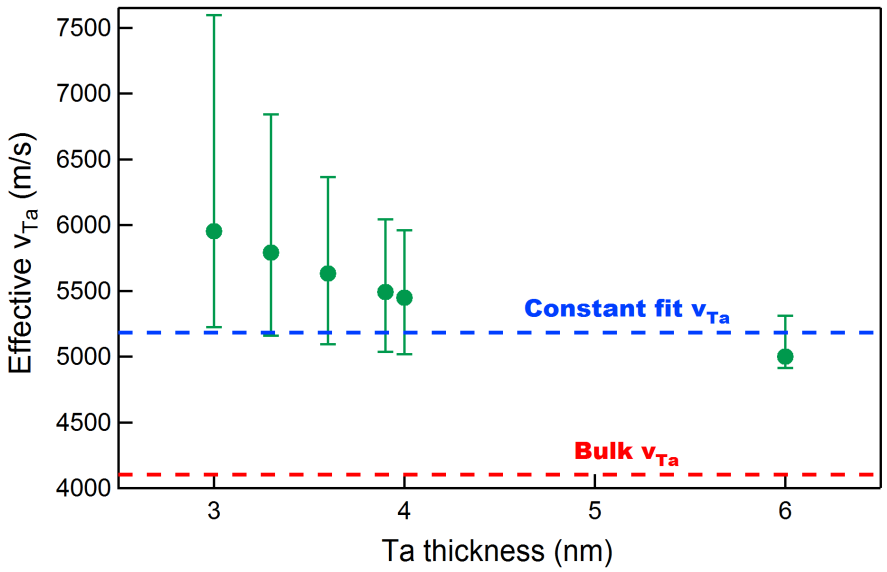

Figure 6.14: **Possible variation in Ta velocity** | If the constant v_{Ni} fitted to the data is assumed, one can solve for the v_{Ta} implied by each data point. As apparent from the error bars (obtained by solving at the upper and lower bounds of v_{Ni}), the thinner films trend upward, but the error bars are always consistent with constant value fit to the whole data series (blue dashed line). All are still significantly above the bulk Ta velocity (red dashed line). The error bars also increase drastically with thinner Ta as the layer has less effect on the measurement; indeed, below 3 nm the effect is too low to calculate any solution.

[156, 187, 198, 215]. Stiffening is less often observed, but it has typically been attributed to strain-induced changes in third-order elasticity [156, 197, 198, 216]. In particular, Ogi *et al.* [197] observe a correlation between measured out-of-plane strain and the stiffening of Pt and Fe films. However, to our knowledge, changes of the magnitude exhibited by our Ta layers have not been previously observed in metallic films.

It is likely that many of these effects contribute to the changes in elastic properties that we observe. Further characterization using multiple techniques to analyze film microstructure (as with transmission electron microscopy) and lattice strain (as with x-ray diffraction), as well as exploration of how fabrication techniques (for example, sputtering vs. ALD) and conditions affect the elasticity changes, could illuminate more of the specific mechanisms involved.

Exciting higher-order LAW resonances in the bilayers could also reveal more about the importance of changes localized around interfaces [156]. The symmetric mode with anti-nodes at the surface and substrate interface of our bilayers incorporates little displacement near the interface between the ultrathin layers, which is close to the node of the resonant mode. In contrast, the second-order mode would see an anti-node in the center of the bilayer, and could therefore be more sensitive to elastic properties at the middle interface (particularly when the two ultrathin layers have similar thickness). In our previous work, we introduced a Michelson interferometer into the pump beam line to split the pump into two pulses separated by a variable time delay (introduced by a variable optical path length in one arm of the interferometer) [41]. There we demonstrated that the time delay between the two pump pulses could be set to selectively suppress or enhance different SAW orders (see Fig. 6.15). For example, by setting the delay time equal to half the period of the fundamental SAW, the fundamental oscillation is completely suppressed while the second-order mode is reinforced and slightly enhanced. This same principle could be applied to excite the second-order LAW resonance of nanostructures.

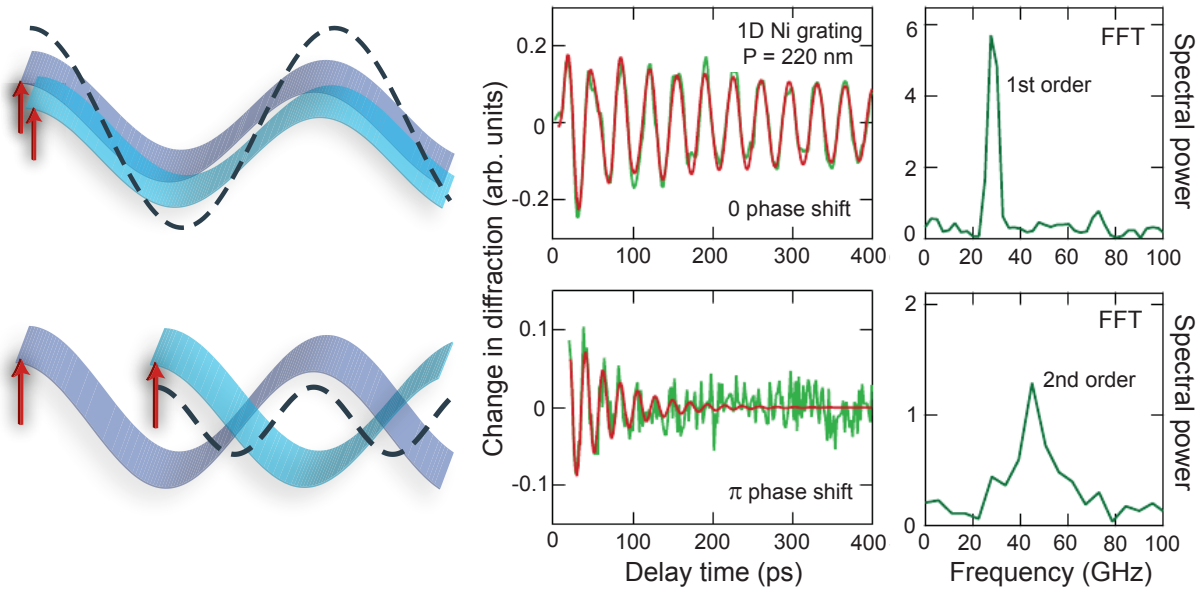

Figure 6.15: **Double pump for selective acoustic excitation** | Two pump pulses can be used to selectively excite specific acoustic modes by setting the delay time between them to suppress or enhance particular frequencies, represented schematically on the left. When the two pump pulses (red arrows) excite the system at the same time (top), the two excitations (blue and purple) reinforce each other and the fundamental SAW mode is primarily excited; when they are offset by a time delay equal to half the fundamental SAW oscillation period (π phase) (bottom) the second-order mode is reinforced while the fundamental is suppressed (visible in the dotted line, which shows the lowest-order mode that can be excited in this case). This effect is clearly observed in the experimental signals from the same sample at two pump offsets and Fourier transforms of the signals shown on the right. This principle could also be applied to selectively excite higher-order LAW resonances. Figure adapted from [41].

6.5 Conclusions and outlook

In this chapter I have demonstrated the first application of the EUV-based SAW mass sensor proposed by Nardi *et al.* [179] to show that the density ratio of Ta to Ni in sub-10nm films is not significantly changed from that expected from bulk materials. However, the LAW resonances of the bilayer reveal that elastic properties are significantly modified. In particular, we observe that within the same bilayer, the ultrathin films of Ni and Ta soften and stiffen relative to their bulk counterparts, respectively. Moreover, the presence or absence of the Ta capping layer further influences the effective properties of the Ni layer. The precision of this measurement was limited primarily by the uncertainty in layer thickness.

On one hand the sensitivity to atomic-monolayer differences in thickness poses challenges for precise characterization of mechanical properties. Other film deposition processes, like atomic layer deposition with its carefully controlled layers, will allow us to address this issue in future experiments, as well as to study how different interface types and qualities may further affect the observed elastic properties. Importantly, this metrology technique can be applied as easily to wide film-like structures as to narrow nanowires or nanodots, enabling unprecedented metrology for small-volume structures that are inaccessible to many other techniques.

On the other hand, the strong sensitivity of the acoustic resonances to the size and elasticity of the structures will allow mapping of variation in height, for example, across many nanostructures, particularly with the possibility of extending this technique to localized measurements with dynamic coherent diffractive imaging. Such non-destructive measurements would enable very strong tests for the repeatability of fabrication techniques and for understanding how various processes can affect the morphology and structure of materials at the nanoscale.

Chapter 7

Conclusions and Future Opportunities

By directly observing the thermal and acoustic dynamics of nanoscale systems with coherent extreme ultraviolet light, this thesis demonstrates new insight into how and why material behavior deviates from that observed in bulk systems. It represents the distillation, reduction, analysis, interpretation and understanding of around 20,000 files of raw data collected over more than 300 days/nights, accumulating well over 3000 hours of camera exposure time collecting more than 43 billion diffracted EUV pulses to characterize a variety of nanostructured samples. To summarize the primary results presented:

- Observations of heat dissipation from the smallest nanoscale heat sources measured to date ($\approx$ 20 nm) have revealed a new regime of nanoscale thermal transport that dominates when the separation between nanoscale heat sources is comparable to the dominant phonon mean free paths [58, 59]. In this efficient collectively-diffusive regime of thermal transport, closely-spaced nanoscale heat sources cool faster than isolated sources of the same size, potentially mitigating projected problems for thermal management in nano-electronics, where the power density is likely to increase as the individual nanostructures shrink in size [6, 60]. It also highlights important design implications for nanostructured materials and devices for energy and biomedical applications.

- The collectively diffusive regime enabled a new approach for characterizing the relative contributions of phonons with different mean free paths to total heat conduction [217].

In particular, it gave access to the small-MFP region below $\approx$ 300 nm which has been previously inaccessible to experiment. This unique capability is important as the need for precise knowledge of phonon MFP distributions in complex nanostructures becomes more pressing – for both fundamental understanding and to harness systems where modeling does not yet exist.

- The development and application of EUV nanometrology to a broad range of stiff and soft ultrathin films, with thickness as small as 50 nm, was demonstrated. In particular, the selective layer sensitivity of the short-wavelength surface acoustic waves observable with EUV probes was shown to isolate thin film properties from those of the substrate [34, 35]. Improvements in measurement precision were obtained through use of the chirp z-transform (rather than the Fourier transform) to extract the acoustic oscillation frequencies observed. I also demonstrated the feasibility of extending these techniques to anisotropic materials.

- In extending EUV nanometrology to nanostructured bilayers with metallic layers below 10 nm in thickness, this work showed how the individual layer mechanical properties within the bilayer can be assessed. It further demonstrated sensitivity to shifts in acoustic resonances corresponding to single-monolayer changes in layer thickness, particularly through the introduction of a second frequency extraction technique employing the Matrix Pencil Method. Moreover, it reported the first application of an EUV-based mass sensor proposed by [179] and revealed that the ratio of material densities within the ultrathin layers of Ni and Ta did not deviate significantly from its bulk counterpart. The elastic properties, on the other hand, were observed to deviate significantly and with opposing trends [217]. These observations represent an important step toward a deeper understanding of how elastic properties of materials build up layer by layer, as well as a demonstration of how EUV nanometrology enables the characterization of mechanical properties within nanostructures.

The outlook is very positive for using coherent short-wavelength light to study nanoscale systems. Since bright soft x-ray high harmonic sources can now reach wavelengths below 1 nm [26], these studies can be extended even further into the deep nano-regime. Moreover, their sensitivity to a wide variety of dynamics, including heat transfer, acoustic waves, magnetic states, surface electronic states, plasmon dynamics and more, creates opportunity for unique studies of many physical properties within a single nanosystem, as well as examination of coupled dynamics and element-specific measurements. nanoelectronics

7.1 Ongoing efforts

By implementing significant updates to our experimental setup, we will soon improve our sensitivity to smaller nanostructures by shortening the EUV propagation distance between the samples and CCD. This will enable the collection of light at wider diffraction angles and allow extensions of all the work discussed in this thesis to even smaller size scales to further explore thermal transport and elastic properties in the deep nano-regime. In particular, the improved sensitivity to smaller grating periods and shorter-wavelength SAWs (with their correspondingly short penetration depths) will improve the study of thinner and softer films where we can systematically examine the effects of thickness on elastic properties and trends in the Poisson's ratio of very soft dielectric materials.

Thickness-dependent elasticity will also be better explored through the use of films grown through atomic-layer deposition techniques. Here the sample thickness is more precisely controlled than in the sputtering deposition process employed in Chap. 6, so that the relationship between resonant frequencies and acoustic velocities and elastic properties will be more precisely determined. The interfaces between materials will also likely be more ideal.

The new setup will also enable a visible-wavelength transient grating system to extend our characterization capabilities for flat surfaces. In the immediate future, this will enable the study of phonon-engineered samples where tall nanostructures coupled to a thin membrane modify the system's phonon dispersion and thus thermal conductivity [129].

Further theoretical developments are also under way, particularly focused on the extension from our existing focus on nanoscale thermal transport from 1D-confined nanowire heat sources to 2D-confined nanodot heat sources and improving understanding of the connections between effective thermal conductivity, effective thermal boundary resistivity, and the fundamental phonon dynamics they seek to capture. Understanding the extension from 1D- to 2D-confined heat sources should also lay a strong foundation for extending to 3D-confined heat sources, like those relevant to nanoparticle-mediated thermal therapies in medicine [45], 3D devices encapsulated by other materials, or controlled thermal annealing through the use of embedded nanoparticles [46, 47].

The first successful demonstrations of combining pump-probe observations of dynamics with coherent diffractive imaging will launch exciting new opportunities to examine localized dynamics, such as the elastic responses of single nanostructures and the heat dissipation away from nanoscale heat sources at all points across the surface nearby.

7.2 Future opportunities

Further opportunities for nanoscience with coherent EUV from high harmonic generation are numerous, and a few have already been discussed in the previous chapters. In particular, dynamic imaging could enable more exploration of complex anisotropic materials or surface defects with its introduction of high-resolution (in both space and time) sensitivity to dynamics. It could also better follow lateral heat flow and thermal transport from arbitrary and non-periodic structures. These studies could also be aided by the development of transient grating (TG) experiments employing VUV or EUV excitation where a uniform surface could be excited at much shorter length scales than ever accessible through visible-light TG.

Improving sensitivity to smaller nanostructures will enable study of more fundamental questions about how elastic properties arise from the interactions between atoms or observations of quantized thermal transport. It will also reveal more detail of phonon mean free path spectra and of the various mechanisms that affect them in nanoscale materials. Combining these studies with

those of magnetic systems could allow the observation of magneto-elastic coupling dynamics where the magnetization of a system can be driven by acoustic waves.

Benefiting from the nanofabrication capabilities that can reliably manufacture nanoscale objects for systematic investigation, these studies will uncover the nanoscale physics that is essential for future technological development and a more fundamental understanding of materials and the dynamics within them.

Bibliography

[1] P. Somavat, V. Namboodiri, et al., "Energy consumption of personal computing including portable communication devices," Journal of Green Engineering, vol. 1, no. 4, pp. 447–475, 2011.

[2] M. P. Mills, "The cloud begins with coal: Big data, big networks, big infrastructure, and big power–an overview of the electricity used by the global digital ecosystem," Digital Power Group, 2013.

[3] UN News Center, "Deputy UN chief calls for urgent action to tackle global sanitation crisis." http://www.un.org/apps/news/story.asp?NewsID=44452&Cr=sanitation&Cr1=#.VQdV7uF58nv, 2013. Online; accessed March 16, 2015.

[4] B. Hayes, "The memristor." http://www.americanscientist.org/issues/id.11871,y.0,no.,content.true,page.1,css.print/issue.aspx. Online; accessed March 16, 2015.

[5] "International technology roadmap for semiconductors." http://www.itrs.net/ITRS%201999-2014%20Mtgs,%20Presentations%20&%20Links/2013ITRS/Summary2013.htm, 2014. Online; accessed March 16, 2015.

[6] S. K. King, H. Simka, D. Herr, H. Akinaga, and M. Garner, "Research Updates: The three M's (materials, metrology, and modeling) together pave the path to future nanoelectronic technologies," Applied Physics Letters Materials, vol. 1, p. 040701, 2013.

[7] E. Vogel, "Technology and metrology of new electronic materials and devices," Nature Nanotechnology, vol. 2, no. 1, pp. 25–32, 2007.

[8] H. E. Winlock, "The origin of the ancient Egyptian calendar," Proceedings of the American Philosophical Society, pp. 447–464, 1940.

[9] B. E. Schaefer, "Heliacal rise phenomena," Journal for the History of Astronomy Supplement, vol. 18, p. 19, 1987.

[10] M. A. Lombard, "Fundamentals of time and frequency," The Mechatronics Handbook, 2-Volume Set, 2002.

[11] A. H. Zewail, "Femtochemistry: Atomic-scale dynamics of the chemical bond using ultrafast lasers (Nobel lecture)," Angewandte Chemie International Edition, vol. 39, no. 15, pp. 2586–2631, 2000.

[12] N. Bloembergen, "From nanosecond to femtosecond science," Reviews of Modern Physics, vol. 71, no. 2, p. S283, 1999.

[13] S. Koke, C. Grebing, H. Frei, A. Anderson, A. Assion, and G. Steinmeyer, "Direct frequency comb synthesis with arbitrary offset and shot-noise-limited phase noise," Nature Photonics, vol. 4, no. 7, pp. 462–465, 2010.

[14] The Edgerton Digital Collections Project, "Harold 'Doc' Edgerton." `http://edgerton-digital-collections.org/`, 2015. Online; accessed March 8, 2015.

[15] G. J. Whitrow, Time in history: Views of time from prehistory to the present day. Oxford University Press, 1989.

[16] "A walk through time." `http://www.nist.gov/pml/general/time/index.cfm`, 2010. Online; accessed March 8, 2015.

[17] B. Bloom, T. Nicholson, J. Williams, S. Campbell, M. Bishof, X. Zhang, W. Zhang, S. Bromley, and J. Ye, "An optical lattice clock with accuracy and stability at the 10^{-18} level," Nature, vol. 506, no. 7486, pp. 71–75, 2014.

[18] "A horse's motion scientifically determined," Scientific American, vol. 39, p. 241, 1878.

[19] National Museum of American History, "Freeze frame: Eadweard Muybridge's photography of motion." `http://americanhistory.si.edu/muybridge/htm/htm_sec1/sec1p3.htm`, 2001. Online; accessed March 8, 2015.

[20] T. Maiman, "Stimulated optical radiation in ruby," Nature, vol. 187, pp. 493–494, 1960.

[21] E. Marey, "Photographs of a tumbling cat," Nature, vol. 51, no. 1308, pp. 80–81, 1894.

[22] J. Terrien, "News from the Bureau International des Poids et Mesures," Metrologia, vol. 11, no. 4, pp. 179–183, 1975.

[23] A. Rundquist, C. G. Durfee, Z. Chang, C. Herne, S. Backus, M. M. Murnane, and H. C. Kapteyn, "Phase-matched generation of coherent soft x-rays," Science, vol. 280, no. 5368, pp. 1412–1415, 1998.

[24] E. Goulielmakis, M. Schultze, M. Hofstetter, V. S. Yakovlev, J. Gagnon, M. Uiberacker, A. L. Aquila, E. Gullikson, D. T. Attwood, R. Kienberger, et al., "Single-cycle nonlinear optics," Science, vol. 320, no. 5883, pp. 1614–1617, 2008.

[25] I. P. Christov, M. M. Murnane, and H. C. Kapteyn, "High-harmonic generation of attosecond pulses in the single-cycle regime," Physical Review Letters, vol. 78, no. 7, p. 1251, 1997.

[26] T. Popmintchev, M.-C. Chen, D. Popmintchev, P. Arpin, S. Brown, S. Ališauskas, G. Andriukaitis, T. Balčiunas, O. D. Mücke, A. Pugzlys, et al., "Bright coherent ultrahigh harmonics in the keV x-ray regime from mid-infrared femtosecond lasers," Science, vol. 336, no. 6086, pp. 1287–1291, 2012.

[27] P. Corkum, "Plasma perspective on strong field multiphoton ionization," Physical Review Letters, vol. 71, pp. 1994–1997, 1993.

[28] M. Lewenstein, P. Balcou, M. Y. Ivanov, A. Lhuillier, and P. B. Corkum, "Theory of high-harmonic generation by low-frequency laser fields," Physical Review A, vol. 49, no. 3, p. 2117, 1994.

[29] R. Sandberg, Closing the gap to the diffraction limit: Near wavelength limited tabletop soft x-ray coherent diffractive imaging. PhD thesis, University of Colorado, 2009.

[30] M.-C. Chen, C. Mancuso, C. Hernández-García, F. Dollar, B. Galloway, D. Popmintchev, P.-C. Huang, B. Walker, L. Plaja, A. A. Jaroń-Becker, et al., "Generation of bright isolated attosecond soft x-ray pulses driven by multicycle midinfrared lasers," Proceedings of the National Academy of Sciences, vol. 111, no. 23, pp. E2361–E2367, 2014.

[31] E. Hecht, Optics 4th Edition. Addison Wesley, 2002.

[32] J. Goodman, Introduction to Fourier optics. Roberts & Company Publishers, 2005.

[33] J. Robillard, A. Devos, I. Roch-Jeune, and P. Mante, "Collective acoustic modes in various two-dimensional crystals by ultrafast acoustics: Theory and experiment," Physical Review B, vol. 78, no. 6, p. 064302, 2008.

[34] Q. Li, K. Hoogeboom-Pot, D. Nardi, C. Deeb, S. King, M. Tripp, E. Anderson, M. Murnane, and H. Kapteyn, "Characterization of ultrathin films by laser-induced sub-picosecond photoacoustics with coherent extreme ultraviolet detection," in Proceedings of SPIE, vol. 8324, p. 83241P, 2012.

[35] D. Nardi, K. M. Hoogeboom-Pot, J. N. Hernandez-Charpak, M. Tripp, S. W. King, E. H. Anderson, M. M. Murnane, and H. C. Kapteyn, "Probing limits of acoustic nanometrology using coherent extreme ultraviolet light," in Proc. SPIE Advanced Lithography, p. 86810N, International Society for Optics and Photonics, 2013.

[36] O. Käding, H. Skurk, A. Maznev, and E. Matthias, "Transient thermal gratings at surfaces for thermal characterization of bulk materials and thin films," Applied Physics A, vol. 61, no. 3, pp. 253–261, 1995.

[37] J. A. Johnson, A. Maznev, J. Cuffe, J. K. Eliason, A. J. Minnich, T. Kehoe, C. M. S. Torres, G. Chen, and K. A. Nelson, "Direct measurement of room-temperature nondiffusive thermal transport over micron distances in a silicon membrane," Physical Review Letters, vol. 110, no. 2, p. 025901, 2013.

[38] S. Mathias, J. M. Shaw, E. Turgut, P. Grychtol, R. Adam, D. Rudolf, H. T. Nembach, T. J. Silva, M. Aeschlimann, C. M. Schneider, et al., "Ultrafast element-specific magnetization dynamics of complex magnetic materials on a table-top," Journal of Electron Spectroscopy and Related Phenomena, vol. 189, pp. 164–170, 2013.

[39] T. Saito, O. Matsuda, and O. Wright, "Picosecond acoustic phonon pulse generation in nickel and chromium," Physical Review B, vol. 67, no. 20, p. 205421, 2003.

[40] R. Tobey, M. Siemens, O. Cohen, M. Murnane, H. Kapteyn, and K. Nelson, "Ultrafast extreme ultraviolet holography: dynamic monitoring of surface deformation," Optics Letters, vol. 32, no. 3, pp. 286–288, 2007.

[41] Q. Li, K. Hoogeboom-Pot, D. Nardi, M. Murnane, H. Kapteyn, M. Siemens, E. Anderson, O. Hellwig, E. Dobisz, B. Gurney, et al., "Generation and control of ultrashort-wavelength two-dimensional surface acoustic waves at nanoscale interfaces," Physical Review B, vol. 85, p. 195431, 2012.

[42] G. Chen, "Nanoscale heat transfer and nanostructured thermoelectrics," Components and Packaging Technologies, IEEE Transactions on, vol. 29, no. 2, pp. 238–246, 2006.

[43] C. Dames and G. Chen, "Thermal conductivity of nanostructured thermoelectric materials," Thermoelectrics Handbook: macro to nano, 2006.

[44] L. Shi, "Thermal and thermoelectric transport in nanostructures and low-dimensional systems," Nanoscale and Microscale Thermophysical Engineering, vol. 16, no. 2, pp. 79–116, 2012.

[45] P. K. Jain, X. Huang, I. H. El-Sayed, and M. A. El-Sayed, "Noble metals on the nanoscale: optical and photothermal properties and some applications in imaging, sensing, biology, and medicine," Accounts of Chemical Research, vol. 41, no. 12, pp. 1578–1586, 2008.

[46] S. Maity, J. R. Bochinski, and L. I. Clarke, "Metal nanoparticles acting as light-activated heating elements within composite materials," Advanced Functional Materials, vol. 22, no. 24, pp. 5259–5270, 2012.

[47] V. Viswanath, S. Maity, J. R. Bochinski, L. I. Clarke, and R. E. Gorga, "Thermal annealing of polymer nanocomposites via photothermal heating: Effects on crystallinity and spherulite morphology," Macromolecules, vol. 46, no. 21, pp. 8596–8607, 2013.

[48] E. Pop and K. Goodson, "Thermal phenomena in nanoscale transistors," Journal of Electronic Packaging, vol. 128, p. 102, 2006.

[49] E. Pop, "Energy dissipation and transport in nanoscale devices," Nano Research, vol. 3, no. 3, pp. 147–169, 2010.

[50] A. Balandin, "Nanoscale thermal management," Potentials, IEEE, vol. 21, no. 1, pp. 11–15, 2002.

[51] L. Pan and D. B. Bogy, "Data storage: Heat-assisted magnetic recording," Nature Photonics, vol. 3, no. 4, pp. 189–190, 2009.

[52] M. Siemens, Q. Li, R. Yang, K. Nelson, E. Anderson, M. Murnane, and H. Kapteyn, "Quasi-ballistic thermal transport from nanoscale interfaces observed using ultrafast coherent soft x-ray beams," Nature Materials, vol. 9, no. 1, pp. 26–30, 2010.

[53] K. T. Regner, D. P. Sellan, Z. Su, C. H. Amon, A. J. McGaughey, and J. A. Malen, "Broadband phonon mean free path contributions to thermal conductivity measured using frequency domain thermoreflectance," Nature Communications, vol. 4, p. 1640, 2013.

[54] A. Minnich, J. Johnson, A. Schmidt, K. Esfarjani, M. Dresselhaus, K. Nelson, and G. Chen, "Thermal conductivity spectroscopy technique to measure phonon mean free paths," Physical Review Letters, vol. 107, no. 9, p. 095901, 2011.

[55] Y. K. Koh and D. G. Cahill, "Frequency dependence of the thermal conductivity of semiconductor alloys," Physical Review B, vol. 76, no. 7, p. 075207, 2007.

[56] J. P. Freedman, J. H. Leach, E. A. Preble, Z. Sitar, R. F. Davis, and J. A. Malen, "Universal phonon mean free path spectra in crystalline semiconductors at high temperature," Scientific Reports, vol. 3, 2013.

[57] I. Maasilta and A. J. Minnich, "Heat under the microscope," Physics Today, vol. 67, no. 8, p. 27, 2014.

[58] K. Hoogeboom-Pot, J. N. Hernandez-Charpak, E. Anderson, X. Gu, R. Yang, H. Kapteyn, M. Murnane, and D. Nardi, "A new regime of nanoscale thermal transport: Collective diffusion counteracts dissipation inefficiency," in Ultrafast Phenomena XIX: Proceedings of the 19th International Conference, Okinawa Convention Center, Okinawa, Japan, July 7-11, 2014 (K. Yamanouchi, S. Cundiff, R. de Vivie-Riedle, M. Kuwata-Gonokami, and L. DiMauro, eds.), (Switzerland), pp. 341–344, Springer International Publishing, 2015.

[59] K. M. Hoogeboom-Pot, J. N. Hernandez-Charpak, X. Gu, T. D. Frazer, E. H. Anderson, W. Chao, R. W. Falcone, R. Yang, M. M. Murnane, H. C. Kapteyn, and D. Nardi, "A new regime of nanoscale thermal transport: collective diffusion increases dissipation efficiency," Proceedings of the National Academy of Sciences, vol. 112, no. 16, pp. 4846–4851, 2015. doi:10.1073/pnas.1503449112.

[60] E. Pop, S. Sinha, and K. Goodson, "Heat generation and transport in nanometer-scale transistors," Proceedings of IEEE, vol. 94, no. 8, pp. 1587–1601, 2006.

[61] K. Esfarjani, G. Chen, and H. T. Stokes, "Heat transport in silicon from first-principles calculations," Physical Review B, vol. 84, no. 8, p. 085204, 2011.

[62] A. J. Minnich, G. Chen, S. Mansoor, and B. Yilbas, "Quasiballistic heat transfer studied using the frequency-dependent Boltzmann transport equation," Physical Review B, vol. 84, no. 23, p. 235207, 2011.

[63] G. Mahan and F. Claro, "Nonlocal theory of thermal conductivity," Physical Review B, vol. 38, no. 3, p. 1963, 1988.

[64] G. Chen, "Nonlocal and nonequilibrium heat conduction in the vicinity of nanoparticles," Journal of Heat Transfer, vol. 118, p. 539, 1996.

[65] A. Minnich, "Advances in the measurement and computation of thermal phonon transport properties," Journal of Physics: Condensed Matter, vol. 27, no. 5, p. 053202, 2015.

[66] S. Narumanchi, J. Murthy, and C. Amon, "Boltzmann transport equation-based thermal modeling approaches for hotspots in microelectronics," Heat and Mass Transfer, vol. 42, no. 6, pp. 478–491, 2006.

[67] A. Maznev, J. Johnson, and K. Nelson, "Onset of nondiffusive phonon transport in transient thermal grating decay," Physical Review B, vol. 84, no. 19, p. 195206, 2011.

[68] K. C. Collins, A. A. Maznev, Z. Tian, K. Esfarjani, K. A. Nelson, and G. Chen, "Non-diffusive relaxation of a transient thermal grating analyzed with the Boltzmann transport equation," Journal of Applied Physics, vol. 114, no. 10, pp. 104302–104302, 2013.

[69] G. Chen, "Ballistic-diffusive heat-conduction equations," Physical Review Letters, vol. 86, no. 11, pp. 2297–2300, 2001.

[70] J.-P. M. Péraud and N. G. Hadjiconstantinou, "Efficient simulation of multidimensional phonon transport using energy-based variance-reduced Monte Carlo formulations," Physical Review B, vol. 84, no. 20, p. 205331, 2011.

[71] K. Kukita, I. N. Adisusilo, and Y. Kamakura, "Monte Carlo simulation of diffusive-to-ballistic transition in phonon transport," Journal of Computational Electronics, pp. 1–7, 2013.

[72] D. Cahill, W. Ford, K. Goodson, G. Mahan, A. Majumdar, H. Maris, R. Merlin, and S. Phillpot, "Nanoscale thermal transport," Journal of Applied Physics, vol. 93, p. 793, 2003.

[73] D. G. Cahill, P. V. Braun, G. Chen, D. R. Clarke, S. Fan, K. E. Goodson, P. Keblinski, W. P. King, G. D. Mahan, A. Majumdar, et al., "Nanoscale thermal transport. II. 2003–2012," Applied Physics Reviews, vol. 1, no. 1, p. 011305, 2014.

[74] G. Chen, "Thermal conductivity and ballistic-phonon transport in the cross-plane direction of superlattices," Physical Review B, vol. 57, no. 23, p. 14958, 1998.

[75] W. Capinski, H. Maris, T. Ruf, M. Cardona, K. Ploog, and D. Katzer, "Thermal-conductivity measurements of GaAs/AlAs superlattices using a picosecond optical pump-and-probe technique," Physical Review B, vol. 59, no. 12, p. 8105, 1999.

[76] A. Joshi and A. Majumdar, "Transient ballistic and diffusive phonon heat transport in thin films," Journal of Applied Physics, vol. 74, no. 1, pp. 31–39, 1993.

[77] Y. Ju and K. Goodson, "Phonon scattering in silicon films with thickness of order 100 nm," Applied Physics Letters, vol. 74, p. 3005, 1999.

[78] R. Chen, A. I. Hochbaum, P. Murphy, J. Moore, P. Yang, and A. Majumdar, "Thermal conductance of thin silicon nanowires," Physical Review Letters, vol. 101, no. 10, p. 105501, 2008.

[79] J. Lim, K. Hippalgaonkar, S. Andrews, A. Majumdar, and P. Yang, "Quantifying surface roughness effects on phonon transport in silicon nanowires," Nano Letters, 2012.

[80] N. Yang, G. Zhang, and B. Li, "Violation of Fourier's law and anomalous heat diffusion in silicon nanowires," Nano Today, vol. 5, no. 2, pp. 85–90, 2010.

[81] M.-H. Bae, Z. Li, Z. Aksamija, P. N. Martin, F. Xiong, Z.-Y. Ong, I. Knezevic, and E. Pop, "Ballistic to diffusive crossover of heat flow in graphene ribbons," Nature Communications, vol. 4, p. 1734, 2013.

[82] A. L. Moore, S. K. Saha, R. S. Prasher, and L. Shi, "Phonon backscattering and thermal conductivity suppression in sawtooth nanowires," Applied Physics Letters, vol. 93, no. 8, pp. 083112–083112, 2008.

[83] H. Maris and S. Tamura, "Heat flow in nanostructures in the Casimir regime," Physical Review B, vol. 85, no. 5, p. 054304, 2012.

[84] M. Highland, B. Gundrum, Y. Koh, R. Averback, D. Cahill, V. Elarde, J. Coleman, D. Walko, and E. Landahl, "Ballistic-phonon heat conduction at the nanoscale as revealed by time-resolved x-ray diffraction and time-domain thermoreflectance," Physical Review B, vol. 76, no. 7, p. 075337, 2007.

[85] J. A. Johnson, A. A. Maznev, M. T. Bulsara, E. A. Fitzgerald, T. Harman, S. Calawa, C. Vineis, G. Turner, and K. A. Nelson, "Phase-controlled, heterodyne laser-induced transient grating measurements of thermal transport properties in opaque material," Journal of Applied Physics, vol. 111, no. 2, pp. 023503–023503, 2012.

[86] A. Minnich and G. Chen, "Quasi-ballistic heat transfer from metal nanostructures on sapphire," in Proc. of ASME, 2011.

[87] T. Oyake, M. Sakata, and J. Shiomi, "Nanoscale thermal conductivity spectroscopy by using gold nano-islands heat absorbers," Applied Physics Letters, vol. 106, no. 7, p. 073102, 2015.

[88] F. Yang and C. Dames, "Mean free path spectra as a tool to understand thermal conductivity in bulk and nanostructures," Physical Review B, vol. 87, no. 3, p. 035437, 2013.

[89] K. Regner, A. McGaughey, and J. Malen, "Analytical interpretation of nondiffusive phonon transport in thermoreflectance thermal conductivity measurements," Physical Review B, vol. 90, no. 6, p. 064302, 2014.

[90] R. Wilson and D. G. Cahill, "Anisotropic failure of Fourier theory in time-domain thermoreflectance experiments," Nature Communications, vol. 5, 2014.

[91] J. Maassen and M. Lundstrom, "Steady-state heat transport: Ballistic-to-diffusive with Fourier's law," Journal of Applied Physics, vol. 117, no. 3, p. 035104, 2015.

[92] D. Nardi, M. Travagliati, M. E. Siemens, Q. Li, M. M. Murnane, H. C. Kapteyn, G. Ferrini, F. Parmigiani, and F. Banfi, "Probing thermomechanics at the nanoscale: Impulsively excited pseudosurface acoustic waves in hypersonic phononic crystals," Nano Letters, vol. 11, no. 10, pp. 4126–4133, 2011.

[93] T. M. Atanackovic and A. Guran, Theory of elasticity for scientists and engineers. Springer Science & Business Media, 2000.

[94] F. Banfi, F. Pressacco, B. Revaz, C. Giannetti, D. Nardi, G. Ferrini, and F. Parmigiani, "Ab initio thermodynamics calculation of all-optical time-resolved calorimetry of nanosize systems: Evidence of nanosecond decoupling of electron and phonon temperatures," Physical Review B, vol. 81, no. 15, p. 155426, 2010.

[95] Z. Lin and L. V. Zhigilei, "Temperature dependences of the electron–phonon coupling, electron heat capacity and thermal conductivity in ni under femtosecond laser irradiation," Applied Surface Science, vol. 253, no. 15, pp. 6295–6300, 2007.

[96] P. D. Desai, "Thermodynamic properties of iron and silicon," Journal of Physical and Chemical Reference Data, vol. 15, no. 3, pp. 967–983, 1986.

[97] J. A. Dean, Lange's Handbook of Chemistry. McGraw Hill Book Co., New York, NY, 1985.

[98] C. Kittel, Introduction to Solid State Physics, vol. 7. John Wiley & Sons, 1996.

[99] J. Zacharias, "The temperature dependence of Young's modulus for nickel," Physical Review, vol. 44, no. 2, p. 116, 1933.

[100] J. Wortman and R. Evans, "Young's modulus, shear modulus, and Poisson's ratio in silicon and germanium," Journal of Applied Physics, vol. 36, no. 1, pp. 153–156, 1965.

[101] J. Wachtman Jr, W. Tefft, D. Lam Jr, and C. Apstein, "Exponential temperature dependence of Young's modulus for several oxides," Physical Review, vol. 122, no. 6, p. 1754, 1961.

[102] Y. Okada and Y. Tokumaru, "Precise determination of lattice parameter and thermal expansion coefficient of silicon between 300 and 1500 K," Journal of Applied Physics, vol. 56, no. 2, pp. 314–320, 1984.

[103] M. J. Weber, Handbook of optical materials. CRC Press LLC, 2003.

[104] R. Tobey, E. Gershgoren, M. Siemens, M. Murnane, H. Kapteyn, T. Feurer, and K. Nelson, "Nanoscale photothermal and photoacoustic transients probed with extreme ultraviolet radiation," Applied Physics Letters, vol. 85, p. 564, 2004.

[105] J. T. Verdeyen, Laser Electronics, Third Edition. Prentice-Hall, Inc., Englewood Cliffs, NJ, 1995.

[106] G. Chen, D. Borca-Tasciuc, and R. Yang, "Nanoscale heat transfer," Encyclopedia of Nanoscience and Nanotechnology, vol. 7, pp. 429–459, 2004.

[107] G. Wexler, "The size effect and the non-local Boltzmann transport equation in orifice and disk geometry," Proceedings of the Physical Society, vol. 89, no. 4, pp. 927–941, 1966.

[108] R. Prasher, "Predicting the thermal resistance of nanosized constrictions," Nano Letters, vol. 5, no. 11, pp. 2155–2159, 2005.

[109] G. Romano and J. C. Grossman, "Toward phonon-boundary engineering in nanoporous materials," Applied Physics Letters, vol. 105, no. 3, p. 033116, 2014.

[110] A. Minnich, "Determining phonon mean free paths from observations of quasiballistic thermal transport," Physical Review Letters, vol. 109, no. 20, p. 205901, 2012.

[111] D. Ding, X. Chen, and A. Minnich, "Radial quasiballistic transport in time-domain thermoreflectance studied using monte carlo simulations," Applied Physics Letters, vol. 104, no. 14, p. 143104, 2014.

[112] A. S. Henry and G. Chen, "Spectral phonon transport properties of silicon based on molecular dynamics simulations and lattice dynamics," Journal of Computational and Theoretical Nanoscience, vol. 5, no. 2, pp. 141–152, 2008.

[113] L. Zeng and G. Chen, "Disparate quasiballistic heat conduction regimes from periodic heat sources on a substrate," Journal of Applied Physics, vol. 116, no. 6, p. 064307, 2014.

[114] K. Schwab, E. Henriksen, J. Worlock, and M. L. Roukes, "Measurement of the quantum of thermal conductance," Nature, vol. 404, no. 6781, pp. 974–977, 2000.

[115] M. D. Seaberg, D. E. Adams, E. L. Townsend, D. A. Raymondson, W. F. Schlotter, Y. Liu, C. S. Menoni, L. Rong, C.-C. Chen, J. Miao, et al., "Ultrahigh 22 nm resolution coherent diffractive imaging using a desktop 13 nm high harmonic source," Optics Express, vol. 19, no. 23, pp. 22470–22479, 2011.

[116] B. Zhang, M. D. Seaberg, D. E. Adams, D. F. Gardner, E. R. Shanblatt, J. M. Shaw, W. Chao, E. M. Gullikson, F. Salmassi, H. C. Kapteyn, et al., "Full field tabletop EUV coherent diffractive imaging in a transmission geometry," Optics Express, vol. 21, no. 19, pp. 21970–21980, 2013.

[117] D. F. Gardner, B. Zhang, M. D. Seaberg, L. S. Martin, D. E. Adams, F. Salmassi, E. Gullikson, H. Kapteyn, and M. Murnane, "High numerical aperture reflection mode coherent diffraction microscopy using off-axis apertured illumination," Optics Express, vol. 20, no. 17, pp. 19050–19059, 2012.

[118] M. D. Seaberg, B. Zhang, D. F. Gardner, E. R. Shanblatt, M. M. Murnane, H. C. Kapteyn, and D. E. Adams, "Tabletop nanometer extreme ultraviolet imaging in an extended reflection mode using coherent Fresnel ptychography," Optica, vol. 1, no. 1, pp. 39–44, 2014.

[119] R. Metzler and J. Klafter, "The random walk's guide to anomalous diffusion: a fractional dynamics approach," Physics Reports, vol. 339, no. 1, pp. 1–77, 2000.

[120] S. Liu, X. Xu, R. Xie, G. Zhang, and B. Li, "Anomalous heat conduction and anomalous diffusion in low dimensional nanoscale systems," The European Physical Journal B-Condensed Matter and Complex Systems, vol. 85, no. 10, pp. 1–20, 2012.

[121] S. Liu, P. Hänggi, N. Li, J. Ren, and B. Li, "Anomalous heat diffusion," Physical Review Letters, vol. 112, no. 4, p. 040601, 2014.

[122] B. Vermeersch, A. M. Mohammed, G. Pernot, Y. R. Koh, and A. Shakouri, "Thermal interfacial transport in the presence of ballistic heat modes," Physical Review B, vol. 90, no. 1, p. 014306, 2014.

[123] B. Vermeersch, A. Mohammed, G. Pernot, Y. R. Koh, and A. Shakouri, "Superdiffusive heat conduction in semiconductor alloys—II. truncated Lévy formalism for experimental analysis," Physical Review B, vol. 91, no. 8, p. 085203, 2015.

[124] A. Dhar, K. Saito, and B. Derrida, "Exact solution of a Lévy walk model for anomalous heat transport," Physical Review E, vol. 87, no. 1, p. 010103, 2013.

[125] Y. Ma, "A two-parameter nondiffusive heat conduction model for data analysis in pump-probe experiments," Journal of Applied Physics, vol. 116, no. 24, p. 243505, 2014.

[126] J. Cuffe, J. K. Eliason, A. A. Maznev, K. C. Collins, J. A. Johnson, A. Shchepetov, M. Prunnila, J. Ahopelto, C. M. S. Torres, G. Chen, et al., "Reconstructing phonon mean free path contributions to thermal conductivity using nanoscale membranes," arXiv preprint arXiv:1408.6747, 2014.

[127] S. Simons, "The application of high frequency thermal propagation data to the measurement of phonon relaxation times," Journal of Physics C: Solid State Physics, vol. 4, no. 14, p. 2089, 1971.

[128] K. Regner, S. Majumdar, and J. Malen, "Instrumentation of broadband frequency domain thermoreflectance for measuring thermal conductivity accumulation functions," Review of Scientific Instruments, vol. 84, no. 6, p. 064901, 2013.

[129] B. L. Davis and M. I. Hussein, "Nanophononic metamaterial: Thermal conductivity reduction by local resonance," Physical Review Letter, vol. 112, p. 055505, Feb 2014.

[130] D. Aketo, T. Shiga, and J. Shiomi, "Scaling laws of cumulative thermal conductivity for short and long phonon mean free paths," Applied Physics Letters, vol. 105, no. 13, p. 131901, 2014.

[131] A. Ward and D. Broido, "Intrinsic phonon relaxation times from first-principles studies of the thermal conductivities of Si and Ge," Physical Review B, vol. 81, no. 8, p. 085205, 2010.

[132] J. Hernandez-Charpak, K. Hoogeboom-Pot, E. Anderson, M. Murnane, H. Kapteyn, and D. Nardi, "Comparing the transition from diffusive to ballistic heat transport for 1d and 2d nanoscale interfaces," Bulletin of the American Physical Society, vol. 59, 2014.

[133] R. Yang, G. Chen, M. Laroche, and Y. Taur, "Simulation of nanoscale multidimensional transient heat conduction problems using ballistic-diffusive equations and phonon Boltzmann equation," Journal of Heat Transfer, vol. 127, no. 3, pp. 298–306, 2005.

[134] M. Alam, R. Pulavarthy, J. Bielefeld, S. King, and M. Haque, "Thermal conductivity measurement of low-k dielectric films: Effect of porosity and density," Journal of Electronic Materials, pp. 1–9, 2014.

[135] C. Hu, M. Morgen, P. S. Ho, A. Jain, W. N. Gill, J. L. Plawsky, and P. C. Wayner Jr, "Thermal conductivity study of porous low-k dielectric materials," Applied Physics Letters, vol. 77, no. 1, pp. 145–147, 2000.

[136] J.-S. Heron, C. Bera, T. Fournier, N. Mingo, and O. Bourgeois, "Blocking phonons via nanoscale geometrical design," Physical Review B, vol. 82, no. 15, p. 155458, 2010.

[137] J.-K. Yu, S. Mitrovic, D. Tham, J. Varghese, and J. R. Heath, "Reduction of thermal conductivity in phononic nanomesh structures," Nature Nanotechnology, vol. 5, no. 10, pp. 718–721, 2010.

[138] S. W. King, J. Bielefeld, G. Xu, W. A. Lanford, Y. Matsuda, R. H. Dauskardt, N. Kim, D. Hondongwa, L. Olasov, B. Daly, et al., "Influence of network bond percolation on the thermal, mechanical, electrical and optical properties of high and low-k a-SiC:H thin films," Journal of Non-Crystalline Solids, vol. 379, pp. 67–79, 2013.

[139] "Property information: Young's modulus and specific stiffness." `http://www-materials.eng.cam.ac.uk/mpsite/properties/non-IE/stiffness.html`. Online; accessed March 12, 2015.

[140] G. Greaves, A. Greer, R. Lakes, and T. Rouxel, "Poisson's ratio and modern materials," Nature Materials, vol. 10, no. 11, pp. 823–837, 2011.

[141] "Poisson's ratio at 200," Nature Materials, vol. 10, p. 807, November 2011.

[142] J. Hay and B. Crawford, "Measuring substrate-independent modulus of thin films," Journal of Materials Research, vol. 26, no. 06, pp. 727–738, 2011.

[143] B. Zhou and B. Prorok, "A new paradigm in thin film indentation," Journal of Materials Research, vol. 25, no. 9, p. 1671, 2010.

[144] H. Li, N. Randall, and J. Vlassak, "New methods of analyzing indentation experiments on very thin films," Journal of Materials Research, vol. 25, no. 4, p. 728, 2010.

[145] J. P. Killgore and D. C. Hurley, "Low-force AFM nanomechanics with higher-eigenmode contact resonance spectroscopy," Nanotechnology, vol. 23, no. 5, p. 055702, 2012.

[146] S. King, G. A. Antonelli, G. Stan, R. F. Cook, and R. Sooryakumar, "Advances in metrology for the determination of Young's modulus for low-k dielectric thin films," in Proc. SPIE Instrumentation, Metrology, and Standards for Nanomanufacturing, Optics, and Semiconductors VI, vol. 8466, p. 84660A, International Society for Optics and Photonics, 2012.

[147] M. Kopycinska-Müller, R. Geiss, J. Müller, and D. Hurley, "Elastic-property measurements of ultrathin films using atomic force acoustic microscopy," Nanotechnology, vol. 16, no. 6, p. 703, 2005.

[148] D. Hurley, M. Kopycinska-Müller, and A. Kos, "Mapping mechanical properties on the nanoscale using atomic-force acoustic microscopy," JOM, vol. 59, no. 1, pp. 23–29, 2007.

[149] M. Kopycinska-Müller, A. Striegler, A. Hürrich, B. Köhler, N. Meyendorf, and K. Wolter, "Elastic properties of nano-thin films by use of atomic force acoustic microscopy," in MRS Proceedings, vol. 1185, Cambridge Univ Press, 2009.

[150] M. Beghi, C. Bottani, and R. Pastorelli, "High accuracy measurement of elastic constants of thin films by surface Brillouin scattering," Mechanical Properties of Structural Films, vol. 1413, pp. 109–126, 2001.

[151] A. Link, R. Sooryakumar, R. Bandhu, and G. Antonelli, "Brillouin light scattering studies of the mechanical properties of ultrathin low-k dielectric films," Journal of Applied Physics, vol. 100, p. 013507, 2006.

[152] M. Beghi, F. Di Fonzo, S. Pietralunga, C. Ubaldi, and C. Bottani, "Precision and accuracy in film stiffness measurement by Brillouin spectroscopy," Review of Scientific Instruments, vol. 82, no. 5, pp. 053107–053107, 2011.

[153] J. Cuffe, E. Chavez, A. Shchepetov, P.-O. Chapuis, E. H. El Boudouti, F. Alzina, T. Kehoe, J. Gomis-Bresco, D. Dudek, Y. Pennec, et al., "Phonons in slow motion: dispersion relations in ultrathin Si membranes," Nano Letters, vol. 12, no. 7, pp. 3569–3573, 2012.

[154] C. Thomsen, H. Grahn, H. Maris, and J. Tauc, "Surface generation and detection of phonons by picosecond light pulses," Physical Review B, vol. 34, no. 6, p. 4129, 1986.

[155] H. Grahn, H. Maris, and J. Tauc, "Picosecond ultrasonics," Quantum Electronics, IEEE Journal of, vol. 25, no. 12, pp. 2562–2569, 1989.

[156] H. Ogi, N. Nakamura, and M. Hirao, "Picosecond ultrasound spectroscopy for studying elastic modulus of thin films: a review," Nondestructive Testing and Evaluation, vol. 26, no. 3-4, pp. 267–280, 2011.

[157] D. Schneider, T. Witke, T. Schwarz, B. Schöneich, and B. Schultrich, "Testing ultra-thin films by laser-acoustics," Surface and Coatings Technology, vol. 126, no. 2-3, pp. 136–141, 2000.

[158] T. Lee, K. Ohmori, C.-S. Shin, D. G. Cahill, I. Petrov, and J. Greene, "Elastic constants of single-crystal $TiN_x(001)(0.67 \leq x \leq 1.0)$ determined as a function of x by picosecond ultrasonic measurements," Physical Review B, vol. 71, no. 14, p. 144106, 2005.

[159] C. Giannetti, B. Revaz, F. Banfi, M. Montagnese, G. Ferrini, F. Cilento, S. Maccalli, P. Vavassori, G. Oliviero, E. Bontempi, et al., "Thermomechanical behavior of surface acoustic waves in ordered arrays of nanodisks studied by near-infrared pump-probe diffraction experiments," Physical Review B, vol. 76, no. 12, p. 125413, 2007.

[160] P. Mante, A. Devos, and J. Robillard, "Towards thin film complete characterization using picosecond ultrasonics," in Ultrasonics Symposium, 2008. IUS 2008. IEEE, pp. 1203–1206, IEEE, 2008.

[161] D. Nardi, F. Banfi, C. Giannetti, B. Revaz, G. Ferrini, and F. Parmigiani, "Pseudosurface acoustic waves in hypersonic surface phononic crystals," Physical Review B, vol. 80, no. 10, p. 104119, 2009.

[162] A. Duggal, J. Rogers, and K. Nelson, "Real-time optical characterization of surface acoustic modes of polyimide thin-film coatings," Journal of Applied Physics, vol. 72, no. 7, pp. 2823–2839, 1992.

[163] T. Crimmins, A. Maznev, and K. Nelson, "Transient grating measurements of picosecond acoustic pulses in metal films," Applied Physics Letters, vol. 74, p. 1344, 1999.

[164] R. Tobey, M. Siemens, M. Murnane, H. Kapteyn, D. Torchinsky, and K. Nelson, "Transient grating measurement of surface acoustic waves in thin metal films with extreme ultraviolet radiation," Applied Physics Letters, vol. 89, p. 091108, 2006.

[165] A. Bartels, R. Cerna, C. Kistner, A. Thoma, F. Hudert, C. Janke, and T. Dekorsy, "Ultrafast time-domain spectroscopy based on high-speed asynchronous optical sampling," Review of Scientific Instruments, vol. 78, no. 3, p. 035107, 2007.

[166] A. Devos, S. Sadtler, P.-A. Mante, A. Le Louarn, and P. Emery, "Pushing the limits of acoustics at the nanoscale using femtosecond transient interferometry," Applied Physics Letters, vol. 105, p. 231905, 2014.

[167] A. I. Fedorchenko, A.-B. Wang, and H. H. Cheng, "Thickness dependence of nanofilm elastic modulus," Applied Physics Letters, vol. 94, no. 15, p. 152111, 2009.

[168] B. Gong, Q. Chen, and D. Wang, "Molecular dynamics study on size-dependent elastic properties of silicon nanoplates," Materials Letters, vol. 67, no. 1, pp. 165–168, 2012.

[169] S. King, J. Bielefeld, M. French, and W. Lanford, "Mass and bond density measurements for PECVD a-SiC_x:h thin films using Fourier transform-infrared spectroscopy," Journal of Non-Crystalline Solids, 2011.

[170] L. Rabiner, R. Schafer, and C. Rader, "The chirp z-transform algorithm," Audio and Electroacoustics, IEEE Transactions on, vol. 17, no. 2, pp. 86–92, 1969.

[171] H. Coufal, K. Meyer, R. Grygier, P. Hess, and A. Neubrand, "Precision measurement of the surface acoustic wave velocity on silicon single crystals using optical excitation and detection," The Journal of the Acoustical Society of America, vol. 95, p. 1158, 1994.

[172] L. D. Landau and E. M. Lifshitz, "Theory of elasticity, vol. 7," Course of Theoretical Physics, vol. 2, p. 112, 1975.

[173] H. Lin, H. Maris, L. Freund, K. Lee, H. Luhn, and D. Kern, "Study of vibrational modes of gold nanostructures by picosecond ultrasonics," Journal of Applied Physics, vol. 73, no. 1, pp. 37–45, 1993.

[174] P. Mante, J. Robillard, and A. Devos, "Complete thin film mechanical characterization using picosecond ultrasonics and nanostructured transducers: experimental demonstration on SiO," Applied Physics Letters, vol. 93, p. 071909, 2008.

[175] D. H. Hurley, S. J. Reese, and F. Farzbod, "Application of laser-based resonant ultrasound spectroscopy to study texture in copper," Journal of Applied Physics, vol. 111, no. 5, pp. 053527–053527, 2012.

[176] D. C. Hurley and J. P. Killgore, "Dynamic contact AFM methods for nanomechanical properties," Scanning Probe Microscopy for Industrial Applications: Nanomechanical Characterization, p. 115, 2013.

[177] M. Plodinec, M. Loparic, C. Monnier, E. Obermann, R. Zanetti-Dallenbach, P. Oertle, J. Hyotyla, U. Aebi, M. Bentires-Alj, R. Lim, et al., "The nanomechanical signature of breast cancer," Nature Nanotechnology, vol. 7, no. 11, pp. 757–765, 2012.

[178] D. Rudolf, L.-O. Chan, M. Battiato, R. Adam, J. M. Shaw, E. Turgut, P. Maldonado, S. Mathias, P. Grychtol, H. T. Nembach, et al., "Ultrafast magnetization enhancement in metallic multilayers driven by superdiffusive spin current," Nature Communications, vol. 3, p. 1037, 2012.

[179] D. Nardi, E. Zagato, G. Ferrini, C. Giannetti, and F. Banfi, "Design of a surface acoustic wave mass sensor in the 100 GHz range," Applied Physics Letters, vol. 100, no. 25, pp. 253106–253106, 2012.

[180] W. Yang, T. Tsakalakos, and J. Hilliard, "Enhanced elastic modulus in composition-modulated gold-nickel and copper-palladium foils," Journal of Applied Physics, vol. 48, no. 3, pp. 876–879, 1977.

[181] F. Streitz, R. Cammarata, and K. Sieradzki, "Surface-stress effects on elastic properties. ii. metallic multilayers," Physical Review B, vol. 49, no. 15, p. 10707, 1994.

[182] R. Cammarata and K. Sieradzki, "Effects of surface stress on the elastic moduli of thin films and superlattices," Physical Review Letters, vol. 62, no. 17, p. 2005, 1989.

[183] J. R. Dutcher, S. Lee, J. Kim, G. I. Stegeman, and C. M. Falco, "Enhancement of the c_{11} elastic constant of Ag/Pd superlattice films as determined from longitudinal guided modes," Physical Review Letters, vol. 65, no. 10, p. 1231, 1990.

[184] A. Fartash, E. E. Fullerton, I. K. Schuller, S. E. Bobbin, J. Wagner, R. Cammarata, S. Kumar, and M. Grimsditch, "Evidence for the supermodulus effect and enhanced hardness in metallic superlattices," Physical Review B, vol. 44, no. 24, p. 13760, 1991.

[185] B. M. Clemens and G. L. Eesley, "Relationship between interfacial strain and the elastic response of multilayer metal films," Physical Review Letters, vol. 61, no. 20, p. 2356, 1988.

[186] N. Nakamura, H. Ogi, T. Yasui, M. Fujii, and M. Hirao, "Mechanism of elastic softening behavior in a superlattice," Physical Review Letters, vol. 99, no. 3, p. 035502, 2007.

[187] N. Nakamura, A. Uranishi, M. Wakita, H. Ogi, M. Hirao, and M. Nishiyama, "Elastic stiffness of $l1_0$ FePt thin film studied by picosecond ultrasonics," Applied Physics Letters, vol. 98, no. 10, pp. 101911–101911, 2011.

[188] N. Pu and T. Li, "Pulse-echo measurement of longitudinal sound velocity in nanometer thin films," Applied Physics B, vol. 82, no. 3, pp. 449–453, 2006.

[189] B. Nysten, C. Frétigny, and S. Cuenot, "Elastic modulus of nanomaterials: resonant contact-AFM measurement and reduced-size effects," in Nondestructive Evaulation for Health Monitoring and Diagnostics, pp. 78–88, International Society for Optics and Photonics, 2005.

[190] R. Dingreville, J. Qu, and M. Cherkaoui, "Surface free energy and its effect on the elastic behavior of nano-sized particles, wires and films," Journal of the Mechanics and Physics of Solids, vol. 53, no. 8, pp. 1827–1854, 2005.

[191] M. T. McDowell, A. M. Leach, and K. Gall, "On the elastic modulus of metallic nanowires," Nano Letters, vol. 8, no. 11, pp. 3613–3618, 2008.

[192] H. Sadeghian, C.-K. Yang, J. Goosen, E. Van Der Drift, A. Bossche, P. French, and F. Van Keulen, "Characterizing size-dependent effective elastic modulus of silicon nanocantilevers using electrostatic pull-in instability," Applied Physics Letters, vol. 94, no. 22, pp. 221903–221903, 2009.

[193] P. Zijlstra, A. L. Tchebotareva, J. W. Chon, M. Gu, and M. Orrit, "Acoustic oscillations and elastic moduli of single gold nanorods," Nano Letters, vol. 8, no. 10, pp. 3493–3497, 2008.

[194] V. Juvé, A. Crut, P. Maioli, M. Pellarin, M. Broyer, N. Del Fatti, and F. Vallée, "Probing elasticity at the nanoscale: terahertz acoustic vibration of small metal nanoparticles," Nano Letters, vol. 10, no. 5, pp. 1853–1858, 2010.

[195] C. Rossignol, B. Perrin, B. Bonello, P. Djemia, P. Moch, and H. Hurdequint, "Elastic properties of ultrathin permalloy/alumina multilayer films using picosecond ultrasonics and brillouin light scattering," Physical Review B, vol. 70, no. 9, p. 094102, 2004.

[196] H. Ogi, M. Fujii, N. Nakamura, T. Yasui, and M. Hirao, "Stiffened ultrathin Pt films confirmed by acoustic-phonon resonances," Physical Review Letters, vol. 98, no. 19, p. 195503, 2007.

[197] H. Ogi, M. Fujii, N. Nakamura, T. Shagawa, and M. Hirao, "Resonance acoustic-phonon spectroscopy for studying elasticity of ultrathin films," Applied Physics Letters, vol. 90, no. 19, p. 191906, 2007.

[198] N. Nakamura, A. Uranishi, T. Shagawa, H. Ogi, M. Hirao, and M. Nishiyama, "Laser-induced coherent acoustic phonons for measuring elastic constants of ultra-thin films," Journal of Solid Mechanics and Materials Engineering, vol. 2, no. 11, pp. 1420–1426, 2008.

[199] R. E. Miller and V. B. Shenoy, "Size-dependent elastic properties of nanosized structural elements," Nanotechnology, vol. 11, no. 3, p. 139, 2000.

[200] L. Zhou and H. Huang, "Are surfaces elastically softer or stiffer?," Applied Physics Letters, vol. 84, no. 11, pp. 1940–1942, 2004.

[201] I. Chang, S.-H. Chang, J.-C. Huang, et al., "The theoretical model of fcc ultrathin film," International Journal of Solids and Structures, vol. 44, no. 18, pp. 5818–5828, 2007.

[202] Encyclopedia Brittanica, "tantalum (Ta)." `http://www.britannica.com/EBchecked/topic/582754/tantalum-Ta`, 2015. Online; accessed March 8, 2015.

[203] E. Çetinörgü, B. Baloukas, O. Zabeida, J. E. Klemberg-Sapieha, and L. Martinu, "Mechanical and thermoelastic characteristics of optical thin films deposited by dual ion beam sputtering," Applied Optics, vol. 48, no. 23, pp. 4536–4544, 2009.

[204] Commission on isotopic abundances and atomic weights, "Conventional atomic weights." `http://www.ciaaw.org/pubs/TSAW2013_xls.xls`, 2013. Online; accessed March 8, 2015.

[205] M. T. Kim, "Influence of substrates on the elastic reaction of films for the microindentation tests," Thin Solid Films, vol. 283, no. 1, pp. 12–16, 1996.

[206] B. Halg, "On a nonvolatile memory cell based on micro-electro-mechanics," in Micro Electro Mechanical Systems, 1990. Proceedings, An Investigation of Micro Structures, Sensors, Actuators, Machines and Robots. IEEE, pp. 172–176, IEEE, 1990.

[207] ONDA Corporation, "Acoustic properties of solids." `http://www.ondacorp.com/images/Solids.pdf`, 2011. Online; accessed March 8, 2015.

[208] Y. Hua and T. K. Sarkar, "Matrix pencil method for estimating parameters of exponentially damped/undamped sinusoids in noise," IEEE Transactions on Acoustics, Speech and Signal Processing, vol. 38, no. 5, pp. 814–824, 1990.

[209] T. K. Sarkar and O. Pereira, "Using the matrix pencil method to estimate the parameters of a sum of complex exponentials," Antennas and Propagation Magazine, IEEE, vol. 37, no. 1, pp. 48–55, 1995.

[210] J. E. Fernández del Rıo and T. K. Sarkar, "Comparison between the matrix pencil method and the fourier transform technique for high-resolution spectral estimation," Digital Signal Processing, vol. 6, no. 2, pp. 108–125, 1996.

[211] B. Bonello, B. Perrin, E. Romatet, and J. Jeannet, "Application of the picosecond ultrasonic technique to the study of elastic and time-resolved thermal properties of materials," Ultrasonics, vol. 35, no. 3, pp. 223–231, 1997.

[212] COMSOL, Inc., "COMSOL Multiphysics, Version 4.3b," 2013. version 4.3b.

[213] J. Groenen, F. Poinsotte, A. Zwick, C. S. Torres, M. Prunnila, and J. Ahopelto, "Inelastic light scattering by longitudinal acoustic phonons in thin silicon layers: From membranes to silicon-on-insulator structures," Physical Review B, vol. 77, no. 4, p. 045420, 2008.

[214] V. B. Shenoy, "Atomistic calculations of elastic properties of metallic fcc crystal surfaces," Physical Review B, vol. 71, no. 9, p. 094104, 2005.

[215] J. Karanikas, R. Sooryakumar, and J. M. Phillips, "Dispersion of elastic waves in supported CaF_2 films," Journal of Applied Physics, vol. 65, no. 9, pp. 3407–3410, 1989.

[216] Y.-C. Lee, K. C. Bretz, F. W. Wise, and W. Sachse, "Picosecond acoustic measurements of longitudinal wave velocity of submicron polymer films," Applied Physics Letters, vol. 69, no. 12, pp. 1692–1694, 1996.

[217] K. Hoogeboom-Pot, J. Hernandez-Charpak, T. Frazer, X. Gu, E. Turgut, E. Anderson, W. Chao, J. Shaw, R. Yang, M. Murnane, H. Kapteyn, and D. Nardi, "Mechanical and thermal properties of nanomaterials at sub-50nm dimensions characterized using coherent EUV beams," in Proc. SPIE Advanced Lithography, vol. 9424, International Society of Optics and Photonics, 2015.

Appendix A

MATLAB program for frequency peak-finding using chirp z-transform

This program was used to extract the SAW frequencies for both thin film samples in Chap. 5 and Ni/Ta bilayer samples in Chap. 6. It uses a chirp z-transform to calculate the frequency spectrum of the signal, and then fits the peaks to a Gaussian to extract the central frequency. This procedure generally improved frequency extraction precision by approximately 10× compared with looking to Fourier transform peaks.

```
function freqs = fSAW( dataFile, fMin, fMax, numFreqs, fGuess )

% ========================================================================
% The function unwraps the loops which make up a given data scan,
% separately calculates the chirp z-transform and fits the frequency peaks
% to a Gaussian to extract the central frequencies
%
% Inputs: dataFile = string giving location of data file - a two-column
%           .dat with [time (ps),signal] and time-zero actually at 0 ps
%         fMin, fMax = min and max of frequency range for CZT, in GHz
%         numFreqs = number of frequency peaks to look for (in descending
%           amplitude order)
%         fGuess = frequency in GHz, initial guesses for CZT peak fit
%           ([f1,f2,...], as many as requested by numFreqs)
% Output: freqs = matrix giving the central frequencies
%           of the peaks
% Dependencies: Makes use of versions of chirpZTrans, and
%                 ft_pad functions included in this file
%
% Written by: Kathy Hoogeboom-Pot, 7/3/13
% ========================================================================

% Import data
data = load(dataFile);

% Chirp z-transform of signal and plot
```

```
figure(11);

czt = chirpZTrans(data,fMin,fMax);

% For comparison, look also at Fourier transform (Can
% change second ft_pad input to add zero-padding.)
figure(13); hold on;

ft = ft_pad(data,0);
plot(ft(:,1),ft(:,2),'linewidth',2);


% Fit frequency peaks to find centers

% Initialize output frequency matrix
freqs = zeros(1,numFreqs);

% Find peaks to fit
[pks,pkLocs] = findpeaks(czt(:,2));
[~,trLocs] = findpeaks(-czt(:,2));

peaksMat = [pkLocs,pks];
sortPeaksMat = sortrows(peaksMat,-2);

for idxFreq=1:numFreqs
   % Find bottom on either side of peak to define range for fit
   troughBefore = trLocs(find(trLocs < sortPeaksMat(idxFreq,1), 1, 'last'));
   troughAfter = trLocs(find(trLocs > sortPeaksMat(idxFreq,1), 1, 'first'));
   fitRange = czt(troughBefore:troughAfter,:);

%    % optionally uncomment to manually set fitRange and comment out prev
%    % three lines
%    fitRange = czt(sortPeaksMat(idxFreq,1)-60:sortPeaksMat(idxFreq,1)+60,:);

   % See range highlight on graph
   figure(11); hold on;
   plot(fitRange(:,1),fitRange(:,2)/max(czt(:,2)),'+')
   hold off;

   % Fit to find central frequencies
   gaussian = fittype( @(A,f0,b,x) A*exp(-(x-f0).^2/b) );
   curvefit = fit(fitRange(:,1),fitRange(:,2)./max(fitRange(:,2)),...
       gaussian, 'StartPoint',[1,fGuess(idxFreq),1]);
   figure(12); hold on; title('Fit frequency peaks');
   plot(curvefit,fitRange(:,1),fitRange(:,2)./max(fitRange(:,2)));
   legend off;

   coeffvals = coeffvalues(curvefit);
   freqs(idxFreq) = coeffvals(2);

end % stepping through frequency peaks

hold off
```

```
end % of function fSAW

%=======================================
function transform = chirpZTrans(data,fMin,fMax)

% takes the chirp Z-transform of data - evenly spaced in the frequency
% range specified by fMin and fMax below
%
% Input: data = [time (in ps),signal], with t0 = 0 ps
%        fMin, fMax = min and max of frequency range to explore, in GHz
% Output: transform = [freq (in GHz), amplitude]
%
% Written by: Kathy Hoogeboom-Pot, 3/4/13
% ===============================================

time = data(:,1);
idx = find(time >= 0);
time = time(idx);
signal = data(idx(20:end),2);

dt = mean(diff(time)) * 1e-12; % signal time step

L = numel(signal); % length of signal (after t0)

maxFreq = 1/dt;
f1 = fMin*1e9; f2 = fMax*1e9; % frequency range of interest in Hz

m = 2^nextpow2(L);
w = exp(-1i*2*pi*(f2-f1)/(m*maxFreq));
a = exp(1i*2*pi*f1/maxFreq);

winSig = signal .* hamming(L); % Hamming Window

% Find transform and associated frequency scale in GHz
z = czt(winSig,m,w,a);
freqs = (((0:length(z)-1)'*(f2-f1) / length(z)) + f1) / 1e9;

transform = [freqs abs(z)];

% plot result
plot(freqs , abs(z)./max(abs(z)), 'lineWidth', 2); axis tight
set(gca,'yLim',[0,1.1]);
xlabel('Frequency (GHz)')
ylabel('Normalized CZT amplitude')

hold on

end % of chirpZTrans function
```

```
% ========================================
function Data = ft_pad(data, padMult)

% Takes Fourier transform with optional zero-padding
%
% Inputs: data = [time,signal], assumes t0 is at zero
%         padMult = integer giving how many times the length of the
%           original signal should be added in zero-pad; 0 means no padding
% Outputs: Data = [freq scale, FT amplitudes], only positive freqs, in GHz
%
% Written by: Kathy Hoogeboom-Pot, 3/1/2013
% ================================================

time = data(:,1);
sig = data(:,2);

N = numel(sig);
M = (padMult + 1) * N;

winSig = sig .* hamming(length(sig));

sigPad = padarray(winSig,[floor(M/2)-floor(N/2),0]);

SigPad = fftshift(fft(ifftshift(sigPad)));

dt = mean(diff(time));
wMax = 1/dt;
dw = wMax/M;
w = -wMax/2:dw:wMax/2-dw;
idx = find(w>0);

Data = [1000 * w(idx)' abs(SigPad(idx))];

end % of ft_Pad function
```

Appendix B

Mathematica code for the Matrix Pencil Method

This code uses the Matrix Pencil Method to extract the complex exponential components of any signal with evenly-spaced sampling. Specifically it can extract the decay times of both oscillating and pure exponentials, oscillation frequencies and starting phase for a specified number of signal components, ignoring the noise. It was used to extract the resonant LAW periods in the Ni/Ta bilayer studied in Chap. 6 of this thesis. For best results, irrelevant data components — especially any which are not described well by complex exponentials, like the transition from before to after time-zero — should be removed before applying this algorithm. This code comes with great thanks to Matthew Reynolds, who taught us this method and built the framework of this program.

B.1 Set up special functions and modules

```
(*
This function plots the locations of the exponentials;

inputs;
        z - list of exponentials;
    pr - range of the plot, such as {{-1,1},{-1,1}};
    co - color of the points;
outputs;
        A plot of the exponentials
*)

ArgandPlot[z_, pr_, co_] :=
 Show[Graphics[{PointSize[0.015], co,
    Point /@ Transpose[{Re[z], Im[z]}]}, Axes -> Automatic,
   AspectRatio -> 1, AxesLabel -> {"Re[z]", "Im[z]"}],
  PlotRange -> pr]
```

```
(*
This module takes an input sequence of length 2N+1, forms a
(N+1)×(N+1) Hankel matrix, and takes the SVD of that Hankel matrix;

inputs;
        input data - 2N+1 samples;
outputs;
        U,σ,V - SVD, where σ is a list of the singular values;
        H - Hankel matrix
*)

hanksvd[inputdata_] :=
 Module[{data = inputdata, num, U, σ, V, H, i, j,
   singularvalues},

  (*Form the Hankel Matrix*)
  num = (Length[data] - 1)/2;
  H = Table[data[[i + j + 1]], {i, 0, num}, {j, 0, num}];

  (*SVD*)
  {U, σ, V} = SingularValueDecomposition[H];
  singularvalues = Diagonal[σ];

  Return[{U, singularvalues, V, H}]
  ]

(*
This module implements the matrix pencil method. It modifies the
appropriate singular vectors, forms the matrix whose eigenvalues are
the exponentials you want, and finds those exponentials;

inputs;
        U0 - singular vectors;
        ind - index of the appropriate singular value;
outputs;
        zz1 - Output of matrix pencil method;
*)
(*Create a function to find nodes via the matrix pencil method*)
findnodesMPM[U0_, index_] :=
 Module[{Upp, Up1, Up2, vmatrix, zz1},

(*Construct the pencil matrix and find the eigenvalues*)
  (*modify the vector V from the SVD*)
  Upp = U0[[All, 1 ;; index]];
  Up1 = Upp[[;; -2]];
  Up2 = Upp[[2 ;;]];
  vmatrix = PseudoInverse[Up1].Up2;

  (*Find the eigenvalues*)
    zz1 = Eigenvalues[vmatrix];

  Return[zz1];
  ]
```

B.2 Import data and extract signal components

```
(*Import the data, etc*)
  data0 = Import[
        "FilePath\\FileName.extension"]; (* 2-column matrix, [time,signal] *)
  data = data0[[All, 2]]; (* We'll only use the signal column *)
(* The spacing of the time samples will be needed to convert
back to real time units *)
  dt = Mean[Differences[data0[[All,1]]]];
(* See what we have *)
  Show[ListPlot[data, Joined -> True],
    ListPlot[data, PlotStyle -> Hue[1]], PlotRange -> All]

(* Select the index of the starting point *)
(* Note that it is important have an odd number of samples to
correctly form the Hankel matrix!!! so Length[hankelData0] must be
odd *)
  startingPoint = <number after time-zero>; (* without the brackets *)
  hankelData0 = data[[startingPoint ;;]];
  Length[hankelData0]

(* Optionally fit and subtract out a 2nd-order polynomial -- as to
remove the slow rising background in LAW data *)
  trendFit[x_] = Fit[hankelData0, {1, x, x^2}, x];
  hankelData =
    Table[hankelData0[[j]] - trendFit[j], {j, 1, Length[hankelData0]}];
  Show[ListPlot[hankelData, Joined -> True],
    ListPlot[hankelData, PlotStyle -> Hue[1]], PlotRange -> All]
(* Use this line instead to skip background fitting *)
  (*hankelData = hankelData0;*)

(* Form the Hankel matrix H and take the SVD *)
  {U, σ, V, H} = hanksvd[hankelData];
(* Plot the singular values (normalized) and select the index
corresponding to the change in behavior. *)
  ListPlot[Log[10, σ/σ[[1]]], PlotRange -> All]

(* Enter that index and find the nodes using the rootfinding algorithm *)
(* Note that the pencil method outputs a number of exponentials = ind;
Expect 2*number of oscillating components + number of decaying components *)
  ind = <number of SVs corresponding to signal>;
  nodesIn = findnodesMPM[U, ind];

(* Create a vandermonde system to solve for the weights *)
(* Note that since the pencil method outputs the number of nodes equal
to the index, there is no need to solve the Vandermonde system twice *)
  vandermondeMatrix =
    Table[nodesIn[[j]]^i , {i, 1, Length[hankelData]}, {j, 1,
      Length[nodesIn]}];
  weights = LeastSquares[vandermondeMatrix, hankelData];
```

```
(* Plot the exponentials with respect to the unit circle *)
  cir = Graphics[Circle[]];
  Show[ArgandPlot[nodesIn, {{-1, 1}, {-1, 1}}, Black], cir]

(* Select the strictly decaying exponentials and corresponding weights *)
  indexRe0 = Table[i, {i, 1, Length[nodesIn]}];
  indexRe = Select[indexRe0, Abs[Im[nodesIn[[#]]]] < 10^-10 &];
  nodesRe = nodesIn[[indexRe]];
  weightsRe = weights[[indexRe]];

(* Select the oscillating exponentials and corresponding weights *)
  indexIm0 = Table[i, {i, 1, Length[nodesIn]}];
  indexIm = Select[indexIm0, Abs[Im[nodesIn[[#]]]] >= 10^-10 &];
  nodesIm = nodesIn[[indexIm]];
  weightsIm = weights[[indexIm]];

(* Check the results. Here I look at the decaying and oscillating parts
of the output approximation *)
  result = vandermondeMatrix.weights // Re;
  decayingResult =
    Table[Sum[
      weightsRe[[j]]*nodesRe[[j]]^i, {j, 1, Length[nodesRe]}], {i, 1,
      Length[hankelData]}];
  oscillatingResult =
    Table[Sum[
      weightsIm[[j]]*nodesIm[[j]]^i, {j, 1, Length[nodesIm]}], {i, 1,
      Length[hankelData]}];
  ListPlot[decayingResult, Joined -> True, PlotRange -> All]
  ListPlot[oscillatingResult, Joined -> True, PlotRange -> All]

(* Compare the output of the algorithm with the original data and
check remaining residual *)
  Show[ListPlot[result, Joined -> True],
    ListPlot[hankelData, PlotStyle -> Hue[1], Joined -> True],
    PlotRange -> All]
  ListPlot[hankelData - result, Joined -> True]

(* Convert back to time decay rates and periods *)
  aRe = Log[Abs[nodesRe]];
  bIm = Arg[nodesIm];
  aIm = Log[Abs[nodesIm]];
(* periods and decay times in whatever units the timesteps were recorded *)
  P = Table[2*Pi*dt/bIm[[i]], {i, 1, Length[bIm]}]
  oscDecay = Table[dt/aIm[[i]], {i, 1, Length[aIm]}]
  decay = Table[dt/aRe[[i]], {i, 1, Length[aRe]}]
```

Appendix C

MATLAB program for least-squares fitting with the acoustic transfer matrix

This program was used to find the best-fit velocities for Ni and Ta layers in an ultrathin bilayer from their resonant LAW oscillation periods in Chap. 6. It requires a range of velocities to test and the densities to assume (though only the ratio is actually used) for the two materials. Then it fits a polynomial to period vs. layer thickness data, and tests every pair of material velocities within the specified ranges to find the set of periods (calculated according to Eqn. 6.6) that have the smallest total squared difference to the polynomial fit representing the data. This procedure can optionally be executed in multiple sections, finding best-fit velocities for each subsection of the data.

```
function [vFitTop, vFitBottom] = transMatFit(data, props, vRangeTop,...
    vRangeBottom, res)

% transMatFit works to fit frequency vs. bilayer layer thickness (as for
% series of LAW samples) with optimal vLAW values for the two materials
% using the transfer matrix method of calculating resonant frequencies.
% Assumes one ('bottom') layer is of fixed thickness.
%
% Inputs: data = [top layer thickness in nm, LAW period in ps]
%         props = material properties, [densityTop, densityBottom,
%           vInitTop, vInitBottom, thicknessBottom]; densities must match
%           in units, v's expected in m/s, thickness in nm
%         vRangeTop,Bottom = fraction (0 to 1) by which to vary initial
%           velocities to seek fit
%         res = number of points to test across each vRange
% Outputs: vFitTop, vFitBottom = best-fit (in least squares sense) of two
%            material velocities from absolute minima in each section
%
% Written by: Kathy Hoogeboom-Pot, 9/18/13
```

```
% Modifications:
%     9/23/13, KHP, add second iteration of optimization for vTop
%       in separate sections of the polynomial fit
%     9/24/13, KHP, try 2D surface optimization in
%       sections rather than two iterations
%     11/1/13, KHP, add error bars to final plot and error plane to each 2D
%       surface
% ========================================================================

% Some setup
nm = 1e-9;
ps = 1e-12;
pTop = props(1);
pBottom = props(2);
viTop = props(3);
viBottom = props(4);
tBottom = props(5)*nm;
tTop = data(:,1)*nm;
wData = 2*pi./(data(:,2)*ps);
w = sym('w');

% Setup parameters you may wish to change:
order = 2; % order of polynomial to fit to data
numPts = 80; % number of points in fit
sections = 1; % number of separate sections over which to optimize vTop;
              % must divde into numPts without remainder
dataError = 1.1974e10; % sqrt(sum((errors on wData points).^2))
errorPoints = 9; % number of points included in the dataError calc.
errorCompare = dataError/errorPoints*numPts/sections; % scale the average
                                % data error to the number of points in
                                % each vTa section to allow comparison on
                                % plots of vTa residual curves

vTopTest = linspace(viTop-vRangeTop*viTop,viTop+vRangeTop*viTop,res);
vBottomTest = linspace(viBottom-vRangeBottom*viBottom,...
    viBottom+vRangeBottom*viBottom,res);

% Fit a low-order polynomial to data points to enable more points at which
% to test a fit plus smooth curve that leads to better result
tTopFit = linspace(min(tTop),max(tTop),numPts);
[p,S,mu] = polyfit(tTop,wData,order);

wFit = polyval(p,tTopFit,S,mu)';
figure; hold off;
plot(tTop,wData,'*',tTopFit,wFit,'-'); title('Poly fit to data');
xlabel('Top layer thickness (m)'); ylabel('Angular frequency');

%------------
% % Optionally uncomment to use this instead of previous polynomical fit to
% % fit to raw data
% tTopFit = tTop;
% wFit = wData;
%------------
```

```
% Break polynomial in sections (# specified at beginning)
tSection = reshape(tTopFit,length(tTopFit)/sections,sections);
wFitSection = reshape(wFit,length(tTopFit)/sections, sections);

%------------

% Solve for w (resonant frequency) for the sweeps through vTop and vBottom
% and calculate the sum of the squares of the differences between
% calculated w and wFit

variance = zeros(res,res,sections); % initialize output matrix
vFitTop = zeros(sections, 1); % initialize output v vectors
vFitBottom = zeros(sections,1);
vBottomBounds = zeros(sections, 2); %initialize output v error bar vectors
vTopBounds = zeros(sections,2);

tSectionLength = length(tSection(:,1));

for idx=1:sections % for each section of polyfit
    for ii=1:res % sweep vTop
        for jj=1:res % sweep vBottom
            wSimSection = zeros(tSectionLength,sections); % initialize the
                     % simulated vectors of w's which we'll compare to data

            for kk=1:tSectionLength % step through data point fit
                wSimSection(kk,idx) = ...
                    vpasolve(tan(w*tBottom/vBottomTest(jj))...
                    +pTop*vTopTest(ii)/(pBottom*vBottomTest(jj))...
                    *tan(w*tSection(kk,idx)/vTopTest(ii))==0,w,1e12);
            end % kk step through data points

            % Calculate the summed squared difference between sim and data
            variance(ii,jj,idx) = sqrt(sum((wSimSection(:,idx) - ...
                wFitSection(:,idx)).^2));

        end % jj sweep of vBottom

        ii % comment in/out to show/hide running counter
    end %ii sweep of vTop

    % Display resulting surface of variance
    figure; surf(vBottomTest,vTopTest,variance(:,:,idx));
    xlabel('vBottom'); ylabel('vTop'); zlabel('variance');
    title(strcat(['Section ' num2str(idx) ': tTop = ' ...
        num2str(tSection(1,idx)/nm) ',' num2str(tSection(end,idx)/nm)]));
    hold on

    % Find v's corresponding to minimum and plot the point
    mini = min(min(variance(:,:,idx)));
    [locTop, locBottom] = find(variance(:,:,idx) == mini);
    vFitTop(idx) = vTopTest(locTop);
    vFitBottom(idx) = vBottomTest(locBottom);
```

```
    plot3(vFitBottom(idx), vFitTop(idx), mini,'r*');

    % Add a plane representing the data error
    errorPlane = errorCompare * ones(length(vTopTest),length(vBottomTest));
    mesh(vBottomTest,vTopTest,errorPlane);

    % Find error bars on fit v's based on the variance surface's
    % intersection with error plane
    testVariance = variance(:,:,idx);
    testVariance(testVariance > errorCompare) = 0;

    if nnz(testVariance) > 0
        locLower1 = find(testVariance(locTop,:),1,'first');
        locUpper1 = find(testVariance(locTop,:),1,'last');
        vBottomBounds(idx,1) = abs(vFitBottom(idx)-vBottomTest(locLower1));
        vBottomBounds(idx,2) = abs(vFitBottom(idx)-vBottomTest(locUpper1));

        locLower2 = find(testVariance(:,locBottom),1,'first');
        locUpper2 = find(testVariance(:,locBottom),1,'last');
        vTopBounds(idx,1) = abs(vFitTop(idx)-vTopTest(locLower2));
        vTopBounds(idx,2) = abs(vFitTop(idx)-vTopTest(locUpper2));
    else
        vBottomBounds(idx,:) = [0,0];
        vTopBounds(idx,:) = [0,0];
    end

end % idx step through sections

% Plot fit velocities according to thickness of top layer at low end of
% section with the error bars found from plane intersections
figure;
errorbar(tSection(1,:)/nm,vFitTop,vTopBounds(:,1),vTopBounds(:,2),'o');
hold on;
errorbar(tSection(1,:)/nm,vFitBottom,vBottomBounds(:,1),...
    vBottomBounds(:,2),'ro');
xlabel('Top layer thickness starting each section (nm)');
ylabel('Fit velocities (m/s)');
title('What velocities appear optimum in each section?');
legend('Top layer','Bottom layer');

% Optionally display the resulting data fit when fitting in one section
% wFinal = zeros(length(tTop),1);
% w = sym('w');
% for kk=1:length(tTop) % step through data point fit
%    wFinal(kk) = vpasolve(tan(w*tBottom/vFitBottom)...
%       +pTop*vFitTop/(pBottom*vFitBottom)...
%       *tan(w*tTop(kk)/vFitTop)==0,w,1e12);
% end % kk step through data points
%
% figure (10); hold on;
% plot(tTop,wFinal,'o');
% legend('Data','PolyFit','OptFit');
```